Exploring Excitations and Vibrations in Semiconductor Nanocrystals through Fluorescence and Raman Spectroscopy

by

Anna Jolene Mork

B.A., Chemistry & Physics, Carleton College (2010)
S.M., Organic Chemistry, Massachusetts Institute of Technology (2012)

Submitted to the Department of Chemistry
in partial fulfillment of the requirements for the degree of

Doctor of Philosophy

at the

MASSACHUSETTS INSTITUTE OF TECHNOLOGY

June 2016

Author .....
Department of Chemistry
April 25, 2016

Certified by .....
William A. Tisdale
Assistant Professor
Thesis Supervisor

Accepted by .....
Robert W. Field
Chairman, Department Committee on Graduate Theses

Exploring Excitations and Vibrations in Semiconductor Nanocrystals through Fluorescence and Raman Spectroscopy

by

Anna Jolene Mork

Submitted to the Department of Chemistry
on April 25, 2016, in partial fulfillment of the
requirements for the degree of
Doctor of Philosophy

Abstract

Semiconductor nanocrystals, also known as quantum dots (QDs) have been used in solid state light emission applications ranging from fluorescent downconverters to LEDs and lasers, as well as energy generation devices such as solar photovoltaics and thermoelectrics. In order to realize these myriad applications, the fundamental physics of both electronic and vibrational energy transfer must be understood to engineer better device performance. This thesis begins with a general introduction to the physics and chemistry of QDs as well as an introduction to lattice vibrations, including a proposed model for understanding thermal conductivity in solid state QD-based devices. It continues with a discussion of the methods used to understand the photoluminescence and vibrational characteristics of QDs, including spectrally-resolved time-correlated single photon counting measurements to understand QD photoluminescence lifetime as a function of emission wavelength, and low-frequency Raman spectroscopy to measure acoustic phonons in nanocrystal solids. These two chapters serve as an introduction to the ideas and methods used throughout the thesis.

In Chapter 3, Förster theory is used in conduction with spectrally- and temporally-resolved photoluminescence spectroscopy to understand the rates of excitonic energy transfer in CdSe/CdZnS core/shell QDs through a calculation of the effective dipole-dipole coupling distance known as the Förster radius. This work demonstrated energy transfer rates between donor and acceptor QDs between 10-100 times faster than the predictions based on standard applications of Förster theory, corresponding to an effective Förster radius of 8-9 nm in close packed QD films. Several possible effects, including an enhanced absorption cross section, ordered dipole orientations, or dipole-multipole coupling, can explain the observed difference between our measurements and the Förster theory predictions, demonstrating that several standard assumptions commonly used for calculating QD resonant energy transfer rates must be carefully considered when the QDs are in a thin-film geometry.

Chapters 4-5 involve the use of low-frequency Raman spectroscopy to probe acoustic phonons in QDs. These low-frequency acoustic vibrations affect the

electronic, optical, and thermal properties of semiconductor nanocrystals, and the ability to rationally tune these modes would offer a powerful strategy for controlling phonon-assisted processes. Chapter 4 demonstrates that surface chemistry can be used to manipulate the low-frequency acoustic vibrations of CdSe QDs, and shows in particular that surface-bound ligands modify the resonant vibrational frequencies of the core. This effect is more pronounced for smaller nanocrystals, where the surface ligands constitute a larger fraction of the overall mass. A continuum mechanics model that explicitly includes the ligand shell quantitatively reproduces most of our experimental results. This model can be extended to understand the effect of inorganic shells as well, and we demonstrate that by growing a CdS epitaxial shell we can achieve reduction in acoustic phonon frequencies by more than 70% compared to the CdSe core alone. In Chapter 5, these low frequency phonons are further measured as a function of temperature. Low-temperature measurements allow the unambiguous assignment of overtone modes in large CdSe/CdS nanocrystals to a higher order ($n = 2$) vibrational mode rather than a multiphonon mode. Additionally, the acoustic phonon frequency is shown to vary with temperature though the linewidth remains constant for a variety of sizes of QDs. This variation of frequency without a corresponding broadening suggests that the pure volume contribution to the temperature-dependent phonon energies dominates over phonon-phonon interactions through anharmonic coupling.

Thesis Supervisor: William A. Tisdale
Title: Assistant Professor

Acknowledgments

The educational journey that has culminated in my doctoral thesis has been led and guided by many individuals along the way who I now have the honor and pleasure of thanking.

Before the personal acknowledgements, I have been variously funded during my time at MIT by the MIT Chapin Fellowship in the Department of Chemistry, the National Science Foundation Graduate Research Fellowship Program, and the Eni-MIT Solar Frontiers Research Center, and I gratefully acknowledge financial support from these sources.

First and foremost, I would like to thank my thesis advisor, Will, for his mentorship, support, and guidance throughout the course of my Ph.D. In particular, I have valued our discussions of science from first principles, without preconceived notions, in which learning felt like a collaborative process. I have always appreciated Will's unending enthusiasm for all aspects of science, which turns even failed experiments into opportunities after discussion, and I hope to retain some of this contagious excitement throughout my life. During my time in the Tisdale lab, I have learned a great deal through Will's leadership about how good science is done, and, equally importantly, how it is presented clearly and concisely. These are skills I will take forward with me, and represent an essential component of why I came to graduate school in the first place. Finally, I would like to thank Will for fostering a collaborative and inclusive group dynamic that promotes scientific growth without competition. I have enjoyed every single aspect of graduate school in the Tisdale lab, and cannot thank Will enough for the opportunity to join his group where I have learned and grown so much.

I came to MIT because I was fascinated by the concept that organic molecules could act as semiconductors, and I am grateful for the opportunity I had to explore this idea with Professor Tim Swager. My two years as a masters student were full of learning about new organic materials and new ways to view organic chemistry, inspired by Tim's always inventive ideas and dedicated group members. When I

rapidly came to the conclusion that I liked the idea of molecular semiconductors much more than their actual synthesis, Tim for supported me in my transition from organic to physical chemistry without judgement, for which I will always be grateful.

My work would not have been possible without help from many members of the Tisdale lab. Ferry Prins worked with me on developing the time- and spectrally-resolved photoluminescence measurements from Chapter 3, but more importantly spent a great deal of time teaching me how to think about experiments and how to use them to tell a story for publication. Without Ferry, it would have been much more difficult to get up to speed on physical chemistry and spectroscopy techniques—while Will was the general overseeing the lab from above, Ferry was on the ground with me every day fighting to make experiments work. Mark Weidman and Nabeel Dahod helped me substantially with nanoparticle characterization used throughout this thesis, and I very much appreciate their sometimes late nights (Nabeel) taking TEM images for me before meetings. Mark suggested the sizing curve in Appendix A used to standardize all TEM measurements, which turned out to be critical for turning confusing data into well defined results. Liza Lee developed the theoretical component of the QD acoustic phonon model presented here, always with penetrating insight and well informed discussions. Liza is the best collaborator I could have hoped for: timely, efficient, and extremely productive, and I thank her emphatically for her help getting the QD acoustic phonon work off the ground. Aaron Goodman, our group social chair, helped make all these results possible through planning group social activities that fostered good feeling between group members and provided an avenue to relax during the week. As my desk buddy for the past three years, Aaron has also helped me with learning keyboard shortcuts in Illustrator, answering random questions about Matlab, discussing and understanding seminar presentations, and being a sounding board for various ideas. I want to thank Aaron for making graduate school not just a learning experience, but actively fun. All of the members of the Tisdale group, both former and current, have been instrumental for not only my scientific learning but also for creating an enjoyable and happy workplace during graduate school.

I would like to also thank my parents, Loren and Laura Mork, for their dedication

to my learning and growth throughout my life. I perhaps would not be here if my parents had not taken me to science summer camps, and encouraged me to solve puzzles and do experiments starting as a child. In particular, I want to thank my father for taking me every week to do research projects at Amgen and the University of Washington during my final years of high school, which sparked my interest in research and inspired me to keep studying science. I also want to thank my mother for being a constant and quiet support through difficult times, and for always listening, offering advice or consolation, and helping me keep a sense of perspective. My brother, Frazier, is always a source of interesting facts and cooing noises, and I could not imagine a better sibling. A loving and supportive family makes even the most challenging circumstances manageable, and makes the effort all the more worthwhile at the end.

Finally, I would like to thank my best friend and fiancé, José Cordero, for being by my side through late nights in lab and experiments that fail, for believing that I am better than I think I am, for pushing me to try harder and think more deeply, and for always making my smile.

This doctoral thesis has been examined by a Committee of the Department of Chemistry as follows:

Professor Moungi G. Bawendi.....
Chairman, Thesis Committee
Lester Wolfe Professor of Chemistry

Professor William A. Tisdale.....
Thesis Supervisor
Charles & Hilda Roddey Career Development Assistant Professor of Chemical Engineering

Professor Timothy M. Swager.....
Member, Thesis Committee
John D. Arthur Professor of Chemistry

Contents

Chapter 1

Introduction

Measuring only a minuscule few nanometers in diameter, semiconductor nanocrystals represent an enormous promise for a brighter future, a future in which low-cost solution processed materials may replace expensive single-crystal solar cells, a future that allows energy efficient LEDs to supplant other lighting technologies while improving color quality, a future in which waste heat from engines and power plants is captured and recycled to improve the overall productivity of energy generators at all scales. In order to actualize these dreams, scientists have spent more than 30 years understanding the fundamental physical and chemical properties of these materials, while engineers have optimized their implementation in myriad device architectures [1]. Several companies have successfully commercialized nanocrystal-based technologies for fluorescence downconversion in order to create beautiful, high color-purity liquid crystal display (LCD) screens, and continue to perfect other technologies, such as light emitting diodes (LEDs) (Figure 1-1). In order to improve performance in these and other devices, scientists must understand the interactions between inorganic nanocrystals and their ligands, their neighbors, and their environment.

While many engineering hurdles remain before large-scale deployment of nanocrystal technologies, the energy transfer characteristics of nanocrystal-based devices dictate much of their efficiency. Additionally, different types of devices may require very different energy transfer properties from their QD active material, highlighting

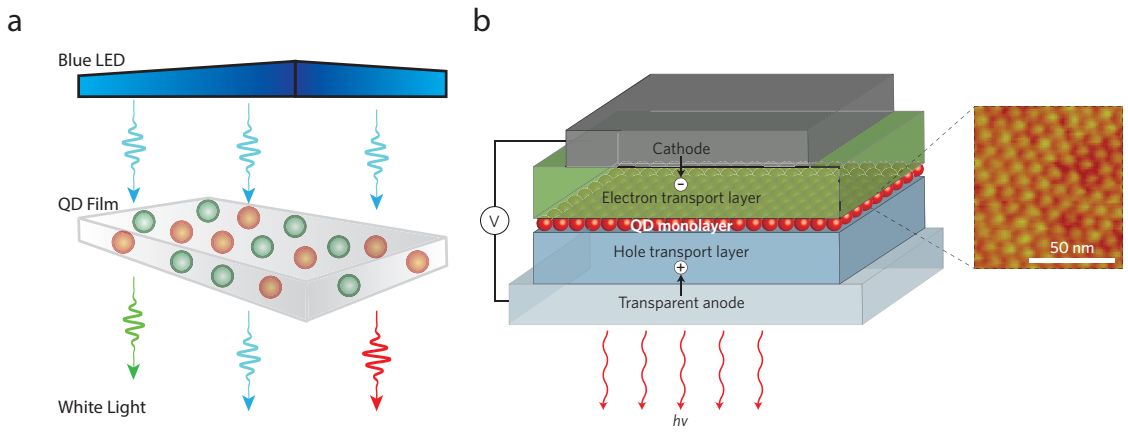

Figure 1-1: Examples of devices employing excellent fluorescence properties of semiconductor nanocrystals. a) Generalized structure for fluorescent downconverter, including a high efficiency blue LED and a film of nanocrystals embedded in a matrix to partially convert the blue light to red and green colors in order to achieve white light emission. b) Generalized structure of a nanocrystal LED in which the nanocrystals form the active layer. (Panel b reprinted with permission from Macmillan Publishers Ltd, reference [2], ©2012)

the importance of tunability in the synthesis and processing of QDs. For example, non-radiative energy transport can detrimentally affect the spectral properties of nanocrystal LEDs [3], but plays an essential role in the phenomenon of 'quantum funneling' where electronic energy is transported down a potential gradient [4]. Similarly, thermal conductivity (i.e. vibrational energy transfer) can impact device efficiency, as high thermal conductivity is essential for functioning nanocrystal-based lasers [5], while low thermal conductivity results in improved nanocrystal thermoelectric devices [6]. Engineering the most efficient devices therefore necessitates an understanding of both electronic and vibrational energy transfer characteristics in order to properly tailor them for a specific application.

1.1 What is a Quantum Dot?

The deliberately vague term 'semiconductor nanocrystals' refers to a material composed of a crystalline inorganic semiconductor confined in size to the nanometer regime. Researchers have succeeded in synthesizing many types of nanocrystals with

different aspect ratios and geometries, but the canonical nanocrystal for the purposes of this thesis will be the 'zero dimensional' quantum dot, or QD. In particular, this thesis will focus on a family of QD materials based around the II-VI semiconductor CdSe, though QDs can be made of a variety of other II-VI, III-V, and even group IV semiconductors. These QDs are colloidally synthesized (See Appendix A for further information), roughly spherical, and typically contain hundreds to thousands of atoms of semiconductor material surrounded by organic ligands that passivate the dangling bonds and confer solubility, with an optional epitaxial inorganic shell between the core and the ligands that also helps to passivate the core surface (Figure 1-2).

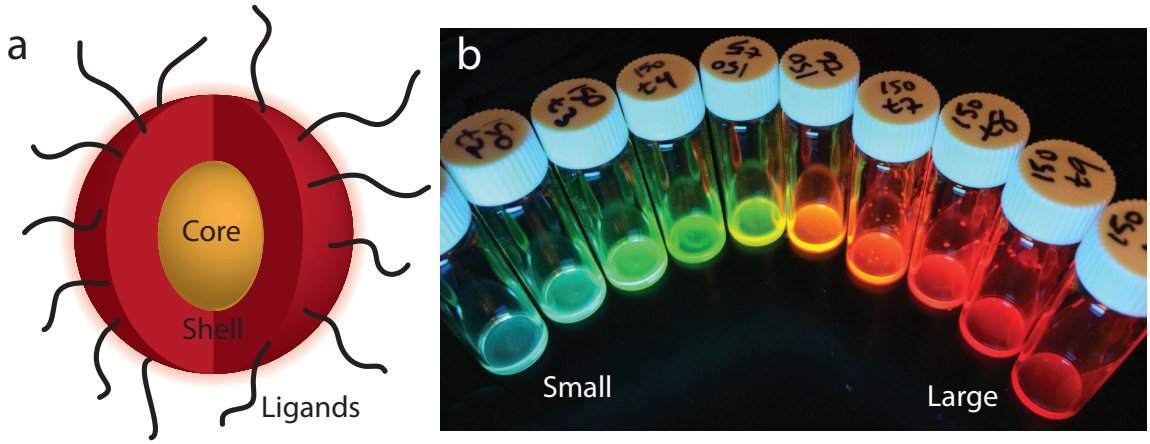

Figure 1-2: a) Schematic of a QD, including inorganic semiconductor core, optional semiconductor shell, and organic ligands bound to the surface. b) Image of core-only CdSe QDs synthesized by the author, arranged in size from smallest (left) to largest (right).

The inorganic semiconductor and organic ligand shells that surround the QD core are highly tunable and application-specific. The native ligands added during synthesis are typically long, aliphatic hydrocarbons bound to the QD through a phosphonic or carboxylic acid, but may be exchanged post-synthesis for a number of different molecules depending on the desired application. For example, these ligands may be exchanged for hydrophilic polymers to enable QDs as fluorescent probes for biological imaging [7], or very short molecules or ions that enable tightly packed films for solar photovoltaic applications [8,9]. The inorganic shell typically is made of a higher band

gap semiconductor than the core to help confine excitons (CdS or ZnS are commonly paired with CdSe cores) [10, 11], though lower band gap shells (e.g. ZnTe) can be used to create more exotic type-II core-shell heterojunctions if desired [12].

The size of the QD core, the nature of any inorganic shell material surrounding the core, and the identity of the passivating organic ligands all affect the electronic, optical, and vibrational properties of the material, yielding a system that is highly tunable and complex.

1.2 Electronic Properties of QDs

Much of the utility of QD materials derives from the quantum confinement effects that alter the energy levels of the parent bulk semiconductor. The characteristic length scale that determines 'confinement' is the Bohr radius, a_B, defined as

$$a_B = \epsilon \frac{m}{m^*} a_0. \tag{1.1}$$

Here, a_0 is the Bohr radius of the hydrogen atom, ϵ is the dielectric constant of the material, m is the rest mass of the particle (electron, hole, or exciton) of interest, and m^* is the effective mass of the particle in the material. It is thus possible to calculate Bohr radii for the elementary particles (including both electrons and holes, the latter referring to the valence band quasiparticle resulting from the absence of an electron) as well as excitons, the Coulombically bound electron-hole pairs. For CdSe, the Bohr radius for the exciton is $\sim$ 6 nm [13]. Nanoparticles smaller than the Bohr radius demonstrate confinement effects, which means that the edges of the nanostructure affect electronic energy levels within the material.

The simplest way to conceptualize the size effects associated with the confinement of an exciton (or electron, or hole) to a small space is through the well-known quantum mechanical problem of the particle in a box. In the 1D problem, a particle of mass m moves inside a potential well of length L where the potential energy is zero within the well and non-zero outside. The stationary state wavefunction of the particle, $\psi(x)$, which describes properties such as its energy, can be calculated by solving the

time-independent Schrödinger equation given by

$$-\frac{\hbar^2}{2m}\frac{d^2\psi}{dx^2} + V(x)\psi(x) = E\psi(x), \tag{1.2}$$

where $\hbar$ is Planck's constant, m is the particle mass, $V(x)$ is the potential energy function, and E is the energy of the particle. In the case of a particle in a square well with infinite energy barriers ($V(x) = \infty$ outside the well), the solutions to Equation 1.2 are a series of sine waves, and the energy of the n^{th} energy level is given by

$$E_n = \frac{\hbar^2\pi^2 n^2}{2mL^2}. \tag{1.3}$$

This simple problem yields several key insights, the most important of which for the purposes of this thesis are that the energies of the particle vary *inversely* with the length L of the box (Figure 1-3a). The particle-in-a-box problem can be readily extended to three dimensions, and can be solved in spherical coordinates. In this case, the wavefunctions resemble atomic orbitals, and can be similarly described by the quantum numbers n, ℓ, and m. Again, the quantized energies of the particle in a sphere are inversely proportional to its size; in this case, $E \propto 1/r^2$ [13]. Translating the results of the particle-in-a-sphere problem, which describes a particle trapped in a finite volume of empty space, to describe the physics of an electron or exciton in a semiconductor nanocrystal requires a series of approximations and assumes that the nanocrystal size is much larger than the lattice constant of the material, but the end result is that the electrons and holes within QDs can be described by atomic-like orbitals confined within the nanocrystal and typically denoted with capital letters, $1S$, $2P$, etc. [13]. The quantized energy levels of the electrons and holes near the semiconductor band edge result in a size-dependent band gap for QDs (Figure 1-3b), where the band gap increases for smaller nanoparticles just as the energies increase for smaller confinement regions in Equation 1.3.

Many spectroscopy experiments have sought to understand in detail the relationships between different electronic energy levels within the manifold of states suggested by Figure 1-3b, and a rich literature exists surrounding both inter-band

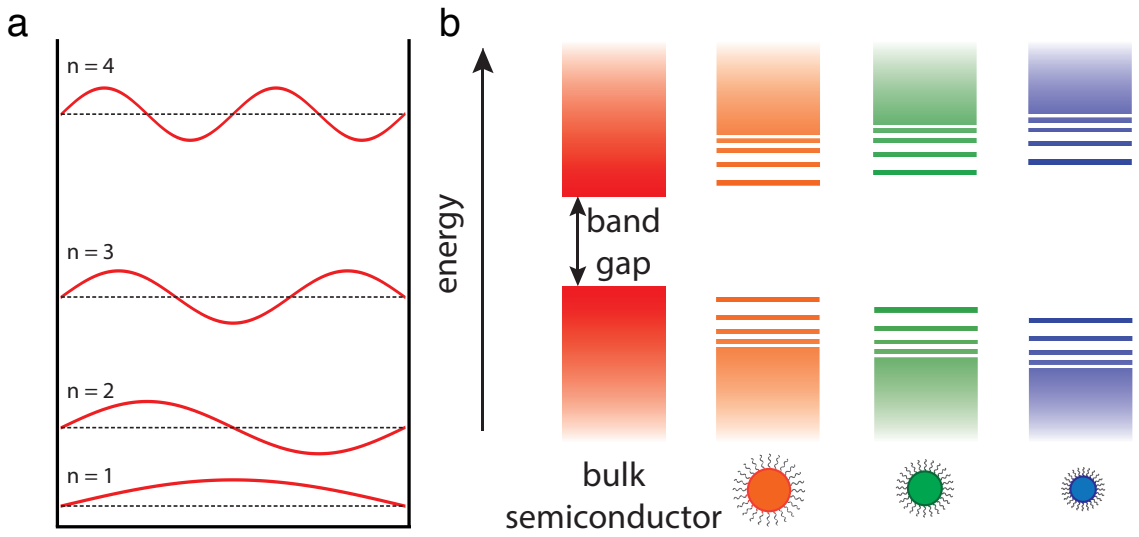

Figure 1-3: a) Wavenunction $\psi(x)$ solutions to the 1D particle-in-a-box problem. b) Schematic of quantization of energy levels in semiconductor nanocrystals, with increasing band gap for smaller nanoparticles.

and intra-band transitions in QD materials at both the ensemble and single-particle levels [14–17]. In bulk semiconductors, the band gap of the solid is manifest in the absorption onset, and for energies higher than this onset the absorption spectrum is continuous and nearly featureless (Figure 1-4). In QDs, however, all of the oscillator strength of the bulk material is concentrated into discrete transitions due to the small size of the nanocrystal, which yields an absorption spectrum characterized by strong absorption features with energies corresponding to the energies of these transitions (Figure 1-4).

The concentration of oscillator strength into certain discrete transitions in nanocrystals can be understood in terms of the parabolic band structure shown in Figure 1-5. In a bulk semiconductor material of 'infinite' size, the energy (E) and crystal momentum (k) for an electron can be precisely defined, though the position of the electron cannot. Near the band edge, the relationship between E and k is roughly parabolic (a result arrived at through the application of perturbation theory to solutions to the Schödinger equation for a periodic lattice of atomic potential wells [19]), with a width proportional to the effective mass (m^*, Equation 1.1) of the

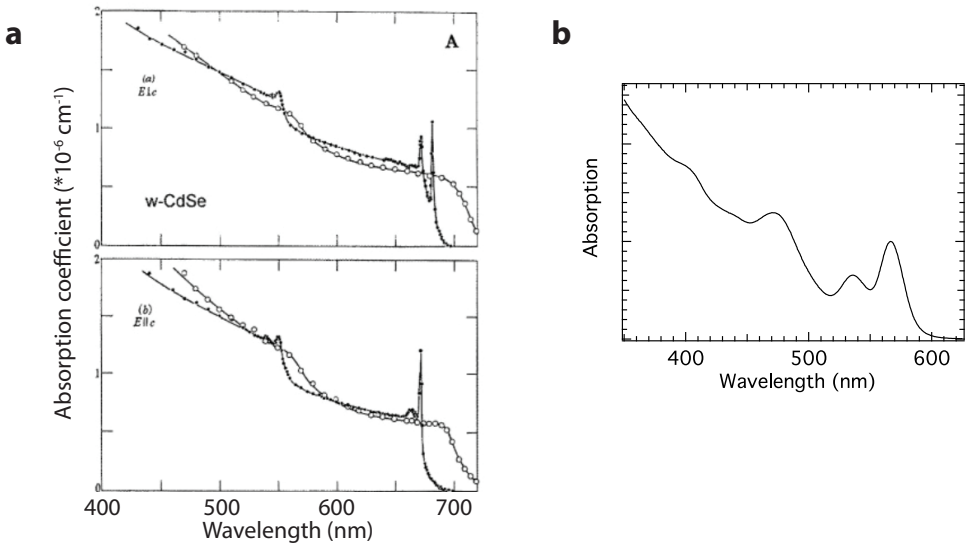

Figure 1-4: a) Absorption spectra for bulk wurtzite CdSe, with excitation either parallel (top) or orthogonal (bottom) to the c-axis. Data collected at 4K and at room temperature, revealing low-temperature exciton peak. Reproduced from reference [18] b) Absorption spectrum of CdSe nanoparticle, with several absorption features visible (at room temperature).

electrons (conduction band) or holes (valence band) of the material. An electron with any k in the valence band can absorb a photon of the correct energy and be promoted to the conduction band, yielding a continuous absorption spectrum for photon energies larger than the band gap. However, in a nanocrystal the greater certainty in electron position results in greater uncertainty in its momentum. This ultimately results in transitions that would be close but different in energy in the bulk solid to collapse into a few strong transitions in the nanocrystal because a bandwidth of momentum states from an infinite crystal maps to the same energy (Figure 1-5b) [20]. In the nanocrystal absorption spectrum shown in Figure 1-4b, the lowest energy (longest wavelength) peak corresponds to the band gap of the nanocrystal ensemble, or the $1S^h_{3/2}1S_e$ transition (for assignment of other transitions, see [13]).

The width of the transitions in QD absorption and emission spectra are affected by both homogeneous and inhomogeneous components. The homogeneous linewidth depends on factors such as spectral diffusion, coupling to phonons, and the exciton fine structure, while the inhomogeneous linewidth is dominated by sample polydispersity

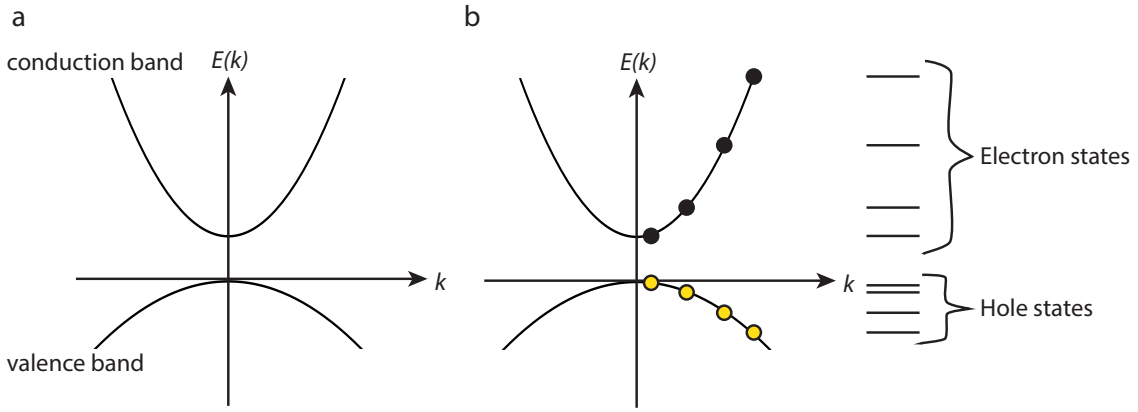

Figure 1-5: a) Valence and conduction bands near the band gap minimum for a bulk semiconductor, where the E vs. k relationship is nearly parabolic. Promotion of an electron from the valence band to the conduction band can occur for any k, yielding a continuous set of available transition energies. In this diagram, as for CdSe, the effective mass m_{eff} of the hole is larger than the electron. b) For quantum confined systems, transitions can occur only for certain k (represented by circles) yielding a discretized energy spectrum (right) similar to that drawn schematically in Figure 1-3.

[21, 22]. Due to the strong dependence of the band gap on particle size ($1/r^2$, as described above), even a small degree polydispersity in QD size within a sample can result in significant broadening of the absorption and emission spectra. The effect of this polydispersity on excitonic energy transfer within a homogeneous film will be discussed in more detail in Chapter 3.

1.3 Phonons in Crystals

The electronic/excitonic properties of QD nanocrystals have received extensive attention, while their vibrational properties have been comparatively neglected. The collective excitation of atoms within a crystal is called a *phonon*, a boson quasiparticle that plays a significant role in both the thermal and electrical conductivity of materials. This section will discuss the classical mechanics approach to defining the vibrational modes of a lattice of atoms, and will define the difference between optical and acoustic phonons in bulk solids [19]. The specific case of vibrations within QDs will be discussed in detail in Chapter 4.

1.3.1 Normal modes of a harmonic crystal

The most basic picture of a crystal is a set of atoms connected by springs, as in Figure 1-6 (top). In this model, the atoms all have mass M, and are uniformly spaced with equilibrium distance a and all springs are characterized by the same spring constant K. Assuming that $u(na)$ is the displacement along the 1D line from the equilibrium position of the n^{th} atom (see Figure 1-6 bottom), the harmonic potential energy U is of the form

$$U^{harmonic} = \frac{1}{2}K\sum_{n}[u(na) - u((n+1)a)]^2 \tag{1.4}$$

in analogy to the classical harmonic oscillator, where the potential energy is proportional to the spring constant K times the square of the displacement from equilibrium. Plugging this potential energy function into Newton's third law yields the equation of motion

$$M\ddot{u}(na) = -\frac{\partial U^{harmonic}}{\partial u(na)} = -K[2u(na) - u((n-1)a) - u((n+1)a)] \tag{1.5}$$

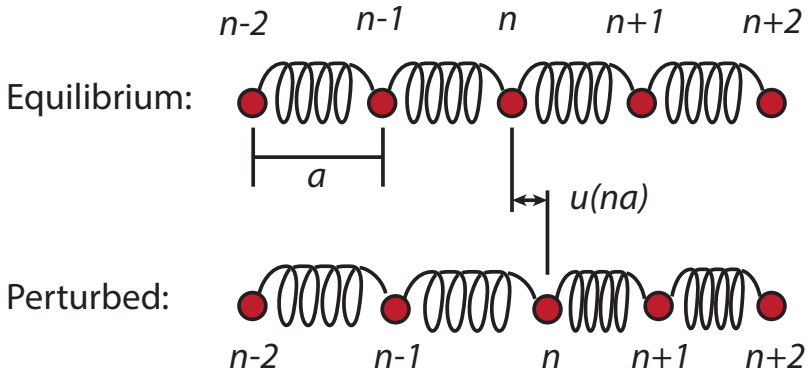

Figure 1-6: Schematic of harmonic crystal lattice depicting atoms (red circles) connected by springs. Top: all atoms are in their equilibrium position, with distance a separation. Bottom: atoms disturbed from equilibrium with some springs compressed and others expanded. The displacement distance from equilibrium for the n^{th} atom is $u(na)$.

Using a periodic boundary condition for N atoms implies that $u((N+1)a) = u(a)$ and $u(0) = u(Na)$. The solutions to the equation should be of the form

$$u(na, t) \propto e^{i(kna-\omega t)} \tag{1.6}$$

for wavevector k and frequency ω. The periodic boundary condition implies that k is given by

$$k = \frac{2\pi}{a}\frac{n}{N} \tag{1.7}$$

for integer n. Therefore, there are only N values of k that yield unique solutions, and these are typically taken to lie between $k = -\pi/a$ and $k = \pi/a$. Substituting Equation 1.6 into Equation 1.5 yields

$$-M\omega^2 e^{i(kna-\omega t)} = -2K(1 - \cos(ka))\, e^{i(kna-\omega t)} \tag{1.8}$$

with a solution for the frequency ω as a function of k given by

$$\omega(k) = 2\sqrt{\frac{K}{M}}|\sin(\frac{1}{2}ka)|. \tag{1.9}$$

The solutions of the actual displacements of the atoms are sine and cosine functions with argument $(kna-\omega t)$. The displacement wave travels with phase velocity $c = \omega/k$ and group velocity $v = \partial\omega/\partial k$. The relationship between ω and k is known as the dispersion relation. The dispersion relation for a 1D monatomic chain is plotted in Figure 1-7. This dispersion relation is valid for a one dimensional lattice consisting only of a single atom, as might be the case for a single-element material.

Many materials are composed of more than one distinct atom, so this simple model must be expanded to understand phonons in compound materials. For a two-atom basis (e.g. CdSe), the equations of motion must be calculated for the individual atoms, which leads to a set of coupled differential equations. The general picture used to determine the set of differential equations is shown in Figure 1-8, which includes two types of atoms and two types of springs with spring constants K_1 and K_2.

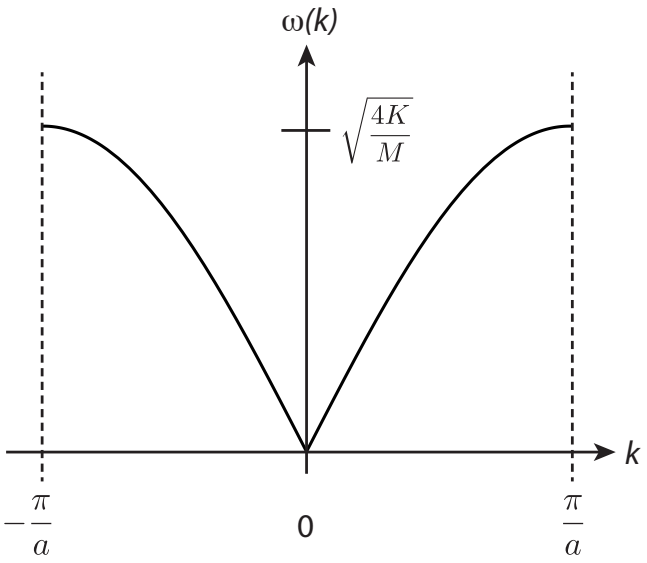

Figure 1-7: Dispersion relation plotted for k ranging from $-\pi/a$ to π/a (the first Brillouin zone) for a 1D monatomic linear chain.

To simplify the problem of solving the equations of motion for this 1D chain with 2-atom basis, both atoms have mass M. The harmonic potential energy then has the form

$$U^{harmonic} = \frac{K_1}{2}\sum_n [u_1(na) - u_2(na)]^2 + \frac{K_2}{2}\sum_n [u_2(na) - u_1((n+1)a)]^2, \quad (1.10)$$

with individual displacements from equilibrium u_1 and u_2 for the two atoms in the basis. Assuming again solutions of a form similar to Equation 1.6, the relationship between ω and k is given by

$$\omega^2 = \frac{K_1 + K_2}{M} \pm \frac{1}{M}\sqrt{K_1^2 + K_2^2 + 2K_1K_2\cos(ka)}. \quad (1.11)$$

The two solutions for ω given by Equation 1.11 indicate that there are $2N$ normal modes for a chain with N primitive cells of two atoms, and these two solutions for ω form two 'branches' of the dispersion relation between ω and k (Figure 1-9). The upper branch forms the 'optical' modes, while the lower branch forms the 'acoustic'

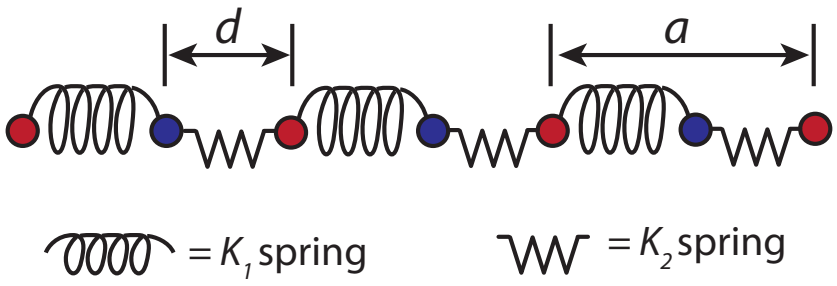

Figure 1-8: Schematic depicting 1D chain with 2-atom unit cell and different springs.

modes in the material. As shown schematically in Figure 1-9, acoustic phonons are those in which the ions in a particular primitive unit cell move in-phase with one another and dynamics are dominated by inter-cell interactions, while optical phonons are those in which the atoms within a single unit cell move in opposite directions (similar to a molecular vibration). The slope of the linear part of the acoustic mode dispersion relation near $k = 0$ is the speed of sound in the material, and the speed of sound is a function of the two spring constants and the two masses of the atoms in the lattice.

The extension of this model to 3D complicates the problem because the atoms are no longer contained to vibrate in 1D, which means there are two orthogonal transverse motions of the atoms along with the compressional (longitudinal) motion previously considered. The two transverse waves and the longitudinal wave are independent from each other, and can split both the optical and acoustic branches into three 'sub-branches'. Calculations of the energies of these different sub-branches requires some knowledge of the symmetry of the crystal under study; in some crystal directions, for instance, the two transverse phonons be degenerate (see acoustic branch in Figure 1-10 for $\Gamma \rightarrow$L) while they separate in energy for other crystallographic directions (Figure 1-10 $\Gamma \rightarrow$K). In general, the transverse phonons are lower energy (smaller ω for a given k) than the longitudinal.

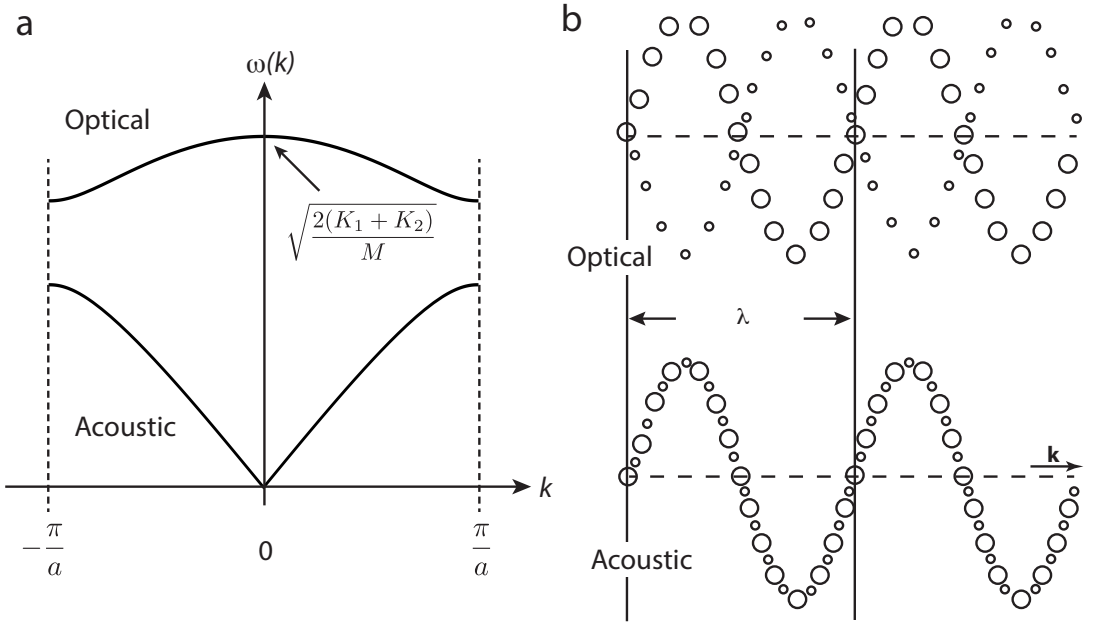

Figure 1-9: a) dispersion relation for 1D chain with 2-atom basis, with lower frequency acoustic modes and higher frequency optical modes labeled. b) schematic depiction of transverse optical (top) and transverse acoustic (bottom) modes for a 2-atom basis. The wavelength (λ) and the direction of propagation are indicated.

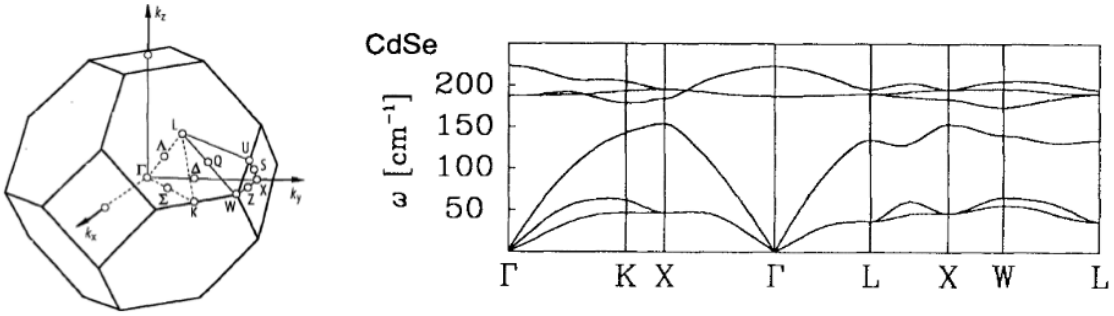

Figure 1-10: Left: First Brillouin zone for a zincblende crystal, with symmetry points labeled. Right: Calculated phonon dispersion curve for zincblende CdSe, showing both optical and acoustic phonons, as well as splitting between transverse and longitudinal phonons. The two transverse phonons are degenerate along some crystallographic directions but not others. Dispersion curve reproduced with permission from [23], ©1993 American Physical Society.

1.3.2 Thermal Conductivity

The thermal conductivity, κ, of a classical (bulk) material relates the heat flux, $\vec{q}$, to the temperature gradient, ∇T, in Fourier's law of heat conduction

$$\vec{q} = -\kappa \nabla T. \tag{1.12}$$

Both electrons and phonons can contribute to thermal conductivity in metals, but for semiconductors and insulators thermal conductivity is dominated by the contribution from phonons, κ_{ph}. It is worth noting that for perfectly harmonic crystals, lattice vibrations are stationary states, and therefore their distribution remains unaltered in time. In this case, the thermal conductivity for a material would be infinite. The phenomenon of thermal conductivity results from the anharmonicity of the interatomic potentials that bind atoms. Bond anharmonicity will be discussed in greater detail in Chapter 5.

From the kinetic theory of gases, the formula for thermal conductivity is

$$\kappa = \frac{1}{3} n c_v v_\lambda \tag{1.13}$$

for n particles each with heat capacity c_v and v average velocity for mean free path length λ. This theory for gases can be extended to solids where the individual phonons act as gas particles, each with energy $\hbar\omega(k)$ and momentum $\hbar k$. The lattice thermal conductivity of a material, κ_{ph} is the thermal energy carried by these phonons, and can be written as

$$\kappa_{\text{ph}} = \frac{1}{3V} \sum_k c_v(k) v_g(k) \lambda(k), \tag{1.14}$$

where the average velocity has been changed to the phonon group velocity v_g [24]. In this formulation, the lattice thermal conductivity is determined by the velocity and mean free path of the phonons that are occupied at the temperature of interest. In order to examine how specific phonons contribute to the lattice thermal conductivity, Equation 1.14 can be converted to a thermal conductivity 'accumulation function',

where $\kappa_{\text{accum}}(\lambda^*)$ is the thermal conductivity of the lattice due to phonons having mean free path (MFP) shorter than λ^*:

$$\kappa_{\text{accum}}(\lambda^*) = \sum_{\text{polarization}} \int_0^{\lambda^*} \frac{1}{3} c_v(\lambda)\, v(\lambda)\, \lambda d\lambda. \tag{1.15}$$

Measuring thermal conductivity as a function of mean free path provides an avenue to study the types of phonons that contribute most significantly to thermal conductivity. This experiment has demonstrated that, for crystalline silicon, about 40% of the material thermal conductivity comes from phonons with $\lambda > 1\mu m$, while for amorphous silicon $\sim 30\%$ of the thermal conductivity results from phonons with $\lambda >$ 100 nm [25]. These data demonstrate that long-wavelength, low frequency phonons contribute significantly to thermal conductivity in both crystalline in amorphous materials, though their vibrational density of states is relatively low.

In the case of QDs, the picture becomes substantially more complicated. For bulk solids, thermal conductivity is limited by phonon-phonon scattering and scattering off defects in the crystal lattice, but for QDs the multitude of interfaces results in significant interface scattering (Figure 1-11). The macroscopic theory of heat transfer described by Fourier's law (Equation 1.12) assumes purely diffusive heat transport, which occurs when the mean free path of the phonons carrying heat energy is much smaller than the length scale over which the heat is transferred. If, on the other hand, the phonon mean free path is similar to the length scale of interest, thermal transport is 'ballistic' and the heat diffusion equation cannot always be applied.

The phenomenon of thermal boundary resistance, which may play a role at the QD-ligand interface, was first discovered in 1936 in studies of the interface between liquid helium and solids, but was neglected for 15 years until the first mathematical model to understand thermal interface resistance (also called the Kapitza resistance) appeared in 1952 [26]. There are two main models to describe heat flow across an interface: the acoustic mismatch model and the diffuse mismatch model. The acoustic mismatch model assumes there is no scattering of phonons at the interface, and the phonon transmission probability from material A to material B depends only on the

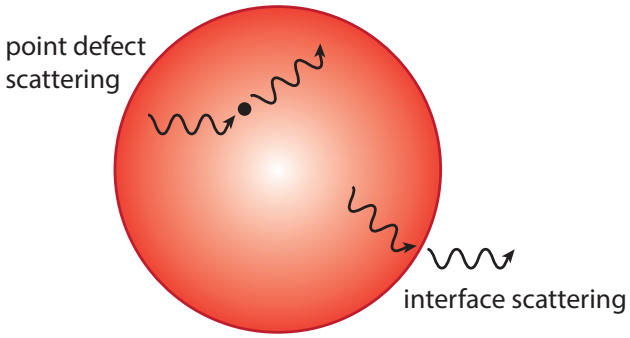

Figure 1-11: Phonons in QDs and other nanostructures not only scatter off of crystal defects, but also the nanocrystal surface.

acoustic impedances, Z, of the materials, where $Z = \rho c$ for density ρ and material-specific sound velocity c. Alternatively, the diffuse mismatch model assumes perfect scattering of phonons at the interface, and the transmission probability depends on the phonon density of states on each side. For both models, the thermal conductance G of an interface is related to the transmission coefficient t_{AB} across it by

$$G(T) = \int C(\omega, T)\langle v(\omega)\rangle \, \langle t_{AB}(\omega)\rangle d\omega, \tag{1.16}$$

where $C(\omega, T)$ is the specific heat, $\langle v(\omega)\rangle$ is the averaged component of the phase velocity orthogonal to the interface, and $\langle t_{AB}\rangle$ is the transmission coefficient averaged over all phonon bands and wavevectors [27]. The best model to choose for a particular materials system depends heavily on the interface structure and the wavelengths of phonons incident upon it, and structuring interfaces at different length scales can selectively change the scattering of specific phonons. Structuring materials at the nanoscale is a known method to change $G(T)$ and therefore the thermal conductivity, which can be seen, for example, in Figure 1-12, which plots the calculated thermal conductivity of a SiGe sample with different fractions of silicon in a germanium host. In this case, the bulk alloy is compared to structures with different diameter Si wires, and the results demonstrate that greater nanostructuring (more, smaller inclusions

of Si in Ge host) resulted in lower thermal conductivities [28].

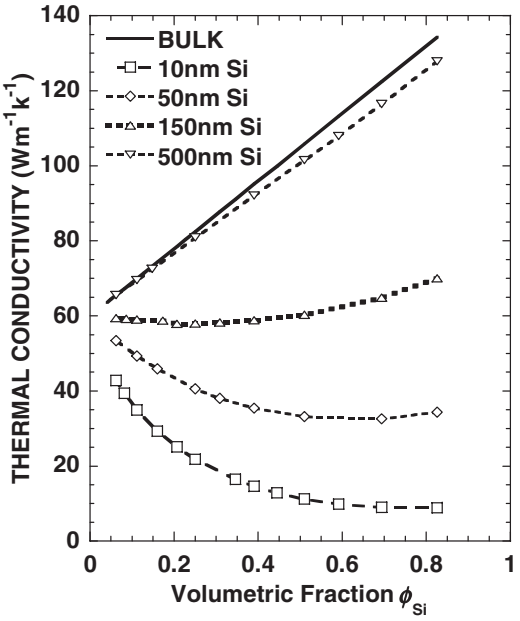

Figure 1-12: Calculated thermal conductivity as a function of silicon content in a germanium host matrix, with varying diameters of silicon nanowires compared to experimental results for the bulk SiGe alloy. Image reproduced from [28].

Contrary to typical nanostructured SiGe and other all-inorganic materials, a QD film is composed of a set of inorganic cores surrounded by organic ligands, yielding a system with very different vibrational properties between its two phases. A comprehensive study of nanocrystal thermal conductivity revealed several key findings: (1) the measured thermal conductivity was independent of sample thickness across a large temperature range, suggesting that thermal transport is dominated by relatively short mean free path phonons traveling diffusively through the material, (2) accurate modeling of the thermal conductivity in these materials required the addition of a thermal boundary resistance between the nanocrystal core and the surrounding ligands, and (3) the temperature dependence of the measured thermal conductivity suggests that overlap of ligand and core vibrational states plays a key role in controlling the thermal conductivity of a material [29].

In a follow-up to this work, the same authors showed theoretically that the ligand

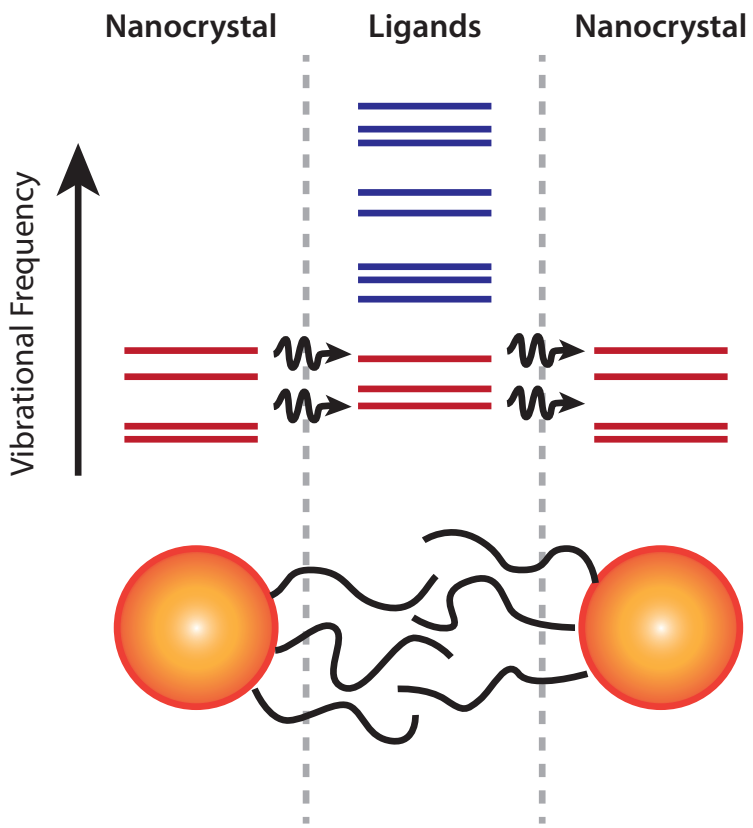

Figure 1-13: Thermal conductivity in QD-based materials may be limited by vibrational density of states overlap between nanocrystals, which typically have only relatively low energy vibrations, and their ligands which have many higher energy vibrational modes.

grafting density and the vibrational density of states spectrum of the core and ligand materials are key factors determining the thermal conductivity of QD solids [30]. These studies combined suggest that ligands play an important role in determining the thermal properties of QD-based materials, and, in particular, the vibrational density of states overlap between ligands and nanocrystals holds the key to engineering thermal properties. Figure 1-13 schematically illustrates the current proposal for heat transfer in nanocrystals: the QDs have very low energy vibrational states, which may overlap to some degree with ligand vibrations, but ligands (center) also have

many higher-lying vibrational levels [31]. At higher temperatures, the ligand-specific vibrational modes can be active, but their is no density-of-states overlap with QDs for these higher energies, and they cannot usefully contribute to thermal conductivity in the material. Based on this model, tuning the vibrational energy states of the QD core may allow better overlap with the ligand density of states and contribute to improved thermal conductivity.

1.4 Thesis Overview

Enabling this understanding of energy transport in nanomaterials requires the development of corresponding tools capable of probing energy levels and dynamics. Optical spectroscopy techniques, in which light is used to interrogate materials, have served to elucidate much of the fundamental physics of nanomaterials, and serve as the basis for the experiments presented in this thesis. In particular, time-resolved fluorescence spectroscopy and low-frequency Raman spectroscopy have served as the basis for many of the experiments presented in this thesis. Chapter 2 describes in more detail these spectroscopic techniques, including theoretical background as well as the specifics of the instrumentation used. Chapter 3 describes results related to excitionic energy transfer in thin films of colloidal QDs, and the calculation of the Förster radius, an important parameter used for determining energy transfer efficiencies. Chapter 4 describes the use of low-frequency Raman spectroscopy to understand how the acoustic phonon energies in QDs can be tuned using surface chemistry and nanocrystal composition. Finally, in Chapter 5, the low-frequency Raman technique is extended to low temperatures to learn more about the identity of previously unresolved overtone modes, as well as understand temperature-dependent shifts in the acoustic phonon spectrum.

Chapter 2

Experimental Techniques

Many spectroscopic techniques exist to probe the fate of excitons, electrons, and holes in QDs and other excitonic materials. These range from ultrafast pump-probe spectroscopic techniques such as transient absorption, which follows the fate of electronic excited states over time by measuring changes in sample absorption after an initial excitation on femtosecond to picosecond timescales [32–34], all the way to the continuous wave (CW) techniques such as those used to study fluorescence intermittency in single QDs [35] or photon-correlation Fourier spectroscopy used to measure single particle fluorescence linewidths [22]. Two main spectroscopic techniques will be used to study QDs in this thesis: time-resolved fluorescence spectroscopy, which is used to probe changes in the emission spectrum of QD ensembles as a function of time after excitation, and Raman spectroscopy, a CW technique used to understand how QD vibrational modes change according to their environment and other factors. Both of these types of spectroscopic experiments were implemented within a microscope, on spot sizes of $\sim$ 400 nm in diameter in the case of fluorescence experiments, to $\sim 1\mu$m in diameter for Raman experiments. The microscopy configuration results in better light collection efficiency than most free-space measurements.

2.1 Fluorescence Spectroscopy

In Chapter 3, the major technique used to study excitonic energy transfer between QDs in films is spectrally and temporally resolved fluorescence spectroscopy, which allows simultaneous knowledge of two key pieces of information: the ensemble fluorescence decay lifetime for any given wavelength/energy, and the ensemble fluorescence spectrum at any given time.

2.1.1 Fluorescence Lifetime and Quantum Yield

The fluorescence lifetime, τ, of a sample refers to the average time the molecule or material remains in the excited state, which can be measured by exciting a population of fluorophores simultaneously and then tracking how much light is emitted as a function of time after the initial excitation. For a typical experiment, a short laser pulse (much shorter in time than the dynamics of the system) excites a fraction of the sample fluorophores, resulting in an initial excited state population n_0. Over time, these excited states may decay radiatively (by emitting a photon) on non-radiatively (by energy transfer, charge trapping, phonon emission, etc.). The decay probability is constant in time, and the differential equation used to mathematically describe this behavior is

$$\frac{dn}{dt} = (k_r + k_{nr})\, n(t) \tag{2.1}$$

for $n(t)$ equal to the excited state population at time t, with k_r and k_{nr} the radiative and non-radiative decay rates, respectively. This differential equation has a solution of the form

$$n(t) = n_0 * e^{-(k_r+k_{nr})\,t} = n_0 * e^{-t/\tau}. \tag{2.2}$$

The lifetime τ of a molecule or material therefore represents the inverse of the sum of the radiative and non-radiative rates, and, for a population of identical emitters, the fluorescence decay should be single-exponential (i.e. having only one radiative and non-radiative rate). The experimentally measured intensity, $I(t)$, is related to the true population $n(t)$ through two constants: the collection efficiency (CE) of the

measurement apparatus, and the quantum yield (QY) of the sample:

$$I(t) = CE * QY * n(t). \tag{2.3}$$

The collection efficiency reflects the response of all parts of the experimental apparatus, including factors such as the reflectivity of mirrors, the efficiency of the spectrophotometer grating, and the response of the detector. The quantum yield is the sample brightness, the ratio of photons emitted to those absorbed. The quantum yield can also be written in terms of the radiative and non-radiative decay constants:

$$QY = \frac{k_r}{k_{nr} + k_r}. \tag{2.4}$$

Higher QY fluorophores emit light more efficiently by having shorter radiative lifetimes ($1/k_r$) than non-radiative lifetimes ($1/k_{nr}$), meaning that the molecule/QD fluoresces faster than the exciton can be trapped, transferred, or decay as heat.

2.1.2 Time-Correlated Single Photon Counting

The measurement of fluorescence lifetimes can be accomplished using either frequency-domain or time-domain techniques [36], the latter of which was used for this thesis. Time-Correlated Single Photon Counting (TCSPC) allows the measurement of fluorescence lifetimes through measuring photon arrival times at a detector, and then making a histogram of the measured arrival times. For this measurement, a short laser pulse excites a sample and triggers a clock within the TCSPC setup. At some point after the clock starts, a single photon hits the detector and its time is recorded. Performing this experiment millions of times leads to a distribution of photon arrival times that represents the fluorescence decay of the sample. A schematic describing this process is shown in Figure 2-1.

For this measurement, it is essential that only a single photon hits the detector for each laser pulse. TCSPC detectors are designed to only register one photon per triggering event, and often have a short 'dead' time after the photon measurement.

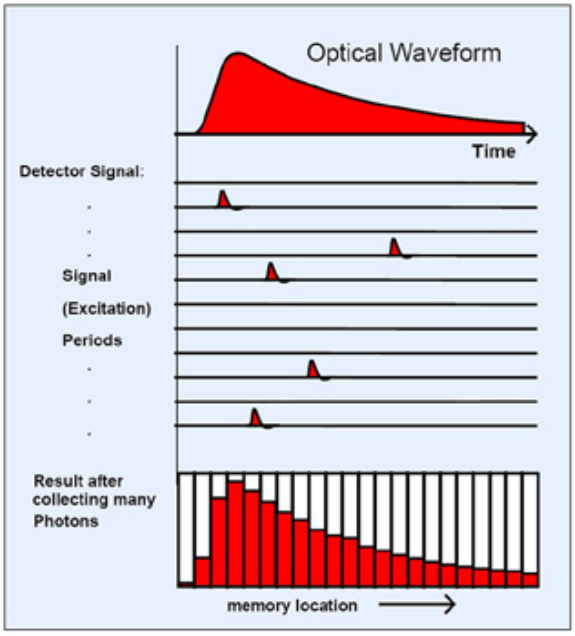

Figure 2-1: Schematic depiction of a TCSPC experiment. The fluorescence decay curve is approximated by making a histogram of millions of single photon experiments, where the arrival time of a single photon is repeatedly measured relative to the excitation pulse. The distribution of arrival times mirrors the true population fluorescence. Image from http://smos.sogang.ac.kr/wiki/index.php

If two photons were to hit the detector after a single laser pulse, the first would be recorded and the second ignored, leading to an over-representation of early photons. The number of photons (x) that reach a detector is a Poisson random variable, with a probability P given by the Poisson distribution

$$P(x = k) = \frac{\lambda^k e^{-\lambda}}{k!}, \tag{2.5}$$

with mean value λ. If, in a TCSPC experiment, the count rate (the number of photons detected per second) is equal to the pulse rate (number of pulses per second from the laser), one photon is expected per pulse. In this case, $\lambda = 1$, and the probability that *more than one* photon hits the detector ($x > 1$) for any given shot is 26%. For this reason, it is essential to maintain a count rate significantly below the pulse rate, represented schematically in Figure 2-1 by several experiments yielding zero photons. For the experiments in this thesis, the count rate in TCSPC experiments

was maintained at less than 5% of the pulse rate, yielding a 0.2% probability that two photons would arrive at the detector in the same shot.

2.1.3 Spectrally and Temporally Resolved Fluorescence Setup

The fundamental implementation of TCSPC involves exciting a fluorescent sample, then collecting and focusing all of the emitted light onto a detector to measure a lifetime. We improved upon this experiment through the addition of a spectrograph before the detector, which spectrally separates the emitted light from the sample and sends only light within a desired wavelength range to the detector. For this thesis, the experiment took place in a microscopy configuration, where the sample was placed on the sample stage of a Nikon Ti-U microscope, and both excitation and emission light passed through a 60x 1.4 NA oil-immersion objective. The sample was excited with a 405 nm diode laser (Picoquant) operating at 5 MHz. The instrument response function, which allows calculation of the 'zero' time and the temporal width of the excitation pulse, was measured using a mirror at the sample plane. Fluorescence was collected from the sample by the objective lens and then sent to a spectrograph (Princeton Instruments) with a 0.5 m focal length. The light was dispersed using a 300 grooves/mm grating, and a ~ 4 nm wavelength band was sent through the exit slit for detection by the avalanche photodiode (APD, PicoQuant). Over the course of the experiment, the spectral band reaching the APD was scanned and a lifetime was captured for each wavelength range. A schematic representation of this setup is shown in Figure 2-2.

2.2 Raman Spectroscopy

2.2.1 General Aspects

Raman spectroscopy is an inelastic light scattering technique used to measure vibrational energies within a sample. In the photon picture, light incident on a sample can experience one of several types of interactions: it can scatter elastically (leading to Rayleigh scattering), it can deposit some of its energy onto the crystal lattice such that

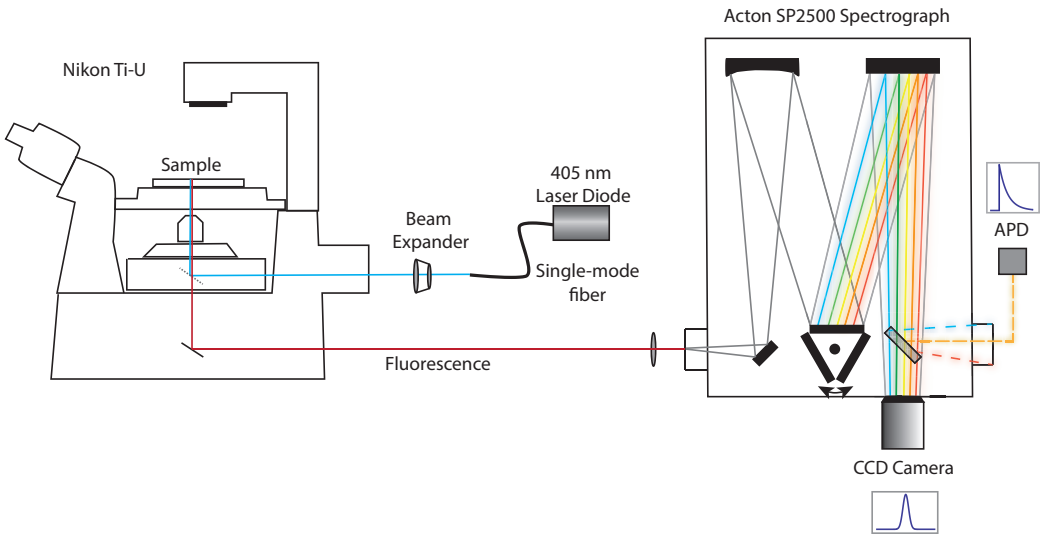

Figure 2-2: Schematic representation of spectrally resolved time-correlated single photon counting (SR-TCSPC) microscopy setup used to collect data for Chapter 3.

the scattered light is red-shifted compared to the incident light (Stokes scattering), or energy from a vibrational mode in the sample can be transferred to the photon so the scattered light is blue-shifted relative to the incident light (anti-Stokes scattering). In the latter two cases, the difference in energy between the incident and scattered light is equal to a vibrational quantum of energy (Figure 2-3a). By measuring millions of photons so that some photons scatter off all the vibrational modes of the sample, it is possible to measure a vibrational spectrum; a simple Raman spectrum of a sample with only one vibrational mode is shown schematically in Figure 2-3b. The Raman spectrum provides information both on mechanical properties of the material which affect the vibrational energies of a given peak, as well as the electronic properties of the material (band structure, ionicity/covalency of bond, etc.) which also determine the intensity of the peak through affecting the Raman scattering efficiency [37]. The intensity of the Stokes and anti-Stokes shifted light corresponds to the occupation of the vibrational modes, given by the Bose-Einstein distribution as discussed in Section 5.2.1. The intensities of the anti-Stokes (I_{AS}) and Stokes (I_S) peaks in the Raman

spectrum are therefore approximately given by

$$I_{AS} \propto \frac{1}{e^{h\nu_{vib}}/kT - 1} \tag{2.6}$$

$$I_S \propto \frac{1}{e^{h\nu_{vib}}/kT - 1} + 1 \tag{2.7}$$

for phonons with vibrational frequency ν_{vib}. The factor +1 comes into the Stokes equation from the phonon creation operator, which allows for Stokes scattering even at zero occupation of the vibrational mode [38].

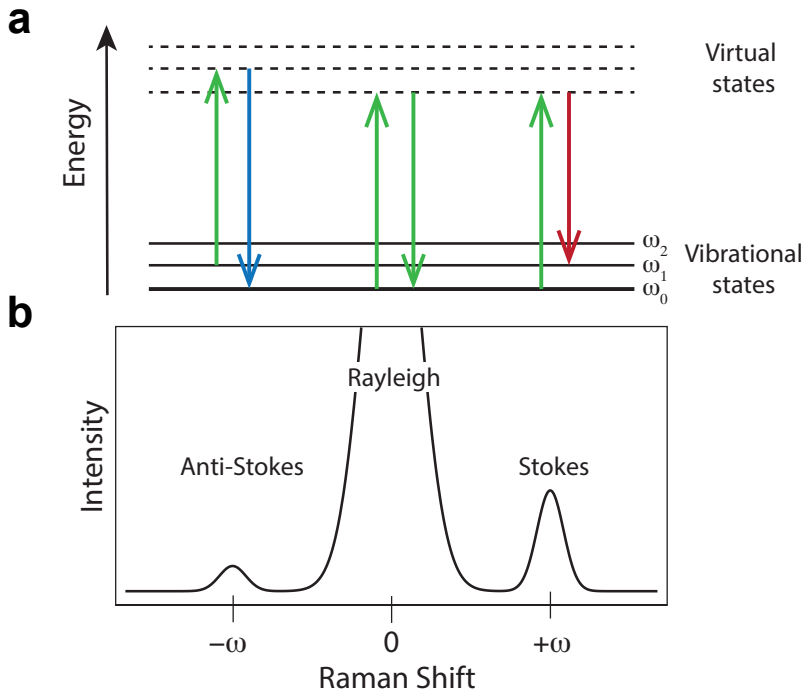

Figure 2-3: Schematic depiction of Raman spectroscopy in the photon picture. a) An incident photon (green arrow) excites a sample to a 'virtual state' (not an electronic transition, except in the case of resonant Raman spectroscopy), and the scattered photon (right of green arrow) either gains energy from a vibrationally excited sample resulting in blue-shifted light or loses energy to excite a vibration in the sample resulting in red-shifted light. b) Schematic Raman spectrum depicting Stokes, anti-Stokes, and Rayleigh scattered light.

Raman scattering can also be described classically using wave formalism for light without the need to call upon the 'virtual states' in a sample depicted in Figure 2-3a,

which, importantly, reveals the origin of the selection rules for Raman spectroscopy. In this picture, an incident photon with frequency ν_0 and amplitude E_0 interacts with a sample to create a polarization $\mathbf{P}$ according to the polarizability tensor α of the sample:

$$\mathbf{P} = \alpha\, E_0 cos(2\pi\nu_0 t). \tag{2.8}$$

The molecular polarization creates an induced dipole that oscillates with frequency ν_0, which can radiate light at frequency ν_0. This is light scattering mechanism does not change the frequency (energy) of the incident light, and represents the elastic Rayleigh scattering mechanism. However, if the molecular polarizability tensor α is time-dependent, other scattering mechanisms become possible [39]. If the atoms within a sample are vibrating, the coordinate describing atomic displacement Q will change as a result of the phonon by an amount dQ

$$dQ = Q_0\, cos(2\pi\nu_{vib} t), \tag{2.9}$$

where Q_0 is the maximum vibrational amplitude, and ν_{vib} is the vibrational (phonon) frequency. The polarizability α can be represented as a Taylor's series for small displacements dQ:

$$\alpha = \alpha_0 + \left(\frac{\partial\alpha}{\partial Q}\right)_{Q_0} dQ, \tag{2.10}$$

where α_0 is the polarizability of the material at its equilibrium position. If Equation 2.9 is substituted into Equation 2.10, then

$$\alpha = \alpha_0 + \left(\frac{\partial\alpha}{\partial Q}\right) Q_0\, cos(2\pi\nu_{vib} t). \tag{2.11}$$

This can in turn be substituted into Equation 2.8 to yield

$$\mathbf{P} = \alpha_0 E_0 cos(2\pi\nu_0 t) + \left(\frac{\partial\alpha}{\partial Q}\right) Q_0 E_0\, cos(2\pi\nu_0 t)\, cos(2\pi\nu_{vib} t). \tag{2.12}$$

Using a trigonometric product-to-sum formula, this can finally be re-written as

$$\mathbf{P} = \alpha_0 E_0 cos(2\pi\nu_0 t) + \left(\frac{\partial\alpha}{\partial Q}\right)\left(\frac{Q_0 E_0}{2}\right)(cos[2\pi(\nu_0 - \nu_{vib})t] + cos[2\pi(\nu_0 + \nu_{vib})t]). \tag{2.13}$$

Equation 2.13 describes the classically oscillating dipole emitting the Rayleigh frequency ν_0 along with dipoles oscillating at frequencies $\nu_0 - \nu_{vib}$ and $\nu_0 + \nu_{vib}$. These latter two emitted frequencies are the Raman scattered waves, corresponding to the Stokes and anti-Stokes scattered light, respectively, which differ in frequency from the incident light by the amount $\pm\nu_{vib}$ (Figure 2-4). As in the photon picture, in the case where the Stokes frequency is emitted, energy from the incoming light is used to excite a vibrational mode in the sample at $\nu = \nu_{vib}$, while the anti-Stokes frequency corresponds to the case where a pre-existing vibrational mode of the sample (again with frequency $\nu = \nu_{vib}$) gives its energy to the scattered light. Thus, the light scattered from a sample is expected to include a very intense Rayleigh peak as well as two Raman peaks per vibrational mode in the sample as is illustrated schematically in Figure 2-3.

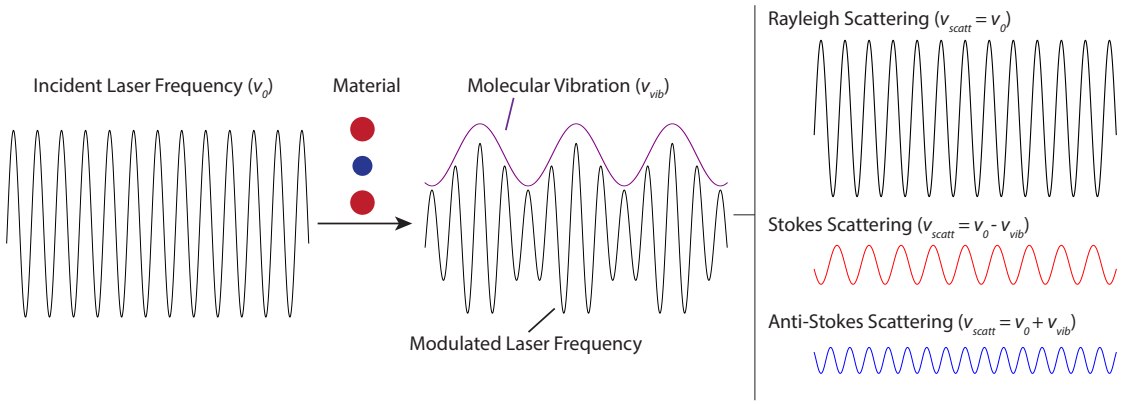

Figure 2-4: An incident electromagnetic wave with a given frequency interacts with a molecular sample. A vibrational mode of the sample with frequency ν_{vib} modulates the laser frequency, and the modulated waveform as frequency components at ν_0, $\nu_0 - \nu_{vib}$ (Stokes scattered, redshifted) and $\nu_0 + \nu_{vib}$ (anti-Stokes scattered, blueshifted).

The wave formalism for Raman scattering yields an important result: only vibrations that result in a change in polarizability, $\partial\alpha/\partial Q \neq 0$, are Raman active.

This selection rule comes from Equation 2.13, where the terms involving light frequency shifts only appear for non-zero $\partial\alpha/\partial Q$. Vibrations that result in a change in polarizability tend to be symmetric, unlike the infrared-active vibrations that result in a change in dipole moment. This property can be thought of pictorially as in Figure 2-5, where the symmetric vibration results in a stretching of the electron 'sack' that corresponds to the polarization of the molecule while the anti-symmetric vibration does not result in any dilation of the same polarizability ellipsoid. Indeed, the Raman spectra collected for QDs and discussed at length in Chapter **??** are symmetric vibrations of the whole nanocrystal.

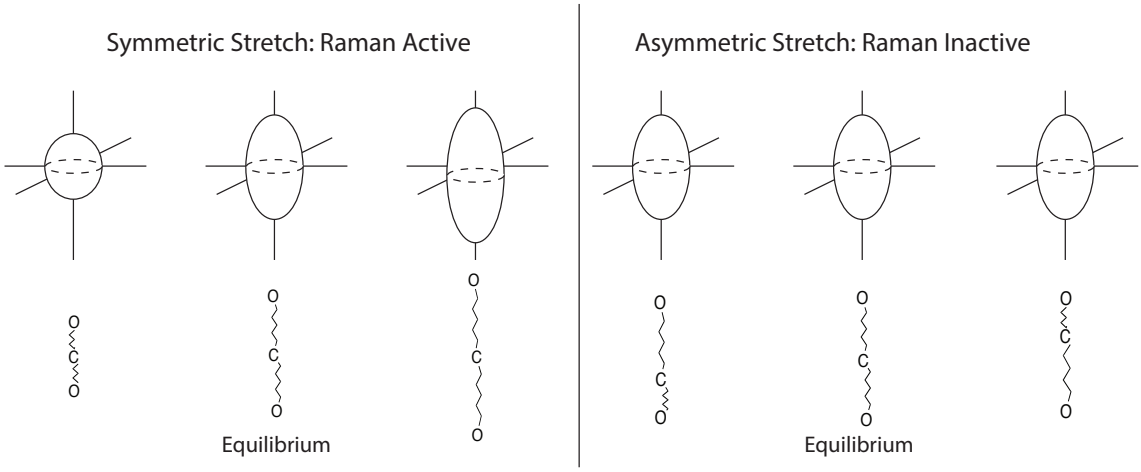

Figure 2-5: Changes in polarization of a molecule or quantum dot can be thought of as motion of the 'bag of electrons', or polarizability ellipsoid. *Left*: The polarizability ellipsoid changes shape (i.e. $\partial\alpha/\partial Q \neq 0$) for a symmetric vibration of the linear molecule CO_2. *Right*: The polarizability ellipsoid does not change shape for the antisymmetric vibration, which is not Raman-active.

2.2.2 Momentum Conservation in Raman Spectroscopy

The law of energy conservation is clearly inherent to the photon picture of Raman scattering in Figure 2-3, where the energy of the scattered photon, $\hbar\omega_s$, is shifted by the phonon energy, $\hbar\omega(\mathbf{k})$, from the incident photon energy, $\hbar\omega_i$ (i.e. $\hbar\omega_s = \hbar\omega_i \pm \hbar\omega(\mathbf{k})$); more subtly, the law of conservation of momentum determines which phonons can be observed through light scattering. Conservation of momentum

requires

$$\hbar\mathbf{q}_s = \hbar\mathbf{q}_i \pm \hbar\mathbf{k} \tag{2.14}$$

for photon wavevector $\mathbf{q}$, phonon wavevector $\mathbf{k}$. Even very high energy photons have very small $\mathbf{q}$ due to the dispersion relation of light (with slope equal to the speed of sound). Typical phonons have energy much smaller than photons, and can only shift the energy of the photon by a small amount, leaving $\mathbf{q}_s$ very similar to $\mathbf{q}_i$; in other words, $\mathbf{q}_s - \mathbf{q}_i \approx 0$. For this reason, only phonons with very small $\mathbf{k}$ scatter light, and so Raman scattering is often referred to as a 'zone-center' phonon measurement technique. This can alternatively be rationalized by comparing the magnitude of a typical photon wavevector (order 10^5 cm^{-1}) with the size of the Brillouin zone (order 10^8 cm^{-1}), which also suggests that photons can only probe phonons with $\mathbf{k} \sim 0$.

Momentum conservation rules also provide information about the scattering angle θ in Raman experiments. Figure 2-6 schematically depicts the Raman scattering interaction between a phonon and a photon, where θ depends on the phonon wavevector $\mathbf{k}$ [40]:

$$\mathbf{k} = (\mathbf{q}_i^2 + \mathbf{q}_s^2 - 2\mathbf{q}_i\mathbf{q}_s\cos[\theta])^{\frac{1}{2}}. \tag{2.15}$$

Typically, interaction with phonons changes $\mathbf{q}_i$ by very little, thus $\mathbf{q}_i \approx \mathbf{q}_s = \mathbf{q}$, and Equation 2.15 can be written

$$\mathbf{k} = 2\mathbf{q}\sin[\theta/2]. \tag{2.16}$$

In this thesis, all Raman scattering experiments are conducted using the backscattered geometry, which means θ is close to π. This geometry maximizes $\mathbf{k}$ for a given $\mathbf{q}$, though $\mathbf{k} << \mathbf{q}$.

Though linear momentum is always conserved, in the particular case of nanostructures or glassy/amorphous materials, the momentum conservation of Equation 2.14 may break down. For those materials, the crystallite or domain size is so small that Bloch's theorem cannot be applied, and the phonon wavevector $\mathbf{k}$ is no longer be a good quantum number for the system. In this case, the Raman scattering intensity reflects the vibrational density of states for the material [41]. For this reason, the 'zone center' selection rule for Raman spectroscopy may not always

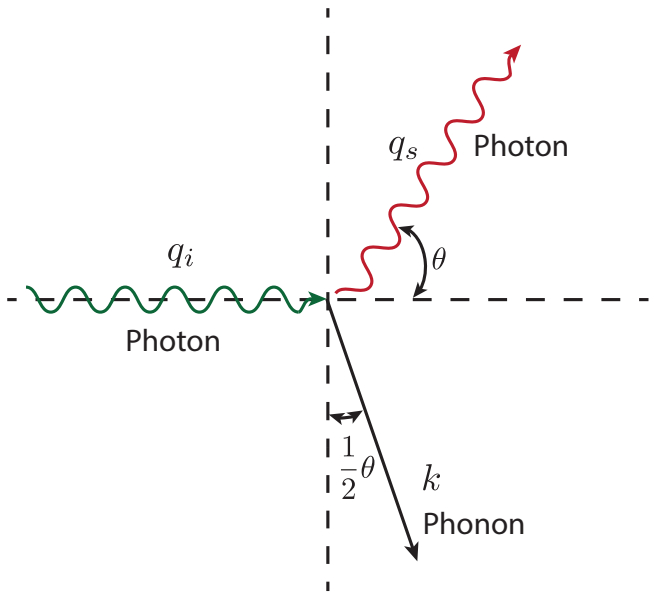

Figure 2-6: Schematic of Stokes Raman scattering process, where a phonon is emitted after the interaction of a photon with a sample, and the scattered photon is redshifted. Wavevector conservation indicates $q_i = q_s + k$. The scattering angle θ is described in the main text.

apply for the measured vibrational modes of QDs.

2.2.3 Details of Low-Frequency Raman Microscope Setup

The particular microscopy setup used to measure Raman spectra for QD nanoparticles in this thesis is drawn schematically in Figure 2-7. In this setup, a wavelength-stabilized 785 nm diode laser provided the excitation source, which passed through several amplified spontaneous emission (ASE) cleanup filters before reaching the sample mounted on a Nikon Ti-U microscopy stage. At the sample, the average laser power used was about 5 mW/μm^2. After reaching the sample, backscattered light was collected using a 0.6 NA 40x objective, fitted with a correction collar that allows it to work with up to 2 mm of glass between the objective and the sample, important for the microscopy cryostat measurements discussed in Chapter 5. After collection, the scattered light was sent through the same beam path as the incident radiation until reaching the volume holographic grating (VHG) beamsplitter. In the forward

direction, this optic acts as an additional ASE filter, reflecting light at the excitation frequency by 10°; in the reverse direction, it passes Raman scattered light shifted from 785 nm. After the beamsplitter, the scattered light passes through a VHG notch filter of width ± 5 cm^{-1} with optical density 10^{-8} at the excitation frequency. All ASE and VHG filters were built to be paired with the 785 nm laser and were purchased from Ondax. After the VHG notch filter, Raman scattered light was dispersed in a 0.5 m focal length spectrograph using a 1200 grooves/mm grating with 750 nm blaze, and the spectrum was imaged onto a cooled CCD camera.

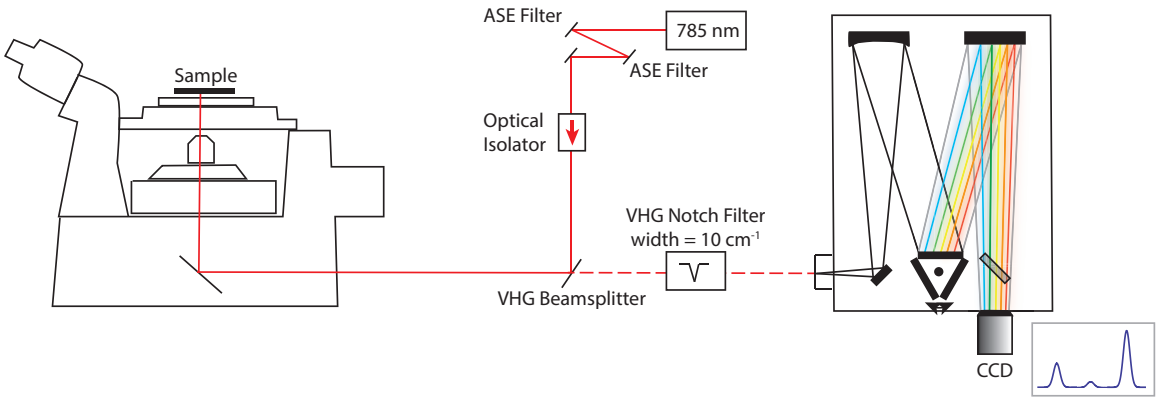

Figure 2-7: Schematic setup for low-frequency Raman measurements of nano materials used for this thesis. The wavelength-stabilized laser, ASE filters, VHG beamsplitter, and VHG notch filter are labeled. The sample on the microscope stage can optionally be placed in a cryostat for low temperature measurements. The spectrograph disperses the Raman scattered light to collect a spectrum at the CCD.

Chapter 3

Förster Resonant Energy Transfer in CdSe Nanocrystal Solids

Much of Chapter 3 has appeared in print as Mork, Weidman, Prins, and Tisdale, *J. Phys. Chem. C* (2014), [42].

3.1 Introduction

As mentioned in Chapter 1, energy transfer must be considered in the design of QD-based devices as it plays a significant role in the fluorescence properties of QD films. In general, energy transfer is the process of transferring of an excited state (an exciton) from one atom/molecule/QD (the "donor") to another (the "acceptor"). The process can be simply written

$$D^* + A \rightarrow D + A^* \tag{3.1}$$

where the excited state is indicated by the asterisk. In QD films, many energy transfer events can occur sequentially, yielding exciton diffusion through a "hopping" type mechanism. Intentionally engineering exciton diffusion in QD solids requires a fundamental understanding of the energy transfer mechanism, and the underlying factors that determine the energy transfer rate.

This Chapter will begin with a general introduction to equations governing

(excitonic) energy transfer, and this background will be used to interpret time-resolved fluorescence data for homogeneously blended QD films of donor QDs with one of two types of acceptor that vary only in the surface ligand (Figure 3-1). From these data, we extract the characteristic distance over which energy transfer occurs, and discuss often overlooked factors that may play a role in energy transfer in close-packed QD devices.

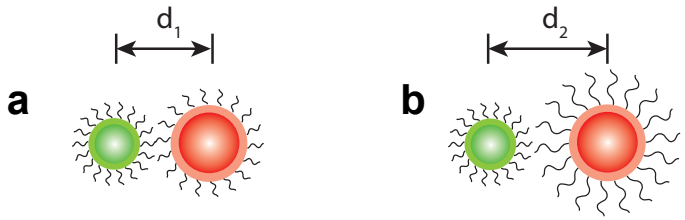

Figure 3-1: Schematic of materials used for energy transfer study in QD films. a) Donor paired with short-ligand acceptor, with interparticle distance d_1. b) Donor paired with long-ligand acceptor with interparticle distance d_2.

3.2 Energy Transfer Mechanisms: Theory

Energy transfer can take one of two principle forms, Dexter or Förster, which have different mechanisms and operate on different length scales. Dexter energy transfer (also called exchange energy transfer) involves the tunneling of an excited electron from a donor to an acceptor and the back transfer of a ground state electron from the acceptor to the donor to yield the de-excited donor and excited acceptor of Equation 3.1 (Figure 3-2). Because this process involves the quantum mechanical tunneling of electrons, it requires wavefunction overlap between the donor and acceptor which can only occur at very small donor-acceptor spacings, though the transferred excited state can be either a triplet or a singlet. The energy transfer rate for Dexter-type energy transfer processes scales exponentially with distance; as a result, Dexter energy transfer is typically only efficient for donor-acceptor distances of < 2 nm [43]. In the case of QDs, the inter-particle spacing is often greater than the distance over which Dexter energy transfer is efficient, and so this mechanism is generally considered to

play a negligible role in energy transfer in QDs compared to energy transfer that occurs though the Förster Resonant Energy Transfer (FRET) mechanism.

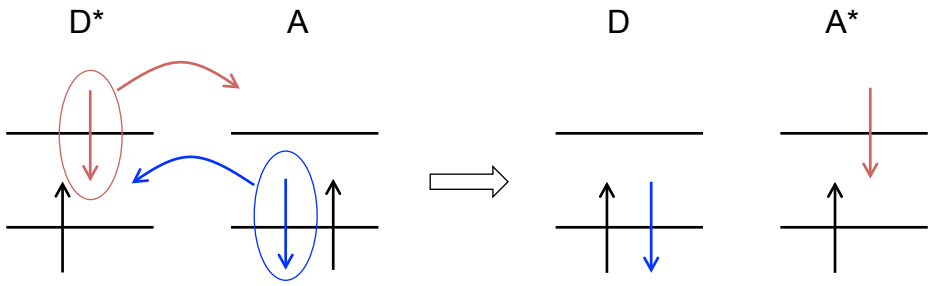

Figure 3-2: Schematic of Dexter energy transfer. An excited donor molecule transfers an electron to an acceptor (red) while the acceptor transfers an electron back to the donor (blue).

FRET does not require tunneling of charges through any potential barrier, and therefore does not have the orbital overlap and length scale constraints of Dexter transfer; rather, FRET involves the transfer of a 'virtual photon' from the donor to the acceptor, resulting in the de-excitation of the former and the excitation of the latter (Figure 3-3). The overall process is exactly analogous to emission-reabsorption, where a donor emits a photon that is absorbed by an acceptor, and in both cases the only type of excitation that can be transferred is a singlet exciton. The rest of this section will discuss the important aspects of the mathematics describing Förster resonance energy transfer, and develop an intuition for the guiding equations [44].

FRET is fundamentally a dipole-dipole interaction, which takes place in the near field at length scales for which the transition dipole of the donor and acceptor molecules can be treated using the ideal dipole approximation. In this case, the distance between the individual dipoles is large compared to their extent, and the dipole-dipole interaction potential, V, between the donor and acceptor dipoles, $\vec{\mu_D}$ and $\vec{\mu_A}$, has a $1/r^3$ dependence:

$$V = \frac{\vec{\mu_A} \cdot \vec{\mu_D} - 3(\vec{\mu_A} \cdot \hat{r})(\vec{\mu_D} \cdot \hat{r})}{(4\pi\epsilon_0 n^2)\, r^3}. \tag{3.2}$$

Here, $\hat{r}$ is the vector between the donor and acceptor point dipoles, ϵ_0 is the

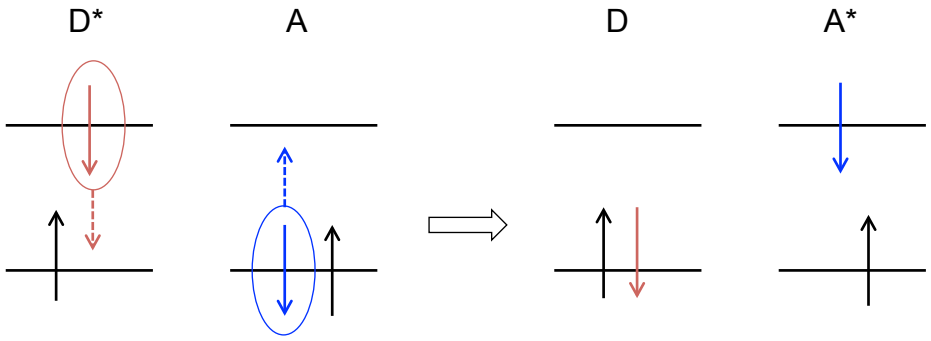

Figure 3-3: Schematic of FRET. An excited donor molecule relaxes and its energy is transferred non-radiatively to an acceptor. Unlike Dexter transfer, the electrons remain on the same molecule (compare final positions of red and blue arrows to Figure 3-2).

permittivity of free space, and n is the dielectric constant for the medium that separates the dipoles. The numerator of this interaction potential is the orientation factor κ, which describes how the transition dipoles of the donor and acceptor are related to each other and to the vector between them. Often, κ is written in terms of θ_D, the angle between the donor dipole and $\hat{r}$, θ_A, the angle between the acceptor dipole and $\hat{r}$, and θ_T, the angle between the donor and acceptor dipoles (Figure 3-4):

$$\kappa = \cos(\theta_T) - 3\cos(\theta_D)\cos(\theta_A). \tag{3.3}$$

In the quantum mechanical picture of Förster theory, the interaction potential V can be used in the context of perturbation theory to determine the energy transfer rate from a donor to an acceptor. In this case, the initial state is written $|D^*A\rangle$ and the final state $\langle DA^*|$, yielding (through Fermi's golden rule)

$$k_{ET}(w_D, w_A) = \frac{1}{h}\int \langle DA^*|V|D^*A\rangle^2 dw \tag{3.4}$$

where k_{ET} is the energy transfer rate from donor to acceptor, w_D and w_A refers to to the initial energy of the donor and acceptor, and dw integrates over all possible values of the transferred energy.

There are various ways convert Equation 3.4 into a form more easily calculated

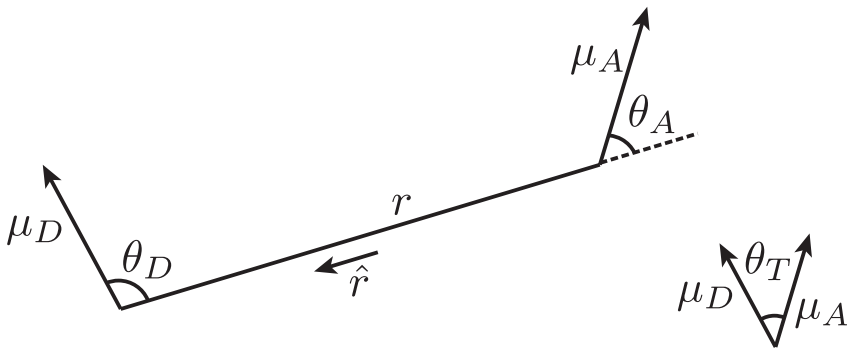

Figure 3-4: Illustration of relevant vectors and angles in the calculation of the dipole potential and κ (Equations 3.2 & 3.3). The relative orientation of the transition dipoles of two molecules, as well as the distance between them, plays a role in the dipole coupling strength.

using experimental observables, and the specifics of the derivation will be skipped here in favor of an intuitive analysis of the result (for two different derivations, see [44] and [45]). The result of performing the integration suggested in Equation 3.4 and converting to units of wavelength (λ) yields a relatively simple equation for k_{ET} that relies on the donor lifetime τ_D with scaling d^{-6}:

$$k_{ET} = \frac{1}{\tau_D}\left(\frac{R_0}{d}\right)^6, \tag{3.5}$$

for

$$R_0^6 = \frac{9\,\eta_{PL}\,\kappa^2}{126\pi^5\,n^4}\int \lambda^4 F_D(\lambda)\sigma_A(\lambda)d\lambda. \tag{3.6}$$

The constant R_0 is called the "Förster radius" and has units of inverse distance. The equation for the Förster radius includes the quantum yield of the donor, η_{PL}, the orientation factor, κ, the refractive index, n, and the overlap integral which describes the overlap between the donor emission F_D and the acceptor absorption σ_A. The calculation of the overlap integral requires the donor emission spectrum to be normalized to its total integrated area while the acceptor absorption spectrum is in units of absorption cross section (giving R_0 the desired units of nm^6 for Equation 3.5).

The Förster radius is the distance at which the energy transfer rate k_{ET} equals the total decay rate of the donor, $k_D = 1/\tau_D$, due to all other de-excitation pathways (radiative and non-radiative), and provides a metric to understand the distances over which energy transfer is efficient (Figure 3-5). For donor-acceptor distances larger than R_0, other de-excitation pathways are faster than energy transfer, and it contributes weakly to the dynamics of the system. For distances on the order of R_0, energy transfer cannot be neglected when engineering or understanding an excitonic system. The rest of this Chapter will describe the use of spectrally resolved time-correlated single photon counting methods to understand energy transfer in mixed donor-acceptor QD films in order to extract a Förster radius for this system.

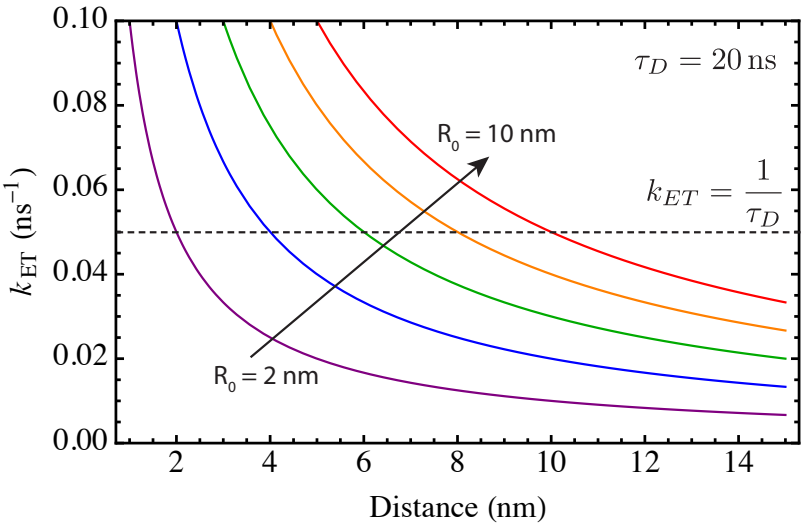

Figure 3-5: Plot of energy transfer rate as a function of donor-acceptor distance for several values of R_0 (2–10 nm in 2 nm increments), assuming a donor lifetime in the absence of energy transfer (τ_D) equal to 20 ns (a typical value for QDs). Horizontal line indicates when the energy transfer rate equals the rate of de-excitation due to other pathways.

3.3 Background for Energy Transfer in QD-based Systems

Several biological assays rely on energy transfer between QDs and organic chromophores in solution, where the proximity of the donor and acceptor can be inferred from the energy transfer efficiency, and in this context FRET has been well

established as a theoretical and practical framework for understanding energy transfer in solution [46–48]. However, recently several laboratories have reported anomalously large polarization effects in QD films, which affect parameters such as the film QD absorption spectrum [49, 50]. These studies raise important questions about how energy transfer in close-packed QD films may differ from energy transfer between QDs and molecules in solution. Additionally, the donor-acceptor distance, and therefore R_0, is typically assumed to measure the center-to-center distance between a donor-acceptor pair. This approximation is usually valid for small molecules, where the point-dipole approximation is reasonable. However, for QDs, the "molecule" itself has significant extent, and it is not clear *a priori* whether the center-to-center or edge-to-edge or some other distance is most relevant for understanding energy transfer properties in QD materials [51, 52].

There are two key indicators of energy transfer in donor-acceptor systems: lifetime shortening of the donor, and spectral redshift to approximate the acceptor emission spectrum (Figure 3-6). The first indicator results from the additional recombination pathway that exists for donors, which means the donor decay rate, k_D, increases in magnitude by an amount equal to the sum of all the energy transfer rates to acceptors:

$$k_D = k_r + k_{nr} + \sum k_{ET}, \tag{3.7}$$

where k_r and k_{nr} are the native radiative and non-radiative lifetimes of the donor, respectively (Figure 3-7). For QDs in particular, the spectral indicator of energy transfer can be observed even in films of only "donor" QDs due to polydispersity. Within the same inhomogeneous population, some QDs will have lower band gaps than others, and over time the exciton population will diffuse to the larger, lower band gap QDs, resulting in a redshift of the spectrum [53].

Prior experiments in solid films have measured the energy transfer rate between donor and acceptor QDs by monitoring the donor fluorescence lifetime in either blended donor-acceptor films [54–56] or in bilayer structures [57, 58]. For both geometries, measured energy transfer rates fall in the range between $1 - 10 * 10^8$

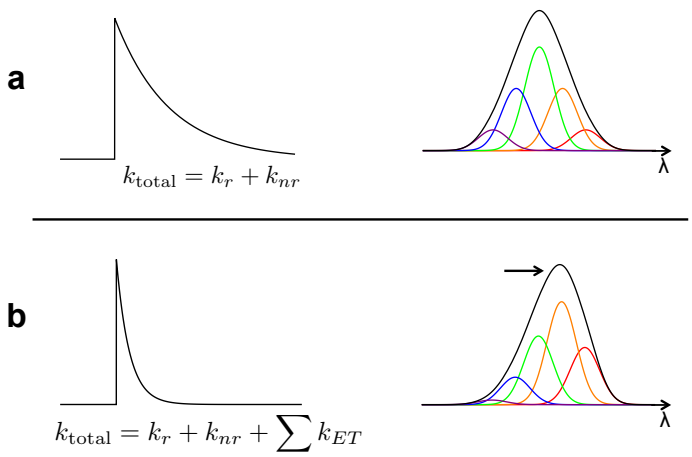

Figure 3-6: a) No energy transfer case. Lifetime is dictated by native radiative and non-radiative rates, and QD ensemble emission spectrum is symmetric and reflects all QD sizes present in sample. b) Energy transfer case. Lifetime is shortened due to an additional energy transfer decay rate, and the QD ensemble spectrum is redshifted to over-represent the lower band-gap dots in the sample (represented by the smaller colored Gaussians).

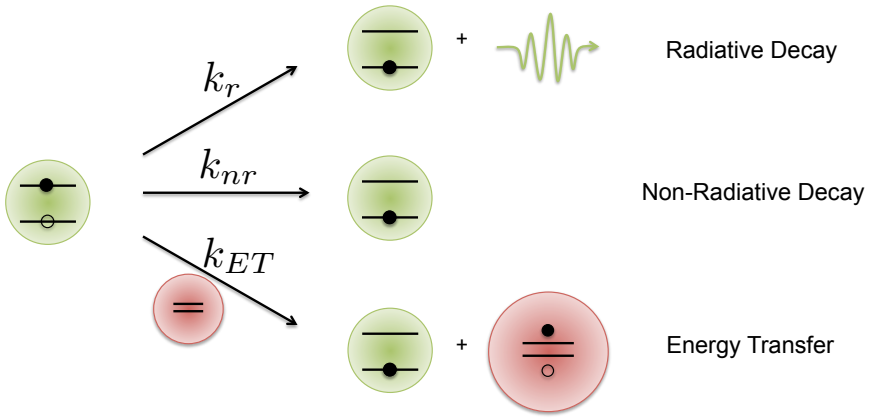

Figure 3-7: An excited donor (left) can undergo several methods of de-excitation, including radiative decay with rate k_r that results in the emission of a photon, non-radiative decay with rate k_{nr} through methods such as coupling to a thermal bath, and energy transfer with rate k_{ET} that results in an excited nearby acceptor.

s^{-1}. Changes in the deposition technique (drop casting vs. Langmuir-Blodgett) [57], as well as changes in the spacing between donor and acceptor layers using polymer spacers [58] or ligands of different lengths [59] have been shown to affect k_{ET} by altering the proximity of nearest neighbor acceptors. Similarly, for energy transfer

within an inhomogeneous distribution of QDs, the linewidth and Stokes shift of QDs affect the energy transfer rate from small QDs (larger band gap) to large QDs (smaller band gap), consistent with the expected dependence of spectral overlap on the energy transfer rate predicted by Förster theory [60]. These experiments have revealed that FRET theory correctly predicts some scaling parameters that affect the energy transfer rate in QD solids, such as overlap integral and inter-particle separation. These studies have primarily used fits to the donor fluorescence lifetime to extract FRET parameters, and few have measured the actual inter-particle separation or rigorously calculated the spectral overlap to test the limits of Förster theory as it applies to QD solids.

3.4 Experimental Methods

3.4.1 Materials

CdSe/CdZnS nanocrystals were supplied by QD Vision, Inc., and were used as received. QD materials were kept under inert atmosphere during all handling and experimentation. QD solutions were prepared with anhydrous solvents purchased from Sigma Aldrich. All QD cores are CdSe with an overcoated CdZnS shell. Additional details pertaining to these QD materials, including the synthesis procedure, can be found in the previous publication by Dang, et al.6 TEM analysis revealed that the donor QDs used for this study were 4.0 ± 0.5 nm in diameter, with a center-to-center distance in pure close-packed monolayers of 6.0 ± 0.9 nm. Two types of acceptor QDs were paired with the donor in energy transfer studies: one acceptor had a long-chain aliphatic ligand and the other had a shorter aromatic ligand. The acceptor QDs were synthesized identically except for the ligand introduced during overcoating; see Dang *et al.* for further details [61]. From TEM images of pure close-packed films, the short-ligand acceptor had a diameter of 5.5 ± 0.5 nm with mean center-to-center separation of 8 ± 1 nm, while the long-ligand acceptor had a diameter of 5.3 ± 0.5 nm with mean center-to-center separation of 9 ± 1 nm.

3.4.2 Sample Preparation

Molar concentrations of QDs were estimated using the method of Yu, *et al.*, based on the band-edge absorption wavelength and intensity [62]. Donor/acceptor mixtures were prepared by adding approximately equal moles of each QD species, as determined by absorption measurements, and diluting to the desired concentration. QD films used for this study were prepared in a nitrogen-filled glovebox by spin casting 5mg/ml solutions of QDs in toluene onto a cleaned glass slide that was previously treated with mercaptopropyl trimethoxysilane, resulting in films approximately 20 nm thick. After spin coating, the samples were packaged in inert atmosphere for removal from the glovebox by placing the QD slide face-down onto a clean glass slide and sealing the edges with epoxy.

3.4.3 TEM and X-ray Analysis of Blended Samples

Transmission electron microscopy (TEM) was used to determine the average center-to-center distance between donors and acceptors in blended QD films. Images were taken on a JEOL 2011 operated at 200kV and using an objective aperture to increase mass-thickness contrast. Samples for TEM analysis were prepared by drop casting the donor/acceptor mixture onto a copper TEM grid with amorphous carbon support film. The donor/acceptor mixtures were diluted such that a monolayer was formed on the TEM grid, allowing for identification of individual QDs. TEM images were processed using ImageJ then analyzed in Matlab. First, an FFT bandpass filter was applied to the image, which served to better distinguish the edges of the nanocrystals from the carbon support [63]. The brightness/contrast of the image was then maximized, followed by conversion from grayscale to black-and-white. Next, particles were indexed and tabulated according to the coordinates of their center-of-mass, and the area was used to calculate an effective diameter for each particle. Artifacts of the image processing algorithm that were clearly not individual QDs were rejected based on size or shape. By plotting the histogram of all diameters in an image, two peaks could be resolved which correspond to the two different

sizes of QDs present in the mixture (Figure 3-8. We assigned a threshold diameter between these two peaks, creating a population of "small" QDs (diameters less than the threshold) and "large" QDs (diameters greater than the threshold). Using the centroid location of each particle in the image, it was then possible to compute center-to-center distances between every pair of QDs, including the case of interest here, which is the distance between "small" (donor) and "large" (acceptor) QDs. The first peak in the histogram of donor-acceptor distances (Figure 3-8) represents the average nearest neighbor center-to-center distance between each donor and acceptor. The width of this peak represents the distribution of different center-to-center distances present in the ensemble.

The determination of the QD center-to-center distance by TEM was complemented by grazing-incidence small-angle X-ray scattering (GISAXS) analysis of spin-cast 3D films. GISAXS measurements were performed at the undulator-based X9 beamline at the National Synchrotron Light Source at Brookhaven National Laboratory. The X-ray energy was set to 14.1 keV (wavelength 0.0879 nm), and the beam size was focused to 50 μm tall by 100 μm wide at the sample position using a KB mirror system. Because of the grazing incidence, beam projection along the beam direction was $\sim$ 1 cm. The grazing incident angle of the X-ray beam was varied from 0.07° to 0.3°. The presented results are for 0.15°, which were found to be representative. 2D scattering data were collected using a Pilatus 1M detector which was calibrated using a silver behenate standard. The QD films used for GISAXS were prepared as described in Section 3.4.2. The interparticle spacing was extracted from a given scattering pattern by taking a line cut along the in-plane scattering direction (q_y) and the Yoneda peak (streak of high intensity just above the sample horizon in Figure 3-8) [64].

3.4.4 Spectrally Resolve Transient Photoluminescence Spectroscopy

Prepared samples were measured using the setup described in Chapter 2 Section 2.1.3. All spectra were corrected for the spectral sensitivity of the detection system using a calibrated tungsten halogen lamp. Data were collected from multiple locations on

each sample and averaged together to obtain statistically representative results.

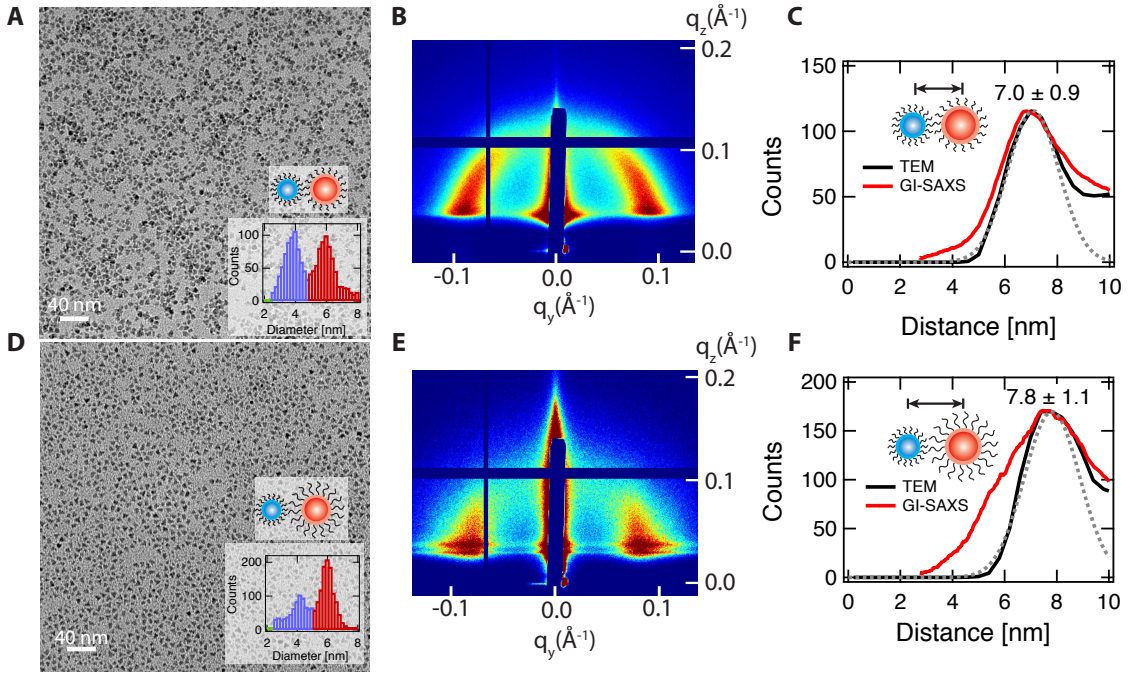

Figure 3-8: TEM and GISAXS measurements of donor-acceptor separation. (A - C) Short-ligand acceptor. (D - F) Long-ligand acceptor. (A, D) TEM micrographs of donor-acceptor blended samples, with insets illustrating the corresponding donor-acceptor pair and size histogram revealing the approximately equimolar bimodal distribution in QD sizes. Scale bar = 40 nm. (B, E) GISAXS patterns for blended 3D films. (C, F) Histograms of the measured nearest-neighbor interparticle distance (Gaussian fit to TEM data indicated with dotted gray line), demonstrating good agreement between TEM and GISAXS measurements.

3.5 Observations of Energy Transfer and Calculation of the Energy Transfer Rate

3.5.1 Donor-Acceptor Distance Changes According to Ligand Length

A key contribution of the work to be described in this Chapter is the careful modulation and characterization of the donor-acceptor distance (Figure 3-1) that produces observed changes in fluorescence characteristics of blended QD films. The TEM measurements of Figure 3-8 reveal that the donor and acceptor species are

mostly homogeneously mixed (see Section 3.6.1 for a discussion of possible effects of incomplete mixing), and that changing the acceptor ligand from benzylphosphonic acid to octadecylphosphonic acid does indeed alter the interparticle separation. As described in Section 3.4.3, through image processing of TEM micrographs the donor and acceptor populations could be separately identified (see insets of Figure 3-8), and the nearest-neighbor donor-acceptor distance calculated. The radial distribution function (a histogram of nearest neighbor distances) for the specific donor-acceptor distance is the black line of Figure 3-8 C & F. Statistical analysis of the TEM micrographs revealed that the donor-acceptor separation for the case where the acceptors were capped with short ligands was 7.0 ± 0.9 nm, while the separation for the long-ligand acceptor case was 7.8 ± 1.1 nm. This yields an average 0.8 nm difference in the center-to-center distance between donors and acceptors in the two types of films used for this measurement. It is worth noting that TEM analysis was performed on monolayer samples, while spectroscopic measurements were performed on multilayer films. In order to verify reasonable donor-acceptor distances were calculated from TEM images, we compare to the interparticle separation measured using GISAXS on films prepared in the same way as those used for fluorescence lifetime measurements. The GISAXS data cannot distinguish between donor-donor, donor-acceptor, and acceptor-acceptor interparticle distances, which leads to the broader distribution function measured using this method. The excellent agreement between TEM and GISAXS data inspires confidence in our quantification of the donor-acceptor spacing as well as our understanding of its statistical variation within the sample.

3.5.2 Donor Fluorescence Quenching

The first indication of energy transfer within donor-acceptor films is the quenching of donor fluorescence, which is due to the reduced lifetime of the donors as the excitation is transferred to acceptor QDs. For the materials used here, the emission spectrum of the donor overlaps with the second absorption feature of both acceptors (Figure 3-9), indicating that the spectral overlap required from Equation 3.6 is satisfied and energy transfer should be possible. Indeed, the ratio of donor to acceptor emission

intensity in a steady-state fluorescence measurement decreased upon deposition from a mixed solution to a film (corresponding to a substantial decrease in average donor-acceptor distance from effectively infinite distance to the values determined through TEM/GISAXS analysis) (Figure 3-9). In particular, the reduction in the relative donor fluorescence is more significant for donors in the presence of the short-ligand acceptor than the long-ligand acceptor, qualitatively confirming initial expectations that the ligand length may be used to control energy transfer efficiency between donors and acceptors in otherwise identical materials. The spectral properties of the donor and acceptor QDs can be used in the context of Förster theory (Section 3.2) to calculate predicted energy transfer rates for these materials, and, using time-resolved fluorescence techniques, these predictions can be compared to experimental observables.

3.5.3 Calculation of the Expected Energy Transfer Rate Using Förster Theory

The Förster energy transfer rate can be calculated using Equations 3.5 and 3.6, with experimental observables specific to our system. The orientation factor κ^2 takes an average value of 2/3 for randomly oriented dipoles, and the refractive index n is the weighted sum of the refractive indices of the inorganic cores and organic shells, equal to 1.8 [54]. The spectral overlap is calculated from the donor emission spectrum, $F_D(\lambda)$, normalized to an integrated area of 1, and the acceptor absorption spectrum, $\sigma_A(\lambda)$, which was converted to the correct units based on the method described by De Geyter and Hens using core and shell diameters [65] (Section 3.6.1 discusses the potential error in this value). From Equation 3.6, the theoretical Förster radii for the donor/short-ligand acceptor and donor/long-ligand acceptor pairs are 5.2 ± 0.2 nm and 5.1 ± 0.1 nm, respectively. These values are expected to be identical given that the two acceptors vary only in their ligand, and they match within experimental error. The expected energy transfer rates based on these Förster radii and the measured donor-acceptor spacings are $10(\pm 8) * 10^6$ s^{-1} and $5(\pm 4) * 10^6$ s^{-1}, respectively. The uncertainty in R_0 results from uncertainty in the quantum yield and overlap integral,

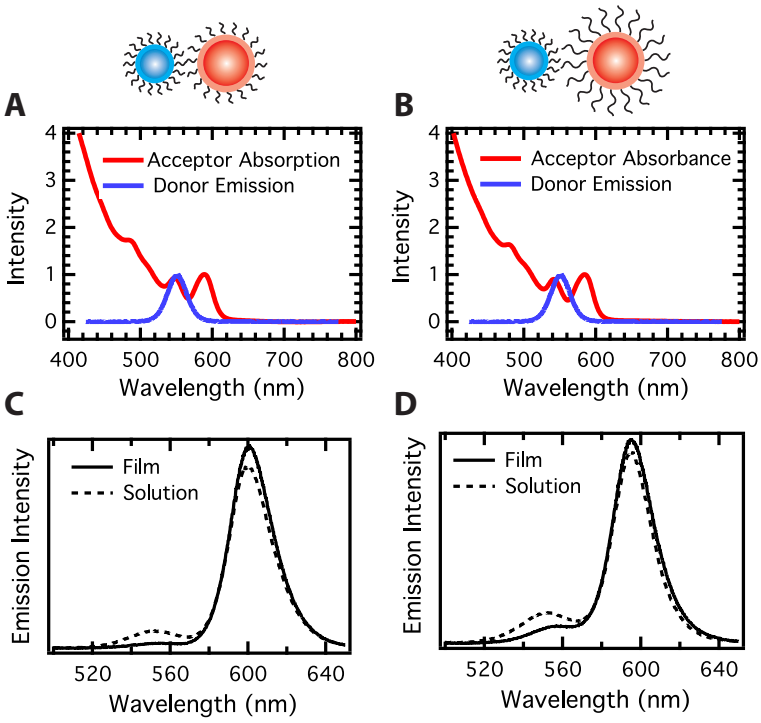

Figure 3-9: (A,B) Emission spectrum of donor (blue) and absorption spectrum of acceptor (red) QDs. The acceptor dots differ only in the length of the surface-bound ligand, which is either short (A) or long (B) as illustrated above each column. (C,D) Emission spectra of the mixed solution (dotted) and film (solid), each normalized to the same number of counts, of nearly equimolar blends of donor and acceptor QDs, showing quenching of donor fluorescence in film compared to solution. The large difference in donor and acceptor emission intensity, despite similar molar concentrations, results from the difference in absorption cross-section between the large acceptor and small donor QDs at the laser excitation wavelength.

while uncertainty in the energy transfer rates stem from uncertainty in R_0, the donor lifetime τ_D and, most significantly, uncertainty in the donor-acceptor distance. Based on these calculations, the energy transfer rate is expected to vary by about a factor of two due to the difference in interparticle separation imparted by the ligands.

3.5.4 Experimental Measurements of the Energy Transfer Rate

The observation donor fluorescence quenching from Figure 3-9 served as the first indicator of energy transfer in these donor-acceptor blended materials, and time-resolved measurements corroborate the energy transfer mechanism. Changes in the

donor lifetime conclusively indicate near-field energy transfer and rule out other possible mechanisms to explain changes in the donor intensity, such as emission-reabsorption. To quantify energy transfer dynamics between donor and acceptor QDs, we measured the exciton lifetime as a function of emission wavelength (Figure 3-10).

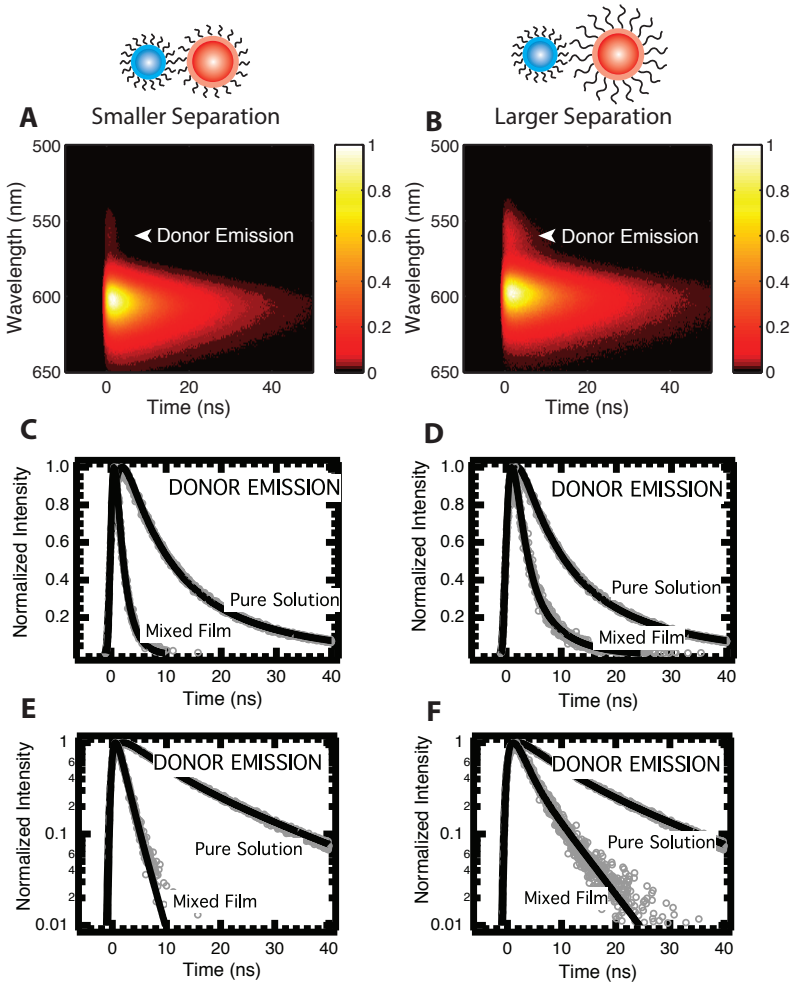

Figure 3-10: Spectrally-resolved transient photoluminescence measurements of donor-acceptor blended films. The left and right columns correspond to the short-ligand and long-ligand acceptor, respectively. (A, B) Normalized fluorescence intensity, indicated by the color bar, plotted as a function of time and emission wavelength. Spectrally-integrated donor counts are plotted on both linear (C, D) and semi-logarithmic (E, F) axes. Solid black lines are fits to the experimental data (open circles).

Plots of emission intensity as a function of emission wavelength and time (Figure

3-10, A-B) show donor quenching and, in particular, reveal more significant donor quenching in the case where the donor and acceptor QDs are closer together (Figure 3-10A). Spectral and temporal resolution allows for clear distinction between donor and acceptor fluorescence. To obtain population decay curves (panels C-F of Figure 3-10), the partially overlapping emission spectra from donor and acceptor QDs were separated by fitting two Gaussians to the emission spectrum recorded at each time slice of the data. The intensities in the donor components of the double Gaussian fit were then spectrally integrated to calculate a donor lifetime in the presence of acceptors. The exciton population decay of the donor in the presence of the acceptor in solid films is plotted in Figure 3-10, panels C-F, and compared to the donor lifetime in solution where no energy transfer occurs. The dramatic change in lifetime results from energy transfer to neighboring acceptors, and the per-pair energy transfer rate may be extracted from the lifetime change as described below in order to compare to theoretical predictions presented in the previous section. The presence of the QD acceptors in solid film reduces donor fluorescence lifetime as well as intensity, indicating near-field energy transfer between donor and acceptor QDs.

The change in donor lifetime observed by spectrally resolved transient photoluminescence (Figure 3-10) was used to calculate the energy transfer rate between donor-acceptor pairs in the blended solid films. In the absence of energy transfer, the total fluorescence decay rate (k_{pure}) is the sum of the intrinsic radiative and non-radiative decay rates,

$$k_{pure} = k_r + k_{nr} \tag{3.8}$$

while in the mixed donor-acceptor film, the total fluorescence decay rate k_{mix} is given by Equation 3.7 (Figure 3-7), where the summation is over all possible FRET acceptors. Therefore, the *total* energy transfer rate may be calculated by subtracting Equation 3.8 from Equation 3.7. Because of the $1/d^6$ distance scaling, only nearest neighbors are expected to contribute substantially to the total energy transfer rate

[55]. Therefore, the per-pair energy transfer rate ($k_{ET,pp}$) can be calculated from

$$k_{ET,pp} = \frac{1}{N}(k_{mix} - k_{pure}) \tag{3.9}$$

where N is the number of nearest neighbors. Danisch *et al.* previously determined the approximate number of nearest neighbors of a given size, given a random close packed lattice of two different size spheres with size ratio 1:1.4, which is the size ratio between donor and acceptor QDs used in this study [66]. For an equimolar mixture of donor and acceptor QDs with this size ratio, N equals 3. Using Equation 3.9, the lifetime comparison yields a direct experimental measurement of the energy transfer rate, which can be used, in turn, to calculate the effective Förster radius.

Correctly applying Equation 3.9 requires a comparison between the donor lifetime in the absence and presence of energy transfer. For this purpose, it is essential to use the solution decay rate for k_{pure} rather than the pure film lifetime because energy transfer within the inhomogenously broadened pure donor ensemble [55] and exciton diffusion to quenching sites [67] obfuscates the true intrinsic decay rate for QDs in a solid film. We can verify that energy transfer occurs within the pure donor film through observation of the decay dynamics at various wavelengths and through the transient redshift that occurs over the course of the exciton lifetime, indicators of excitonic energy transfer described by Figure 3-6. Time-resolved photoluminescence traces of the donor film indeed reveal a transient redshift while the isolated donors in solution display none (Figure 3-11 A-B), and the wavelength-dependent lifetimes demonstrate that in close-packed films the red-edge of the donor QD population has a lifetime similar to isolated QDs while the blue-edge rapidly decays due to energy transfer (Figure 3-11 C-D). The reddest (smallest band gap) QDs in the donor population have effectively no neighbors capable of accepting the band-edge exciton and are therefore effectively isolated. The non-interacting QDs in both solution and film have the same inherent lifetime, so the *solution* lifetime and quantum efficiency (rather than that of the donor film) must be used to predict energy transfer dynamics in blended QD assemblies.

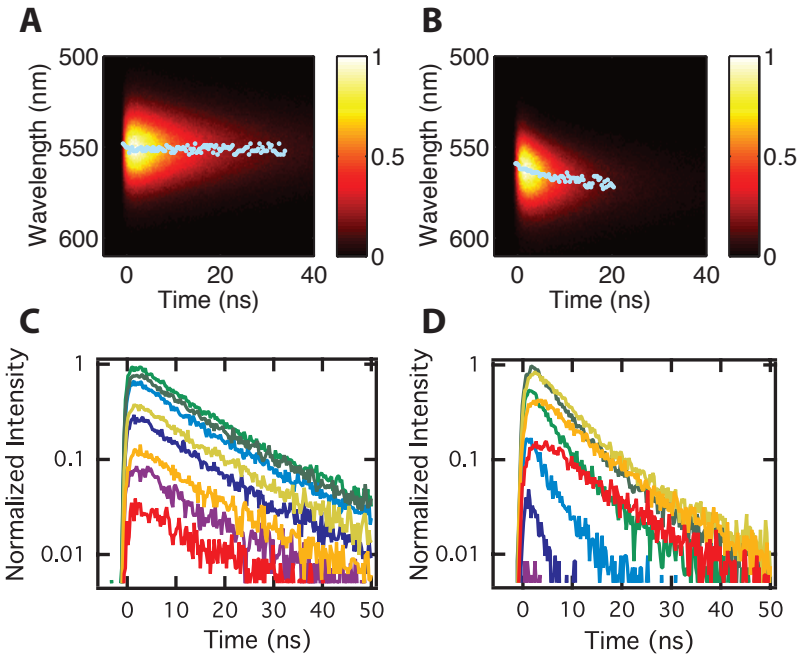

Figure 3-11: Spectrally resolved transient photoluminescence of (A) pure donor solution, and (B) pure donor film. Population decay at selected wavelengths are shown in panels (C) and (D) for the donor solution and film, respectively. Decay traces range in wavelength from 520 nm (purple) to 590 nm (red), in increments of 10 nm.

In the blended QD films, the distribution of donor-acceptor distances (Figure 3-8) is expected to result in a distribution of energy transfer rates, and, accordingly, a distribution of donor fluorescence lifetimes. To obtain a statistically averaged lifetime, we first fit the donor fluorescence decay to a multi-exponential function to deconvolve the time-dependent exciton population $n(t)$ from the instrument response function (determined by the temporal width of the excitation laser pulse). The statistically averaged lifetime, τ_{avg}, is obtained via

$$\tau_{avg} = \frac{\int_0^\infty t * n(t)dt}{\int_0^\infty n(t)dt} \tag{3.10}$$

The lifetime of the donor in solution is 15.5 ± 0.3 ns, yielding k_{pure} for Equation 3.8 equal to 0.065 ± 0.001 ns^{-1}. The average lifetime of the donor blended with the *short ligand* acceptor is $\tau = 1.2 \pm 0.2$ ns ($k_{mix} = 0.8 \pm 0.1$ ns^{-1}) and the average lifetime of

the donor blended with the *long ligand* acceptor is $\tau = 4.1 \pm 0.2$ ns ($k_{mix} = 0.24 \pm 0.01$ ns^{-1}). Using these values and Equation 3.9, we find that the energy transfer rate per donor-acceptor pair is $k_{ET,pp} = 2.6(\pm 0.6) * 10^8$ s^{-1} and $0.6(\pm 0.1) * 10^8$ s^{-1} for the short-ligand and long-ligand acceptors, respectively. These values allow the calculation of an experimental value for R_0 to compare to Förster theory predictions rearranging Equation 3.5 to yield

$$R_0 = d\,(\tau_{pure}\, k_{ET,pp})^{1/6}. \tag{3.11}$$

This equation results in values of R_0 equal to 9 ± 2 and 8 ± 1, for donors paired with the short-ligand and long-ligand acceptors, respectively. These values are summarized in Table 3.1.

Table 3.1: Summary of Theoretical and Experimental Energy Transfer Rates, per Donor-Acceptor Pair

	measured donor–acceptor distance (nm)	R_0 (nm) from theory	$k_{ET,pp}$ (s^{-1}) from theory	$k_{ET,pp}$ (s^{-1}) from experiment	R_0 (nm) from experiment
short ligand	7.0 (±0.9)	5.2 (±0.2)	10 (±8) × 10^6	260 (±60) × 10^6	9 (±2)
long ligand	7.8 (±1.1)	5.1 (±0.2)	5 (±4) × 10^6	60 (±10) × 10^6	8 (±1)

3.6 Reconciling Experiment and Theory

The theoretical Förster radii and energy transfer rates calculated from materials properties are substantially smaller than those measured experimentally. In fact, the expected per-pair energy transfer rates based on the overlap integral and inter-particle separation are more than an order of magnitude smaller than the experimentally measured energy transfer rates based on Equation 3.9 (Table 3.1). Energy transfer rates to next-nearest neighbors are of order 10^4, two orders of magnitude smaller than the rate constants in question, and cannot explain this difference. The discrepancy between theoretical predictions and experimental measurements in our model donor-acceptor system suggests that application of Förster's equation to solid state QD systems requires further consideration, addressed below.

3.6.1 Sources of Experimental Uncertainty

Obvious experimental uncertainty cannot account for the magnitude of the difference between experimentally measured and theoretically predicted energy transfer rates and Förster radii. There is some systematic measurement of the donor-acceptor separation distance due to an inability of the image processing algorithm to distinguish QDs that are very close together in the TEM micrograph. This results in an *over*-estimation of the inter-particle separation on the order of a few tenths of nanometers, but this error is small compared to the propagated uncertainty of ~ 1.0 nm for all calculations. Moreover, the excellent agreement between TEM and GISAXS data suggests that the propagated experimental uncertainty captures any error in the interparticle distance.

Experimental determination of k_{ET} and R_0 depends on knowledge of the number of nearest neighbors, as specified in Equation 3.9. However, even if there are twice as many nearest neighbors as we expect ($N = 6$ rather than $N = 3$), the experimentally measured energy transfer rate remains $\sim 5-15$ times larger than the predicted value. Further, because our QD films are only ~ 3 layers thick and surface QDs are under-coordinated, we have probably *underestimated* the per-pair energy transfer rate by choosing a bulk value for N. Additionally, the TEM images shown in Figure 3-8 indicate that the QDs are not entirely randomly distributed in the film. If slight aggregation of similar types of QDs occurs within our 3D films, this would also decrease the true value of N to less than 3, and would further enhance the discrepancy between calculations and experiment.

These factors, as well as errors in the measurement of quantum yield, lifetime, and other experimental factors, have been quantitatively accounted for in the propagated uncertainty and are insufficient to explain the differences between expected and measured energy transfer rates. We believe that other factors play a role beyond those usually considered in the calculation of the Förster radius; some of these factors are considered below.

3.6.2 Dipole Orientation

As seen in the TEM images of Figure 3-8, the QDs used in this study are not perfectly spherical but instead have a somewhat tetrahedral geometry, as discussed in a previous study using the same materials [61]. This may lead to some oriented packing and alignment of the QDs in thin film, resulting in a transition dipole moment that is not random but instead aligned. Furthermore, the observed 2D character of the emission transition dipole in CdSe QDs makes better-than-random alignment between donor emission and acceptor absorption transition dipoles even more plausible [68]. Murray, *et al.* found that QDs within superlattices tend to align their crystal axes [69], suggesting ready alignment of transition dipoles in some QD assemblies.

3.6.3 QD Shape

In addition to the QD shape affecting packing and transition dipole alignment, it is also possible that shape affects Coulombic and dipole-dipole coupling between neighboring nanocrystals [70]. Several reports in the literature have demonstrated different energy transfer behavior in systems of QDs compared to quantum rods or dot-in-rod structures [70, 71]. Based on published reports of the magnitude of this affect, we estimate that shape could only account for up to 10-20% of the discrepancy.

3.6.4 Higher Order Multipoles

In addition to these physical factors that may be incorrectly accounted for in the usual calculations of R_0 and k_{ET}, the discrepancy may be fundamentally due to the assumption that QD-QD energy transfer in thin film is mediated by point dipole-point dipole coupling. Baer and Rabani showed that for small surface-to-surface separations, dipole-quadrupole coupling may contribute non-negligibly to the total energy transfer rate [52]. In particular, for surface-to-surface distances less than about 20% of the total center-to-center distance, dipole-quadrupole coupling may contribute more than a third to the combined energy transfer rate. For this model system, the expected difference in energy transfer rates from donor to acceptor for the two test

cases was a factor of 2, as described above; however, a factor of 4 difference was observed experimentally. The relative change in energy transfer rate from the donor to the short-ligand acceptor vs. long-ligand acceptor may be due in part to dipole-multipole interactions as the surface-to-surface separation is 25% of the total center-to-center separation in the case of the short-ligand acceptor (putting it into the realm of more significant dipole-quadrupole coupling), but more than 40% of the center-to-center distance in the case of the long ligand acceptor. As a result, the larger than expected difference between the measured energy transfer rates with the two acceptors could be due in part to dipole-quadrupole coupling, which contributes to the energy transfer rate in the case of the shorter-ligand acceptor but has a negligible effect for the longer-ligand acceptor. Contributions from dipole-quadrupole coupling may account for part of the magnitude difference between the measured and theoretical energy transfer rates, but the exact contribution is difficult to quantify.

3.6.5 Absorption Cross Section

The absorption cross-section of the acceptor QDs sensitively affects the calculated overlap integral, and therefore the Förster radius, for a donor-acceptor pair. However, there are inconsistencies in the literature as to the magnitude of the absorption cross section as a function of QD size. In this work, the calculated Förster radius changes between 4.8-6.2 nm depending on the value of the absorption cross-section used. CdZnS shells surround the nanoparticles examined in this study, which complicates the determination of absorption cross section. As a result, the work of De Geyter, *et al*, which directly addresses this issue, was used for calculating absorption cross-section [65]. However, other methods for calculating the absorption cross-section [16, 62, 72] can yield slightly different values that may change the absorption cross-section, and therefore the Förster radius. The lack of experimental consensus renders exact calculation of the absorption cross section difficult, and highlights the need for improved data in this important area of QD research.

3.6.6 Thin Film Polarizability Effects

In addition to variation in the calculated absorption cross-section depending on method, a further likely contribution to the larger than expected energy transfer rate is an enhanced absorption cross-section of the acceptor QDs in film compared to solution. Recently, Geiregat et al. showed that the absorption cross-section per QD in close-packed films is enhanced relative to the solution value due to dipole-induced-dipole effects in the solid [50]. For CdSe QDs of the sizes used here, the absorption cross section in thin film was measured to be 3-4 times larger than the absorption cross section in solution [50]. If the measured absorption spectrum is scaled to this new, larger magnitude value (and possible dipole orientation effects ignored), the theoretical value for R_0 increases from 5.1-5.2 nm to 6.2 nm for both donor-acceptor pairs. Furthermore, these polarization effects should play a larger role in short-ligand QD assemblies due to closer proximity of neighboring QDs [50]. We indeed observe a larger deviation from the predicted theoretical energy transfer rate in the system with the shorter ligand acceptor than that with the longer ligand acceptor, consistent with stronger absorption enhancement in the denser QD array. These factors suggest that the results of a full ligand series to incrementally change the inter-particle separation may be difficult to interpret. Even if Förster theory is the correct theoretical framework, such a study would likely not result in the expected $1/d^6$ scaling because the polarizability (acceptor absorptivity) of the nanocrystal assembly, its refractive index, and the inter-particle separation all change simultaneously in different directions.

3.7 Conclusions

This Chapter discusses the measured the energy transfer rate between donor and acceptor QDs in homogeneously blended films, where the inter-particle separation was tuned through altering the ligand length of the acceptor. The measured energy transfer rates were found to be more than an order of magnitude larger than the theoretical energy transfer rates calculated based on Förster theory, using

standard assumptions. Several possible sources of the discrepancy were identified and quantified, including QD shape, preferential orientation of transition dipoles, enhanced absorption cross-section, and dipole-multipole coupling; these factors may result in different behavior for QDs in solid films than for QDs in solution. To further elucidate the mechanisms underlying energy transfer in CdSe QD assemblies, further experimentation may focus on the direct comparison of energy transfer between isolated donor-acceptor pairs in solution to that in solid film. This work suggests that predicting energy transfer between QDs at small distances within a close-packed film requires careful consideration, and informs our understanding of excitonic energy transfer in QD films relevant for optoelectronic devices such as solar cells and LEDs.

3.8 Chapter-Specific Acknowledgements

The QD materials used for this work were generously provided by Jonathen Steckel and Seth Coe-Sullivan of QD Vision. Dr. Ferry Prins helped with experimental design, and Mark Weidman performed TEM and GISAXS measurements.

Chapter 4

Raman Spectroscopy of Acoustic Phonons in Nanocrystals

Much of Chapter 4 has been submitted for publication as Mork, Lee, Dahod, Willard, and Tisdale (2016).

4.1 Introduction

Advancements in the synthesis of colloidal semiconductor nanocrystals, also known as quantum dots (QDs), have led to improvements in their monodispersity, quantum yield, and photostability, paving the way for their incorporation into a variety of optoelectronic devices [1, 5, 6, 73]. While considerable progress has been made in the control of QD electronic properties [74–76], the intentional engineering of vibrational and thermal properties has not been demonstrated. In particular, the low-frequency ($<$50 cm^{-1}, or $<$1.5 THz) acoustic vibrations of QDs affect a wide range of optical, electronic, and thermal properties of QD materials, but there have been virtually no studies documenting how structural or environmental attributes of QDs affect their vibrational spectra, with the exception of QD size.

The thermal properties of nanocrystal assemblies are complicated by their heterogeneous structure, including a myriad of interfaces between organic and inorganic components. The effects of these interfaces on the excitonic and charge transport properties of QD films have been well documented [1], but their impact on

vibrational (heat) energy transfer requires further understanding. For semiconductors such as QDs, heat is primarily carried by the acoustic and optical phonons discussed in Chapter 1.3. Nanoparticle assemblies exhibit low thermal conductivities, which limit their use in many devices because high operating temperatures affect both the quantum yield and recombination rates of QDs, often deteriorating device performance characteristics after long on-times [77]. Their thermal conductivity is only weakly dependent on the composition of the core, suggesting an essential role played by the interfaces in these hybrid materials, as discussed in Chapter 1.3.2.

In addition to their importance for thermal energy transport in QD materials, acoustic phonons influence fundamental photoluminescence properties of nanocrystals. The coupling between excitons and acoustic phonons results in a fluorescence lineshape that deviates from the ideal Lorentzian profile for single QDs due to acoustic phonon sidebands [78,79]. Both optical and acoustic phonons are believed to affect the QD homogeneous photoluminescence linewidth; the former through exciton-phonon coupling via the Frölich mechanism [21] and the latter through contributions to the exciton dephasing time [80, 81]. Finally, acoustic phonons are known to mediate transitions between dark and bright exciton states in the low-temperature optical emission of QDs, and affect the low-temperature photoluminescence lifetime [82, 83]. Therefore, improved understanding of QD acoustic phonon modes may shed light on fundamental photophysical processes, such as intra-level transitions, spin-flips, and exciton dephasing, in addition to heat transfer characteristics.

The acoustic phonon energies of nanoparticles are known to depend on the size of the nanocrystal, but the effects of the ligands and inorganic shell materials integral to the composition of colloidal QD materials have, to the best of our knowledge, never been studied. Elastic continuum modeling of nanoparticles as spherical mechanical resonators, where the stress-strain response of a mass-containing differential element is described by Hooke's law [84], has successfully predicted the inverse size dependence of the acoustic phonon energies of many types of nanoparticles [85–89], especially those embedded in glass [90–93]. However, few studies have measured the acoustic phonon spectrum of the colloidal nanoparticles used for solution-processable QD

device applications either directly (e.g. by Raman spectroscopy [88]) or indirectly (e.g. by pump-probe spectroscopy [85, 94]). In particular, the effect of surface chemistry remains largely unexplored, though disagreements between theoretical predictions and experimentally observed phonon energies have been postulated to result from the presence of ligands [85, 88].

This Chapter will describe the use of low-frequency Raman spectroscopy to measure the energies of acoustic vibrations of CdSe nanocrystals, and their dependence on QD size, ligand, and inorganic shell thickness. These results demonstrate that several synthetic handles can finely tune nanocrystal vibrational energies.

4.2 Mathematical Models of Phonons in Nanocrystals

Quantum confinement alters the electronic properties of nanocrystals, resulting in energy level shifts as a function of size (Chapter 1.2), among other effects. From Chapter 1.3, optical and acoustic phonons describe the normal vibrational modes of a crystal with a two-atom basis, with the former describing the relative motion of atoms within a unit cell and the latter referring to long-wavelength in-phase vibrations of many unit cells. Similar to charges (electrons/holes) in QDs, phonons can also experience confinement effects, especially as their wavelength or mean free path may exceed the nanocrystal diameter. Two major models describe alterations to phonon properties in nanocrystals: the phonon confinement model, primarily used for optical phonons, and the elastic sphere model, primarily for acoustic phonons.

4.2.1 Phonon Confinement Model

The phonon confinement model seeks to mathematically describe the observed Raman spectra of optical phonons in nanostructured materials through incorporating contributions from non-zone-center ($\mathbf{k} \neq 0$) phonons, contrary to the momentum conservation rules from Chapter 2.14. In the phonon confinement model, the optical vibrations of the nanocrystal can be described by the plane wave bulk phonon

multiplied by a Gaussian envelope function that decays near the edges of the nanocrystal because phonons cannot propagate beyond the boundary [37, 95]. In this model, the phonon wavefunction, Φ, for a particle of diameter d is a function of the phonon wavevector $\mathbf{k}$ and the radial position within the nanocrystal r:

$$\Phi(\mathbf{k}, r) = u(\mathbf{k}, r)\, e^{i\mathbf{k}r} * e^{-\alpha(r/d)^2}. \tag{4.1}$$

This equation features the Bloch wave $u(\mathbf{k}, r)\, e^{i\mathbf{k}r}$ for the unperturbed optical phonon and the Gaussian envelope function $e^{-\alpha(r/d)^2}$ featuring decay constant α that varies depending on the model. A series of mathematical manipulations yields a phonon wavefunction composed of a superposition of plane wave phonons of wavevector $\mathbf{k}$ centered around $\mathbf{k} = \mathbf{k_0}$ and weighted by a coefficient $C(\mathbf{k_0}, \mathbf{k})$ [37]:

$$C(\mathbf{k_0}, \mathbf{k}) = \frac{1}{(2\pi)^3} \int e^{i(\mathbf{k_0}-\mathbf{k})r} * e^{-\alpha(r/d)^2} d^3r \tag{4.2}$$

Because each wave is expected to give rise to a Lorentzian line shape (with width Γ) in the Raman spectrum, the total Raman intensity is given by

$$I(\omega, d) \propto \int \frac{|C(\mathbf{k_0}, \mathbf{k})|^2}{(\omega - \omega(\mathbf{k}))^2 + (\Gamma/2)^2} d^3\mathbf{k} \tag{4.3}$$

where the integral runs over all the $\mathbf{k}$ in the Brillouin zone. The factor $\omega(\mathbf{k})$ in the denominator is the phonon dispersion relation, which, for optical phonons, can be written $\omega(\mathbf{k}) = \omega(0) - \Delta\omega * \sin^2(ka/4)$ for lattice constant a and $\Delta\omega$ equal to the difference in frequency between the zone-center and zone-edge optical phonons [96]. The phonon confinement model has been used extensively to understand the observed broadening and red-shift associated with nanoparticle optical phonon Raman features (Figure 4-1).

It is worth noting that, in the Phonon Confinement Model, smaller nanoparticles result in a *red shift* in the phonon energy and an asymmetric broadening of the phonon peak. Both of these effects result from contributions from phonons with $\mathbf{k} \neq 0$. As can be seen in the optical phonon branch of the schematic dispersion curve from

Figure 1-9, optical phonons with $\mathbf{k} \neq 0$ are lower in energy than those near $\mathbf{k} = 0$, so increasing participation of far-from-center optical phonons results in an asymmetric broadening towards lower energy of this peak. In the next section, it will be shown that for acoustic phonons, the Elastic Sphere Model predicts that smaller particles have *blue shifted* acoustic phonon energies.

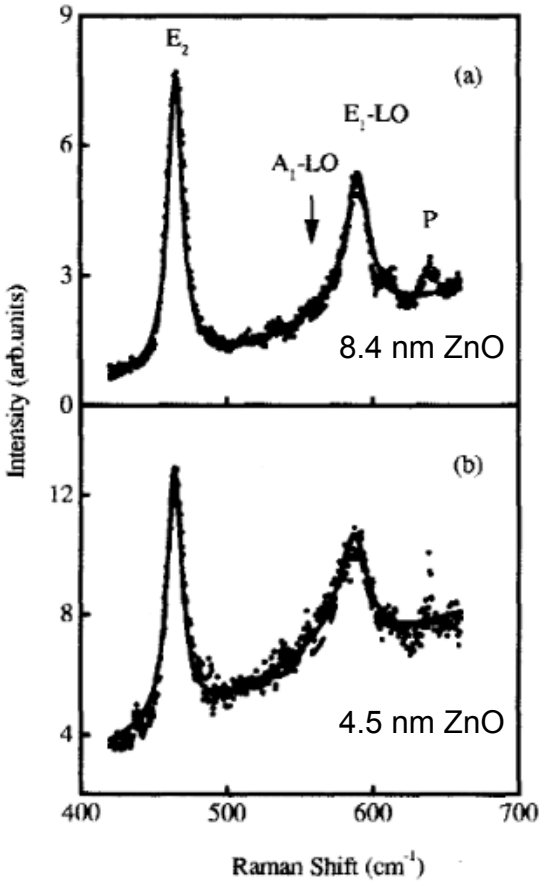

Figure 4-1: Raman spectra of ZnO particles of two different sizes. The smaller particles (bottom panel) exhibit broader and slightly redshifted phonon features due to increased optical phonon confinement. Reproduced with permission from [95], ©2000 American Institute of Physics.

4.2.2 Elastic Sphere Model

The lowest energy acoustic phonons of nanoparticles describe the in-phase vibration of the entire nanocrystal lattice. The mechanical resonance frequencies of these modes

are quantized, with discrete energies that vary with the size of the particle. The vibrations of spherical particles have been studied mathematically since 1882, when Lamb first described the vibrational eigenmodes of a homogeneous elastic sphere [84]. He showed that these vibrational modes can be either spheroidal (volume-changing) or torsional (surface), and can be described with the labels n, ℓ, and m. These quantum numbers are exactly analogous to solutions for electronic wavefunctions for atoms, where n is the principle quantum number indicating the number of radial nodes, while ℓ is the angular quantum number describing the number of wavelengths that fit along the surface of the nanoparticle and m is the projection of the angular momentum along the z axis. The labels ℓ and m are the labels for the spherical harmonic functions Y_ℓ^m (Figure 4-2).

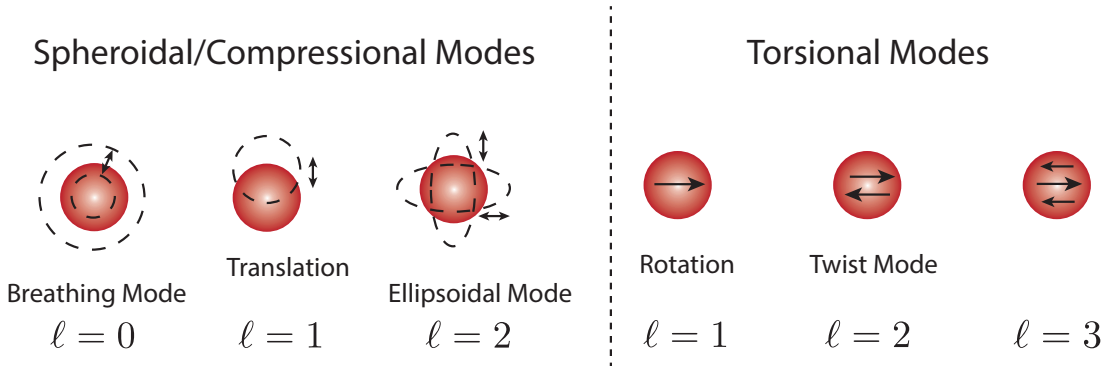

Figure 4-2: Schematic drawings of the normal vibrational modes of an elastic sphere, including spheroidal (left) and torsional (right) for indicated values of ℓ and $m = 0$.

There are a variety of methods to measure acoustic phonon frequencies for nanocrystals, but for spherical particles the only Raman active modes are the symmetric $\ell = 0$ and ellipsoidal $\ell = 2$ modes [97]. These modes have been observed and assigned for several types of inorganic nanomaterials embedded in glasses, including CdSe [92], PbSe [90], and Si [86]. For the $\ell = 0$ mode, also known as the radial breathing mode, the solution to the Navier equation that governs the displacement waves in the spherical particle depends on the boundary condition. Typically, the boundary condition is assumed to either be free (also known as homogeneous, with zero stress at the surface) or rigid (zero displacement at the

surface). For the free boundary condition, the vibrational frequency ω is given by the characteristic equation [92]

$$\tan(\alpha) - \frac{\alpha}{1 - \frac{v_l^2}{4v_t^2}\alpha^2} = 0 \tag{4.4}$$

for

$$\alpha = \frac{\omega R}{v_l}.$$

In these equations, v_l and v_t are the longitudinal and transverse sound velocities of the material, respectively. In this case, if the frequency ω is plotted as a function of $1/R$ the slope is equal to $\alpha * v_l$ for the characteristic roots α that satisfy Equation 4.4 (the first root of Equation 4.4 corresponds to $n = 1$, and larger roots correspond to larger values of the quantum number n). In other words, a plot of ω vs. $1/R$ should yield a line that depends on the sound velocities of the sphere. For the rigid boundary condition, the characteristic equation is given by [92]

$$\tan(\alpha) - \alpha = 0. \tag{4.5}$$

This equation also suggests a linear relationship between ω and $1/R$ but the values of α that satisfy Equation 4.5 are different from those that satisfy Equation 4.4. The predicted dependence of the phonon frequency with nanocrystal size using CdSe parameters is shown in Figure 4-3. Both the rigid and free boundary condition models assume nothing about the nature of the surface or the medium surrounding the sphere, and in fact there is little consensus on the best boundary condition to use to describe the vibrational eigenmodes of QDs. Therefore, goals of this chapter include the elucidation of reasonable boundary conditions for the elastic sphere model that yield accurate predictions for QDs, and the extension of the elastic sphere model to the case of core-shell QDs.

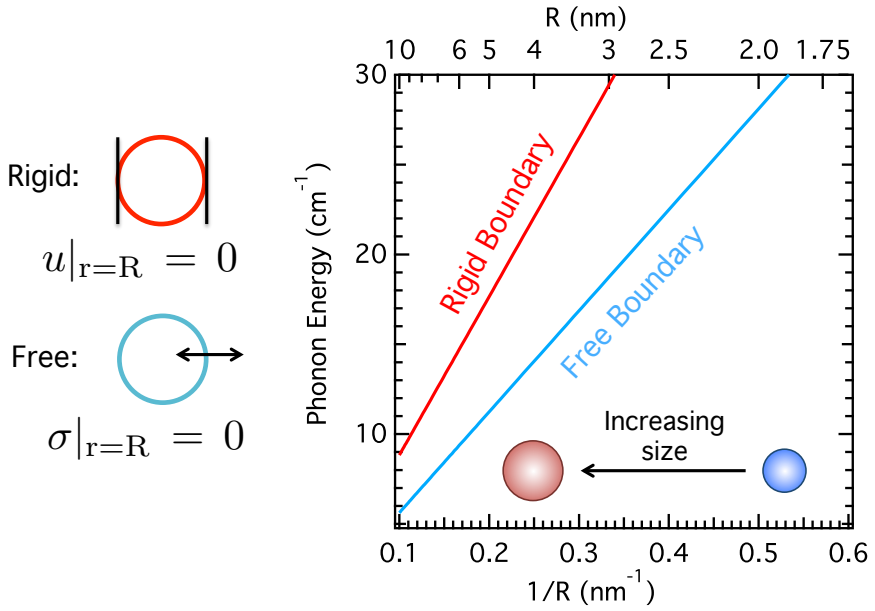

Figure 4-3: Left: Illustrations of rigid and free boundary conditions with mathematical interpretation, u = displacement, σ = stress. Right: Predicted $\ell = 0$ phonon energy dependence on $1/R$ for rigid boundary and free boundary condition models.

4.3 Methods

4.3.1 General Procedures

In this Chapter, QDs were synthesized with either octadecylphosphonic acid native ligands through a standard hot-injection method (see Appendix A) [98] where aliquots were taken over time to collect different sizes, or oleic acid native ligands though a seeded growth method with slow injection of growth precursors [99]. Zincblende QDs were synthesized according to [100]. Ligand exchange reactions, when relevant, were performed on octadecylphosphonic acid native ligand QDs, and conducted as described below. After repeated purification through precipitation and resuspension, QDs were drop cast onto clean glass coverslips, and their Raman spectra were collected using the setup described in Chapter 2-7.

4.3.2 Ligand Exchange Methods

QDs were ligand exchanged with variable length alkanethiols (hexanethiol, octanethiol, decanethiol, dodecanethiol, tetradecanethiol, octadecanethiol) or substituted benzylmercaptans purchased from Aldrich and used as received. For the ligand exchange reaction, 20-50 nmol of freshly purified CdSe QDs were dissolved in 1 mL of chloroform. To this solution were added 1 mmol of the desired ligand and 0.1 mmol of triethylamine to serve as a non-interacting base to help generate the thiolate [101]. Ligand exchange solutions were stirred overnight (>12hrs) and the QDs were subsequently crashed out with a combination of methanol and butanol for alkanethiol ligand exchange reactions. QDs substituted with benzylmercaptans with the *para*-substituent X = H, F, Cl, Br, CF_3 were crashed out for purification by adding hexanes, and were resuspended in acetone. QDs substituted with benzylmercaptans with X = Me, tBu were crashed by adding methanol and butanol and were resuspended in hexanes.

To confirm the success of ligand exchange, we measured the ^{31}P and ^{1}H NMR spectra for dodecanethiol-exchanged QDs and compared them to the spectra acquired for control (non-ligand exchanged) QDs from the same batch synthesis. Both were purified by crashing out 4 times, then dried under vacuum before NMR analysis. The ligand-exchanged QDs and the control QDs were diluted to the same concentration into chloroform-*d*, and the ^{1}H and ^{31}P acquisition parameters were constant for all spectra. As can be seen in Figure 4-4, the phosphorus ligand bound to the surface of the control QDs largely disappears in the ligand exchanged QDs. Based on absolute intensity integration of these peaks, the ligand exchange was effective at removing ∼99% of the native ligands from the sample surface.

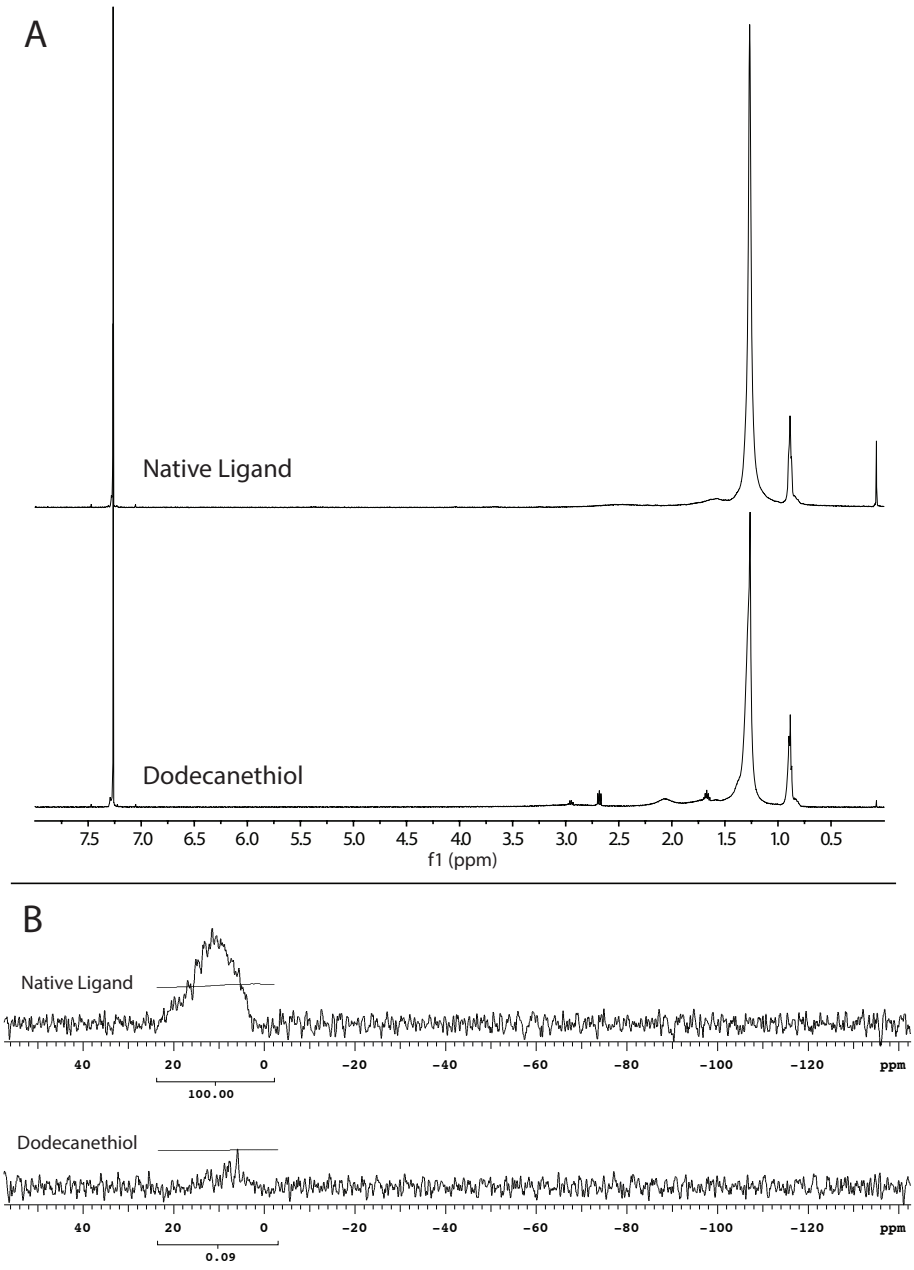

Figure 4-4: (A) ^{1}H NMR spectra of QDs with native phosphonic acid ligands (top) and after ligand exchange with dodecanethiol (bottom). Proton NMR spectra do not allow sufficient differentiation between alkanethiol and native ligand peaks to permit quantification of ligand exchange. (B)^{31}P NMR spectra of QDs with native ligands (top) and QDs after ligand exchange(bottom). The cores with native ligands show a characteristic broad phosphoric acid peak between 0-20 ppm [101], and this peak has largely disappeared in the ligand exchanged sample. The phosphorous peaks have been integrated on the same absolute integral scale, and comparison shows that the ligand exchange procedure was 99% effective in removing the native ligands from the QD surface. The concentration of QDs (determined by UV-Vis spectroscopy) and the acquisition parameters were the same for both samples.

To verify that observed changes in the QD Raman spectra were not due to changes in QD size, absorption spectra for all QD samples before and after ligand exchange were collected and compared. As seen in Figure 4-5, the absorption onset remains constant after ligand exchange. Quenching of the second absorption feature is seen, which has been suggested to indicate a mixture of ligands at the surface [99].

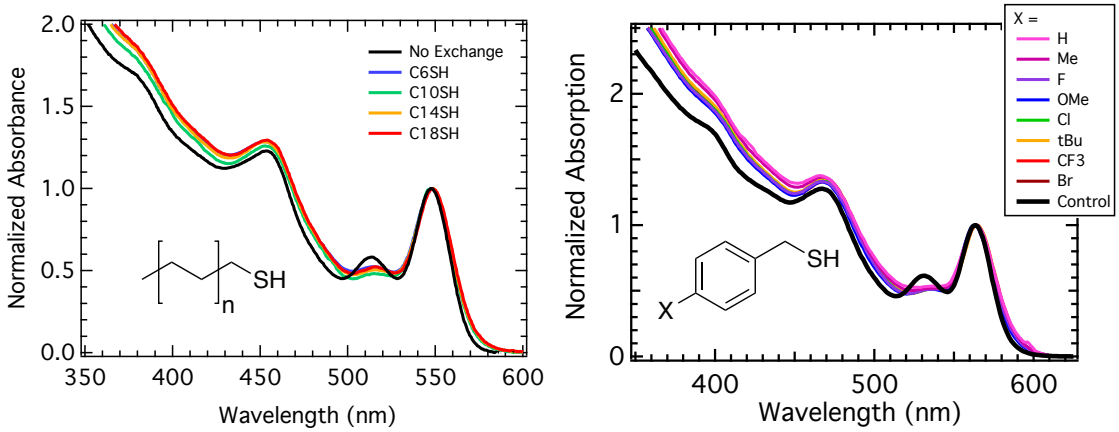

Figure 4-5: QDs after ligand exchange with alkanethiols (left) and benzylmercaptans (right) of different sizes show no change in the absorption onset, which indicates the QD size remains constant upon ligand exchange, and the ligand exchange does not affect the QD Raman spectrum through changing QD size.

4.3.3 Fitting Phonon Energies in Low-Frequency Raman Spectrum

The energy of the $\ell = 0$ phonon was determined through spectral fitting. The Stokes side of the Raman spectrum was fit with three Gaussian functions, one to capture the $\ell = 2$ phonon, one for the $\ell = 0$ phonon, and one broad background peak. The transmission function of the VHG notch filter incorporated into the fitting by multiplying it by the sum of the three Gaussians. An example set of data with fits is shown in Figure 4-6 for 4.3 nm QDs. At least four spectra from different regions of the sample were acquired for each measurement, and each spectrum was fitted separately. The measured energy of the $\ell = 0$ phonon was the average center of the fitted Gaussians, and the error was the standard deviation of the fitted Gaussian centers. Typically, the error for each sample was on the order of 0.05-0.1 cm^{-1}, which

is smaller than $\sim$0.4 cm^{-1} energy spacing between pixels of the spectrograph. We note that this procedure is used to accurately measure the position of the $\ell = 0$ phonon peak and can extract its approximate linewidth (green Gaussians in Figure 4-6), but does not attempt to describe all aspects of the lineshape.

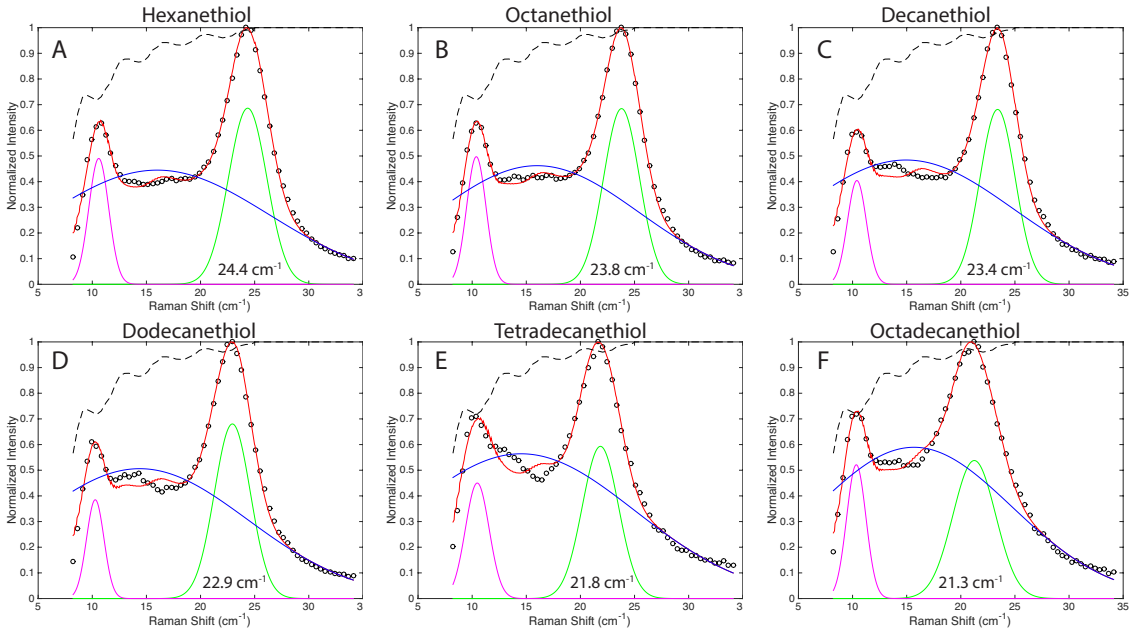

Figure 4-6: Fitted Raman spectra of a series of alkanethiol ligand exchanged QDs 4.3 nm in diameter, with the alkanethiol specified above each panel. The black circles are the experimental data, the pink, green, and blue lines correspond to the three Gaussian fits, the red line is the sum of the three Gaussians, and the black dashed line is the transmission function of the notch filter. The fitted peak position is indicated under the green ($\ell = 0$) trace for each spectrum.

4.3.4 Fitting using Elastic Continuum Theory Models

The measured Raman spectra were used to understand QD phonon energies in the context of an elastic continuum model that incorporates the effect of ligand and/or shell materials, which is an extension of the basic model described in Section 4.2.2. For the core-ligand model, there are a total of 8 variables: ρ_{core}, ρ_{ligand}, $v_{l,core}$, $v_{l,ligand}$, $v_{t,core}$, $v_{tligand}$, R_{core}, and L_{ligand}. The variables ρ indicate density, v_l is the longitudinal sound velocity, v_t is the transverse sound velocity, R is the QD radius, and L is the

ligand length. When fitting the data relating QD size to phonon energy, the sound velocities of the ligand shell, $v_{l,ligand}$ and $v_{t,ligand}$, are the only free fitting parameters that are found via a least-squares fitting minimization. The sum of the squared residuals was found to be insensitive to $v_{t,ligand}$ for all ligand series data sets, likely because the transverse sound velocity of the ligand plays no role in the breathing mode which has no shear character. Therefore, we report no $v_{t,ligand}$. For more details regarding the model used, see the upcoming paper by Mork, Lee, Dahod, Willard, and Tisdale.

4.4 Size Dependence of Acoustic Phonon Frequencies

To understand the size dependence and the appropriate surface boundary condition to model acoustic vibrations for colloidal QDs in thin films, we synthesized a size series of QDs with native octadecylphosphonic and oleic acid ligands. As seen for the octadecylphosphonic acid capped QDs in Figure 4-7, the Raman spectra show a continuous redshift in both the $\ell = 0$ and $\ell = 2$ modes with QD size (approximate sizes given in the corresponding absorption spectra), consistent with the Elastic Sphere model. Similarly, the Raman linewidth varies inversely with size (Figure 4-7c), as has been observed previously [93, 102] and indicates damping of the acoustic phonon mode with the medium. However, when the measured energies of the $\ell = 0$ breathing mode are compared to the continuum elastic predictions based on Equations 4.4 and 4.5 (Figure 4-3), the models are found to predict higher vibrational energies for all QD sizes than are observed experimentally (Figure 4-8). Furthermore, the deviations between the model predictions and the experimental measurements are more significant for smaller QDs, which cannot be accounted for by the behavior of purely elastic spheres.

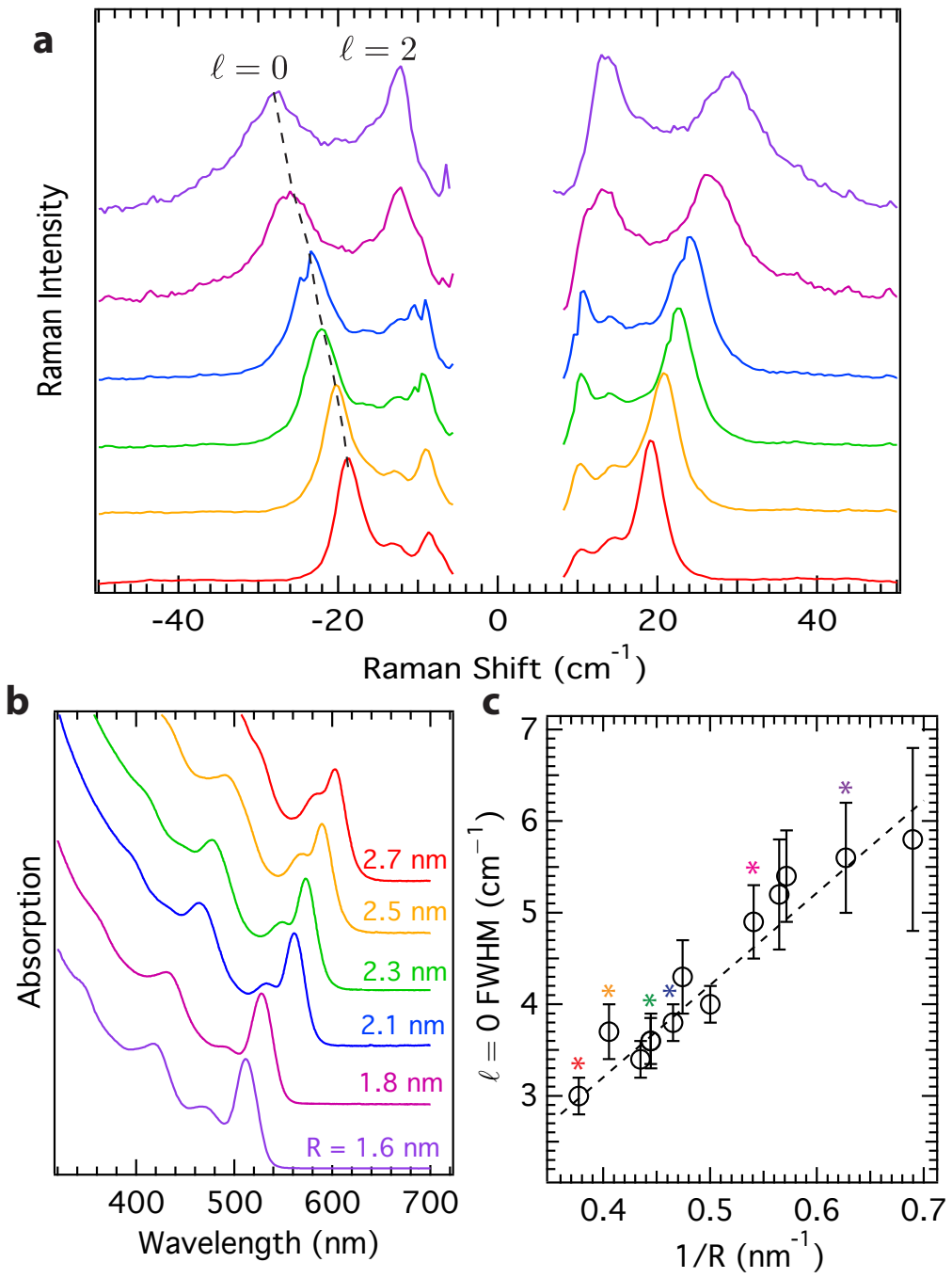

Figure 4-7: a) Raman spectra for CdSe core QDs with octadecylphosphonic acid ligands. b) Absorption spectra for QDs with colors corresponding to Raman spectra in (a) and sizes indicated. c) Fitted FWHM of $\ell = 0$ peak for QD cores. Colored asterisks correspond to line colors in (a). Dotted line serves as guide to the eye.

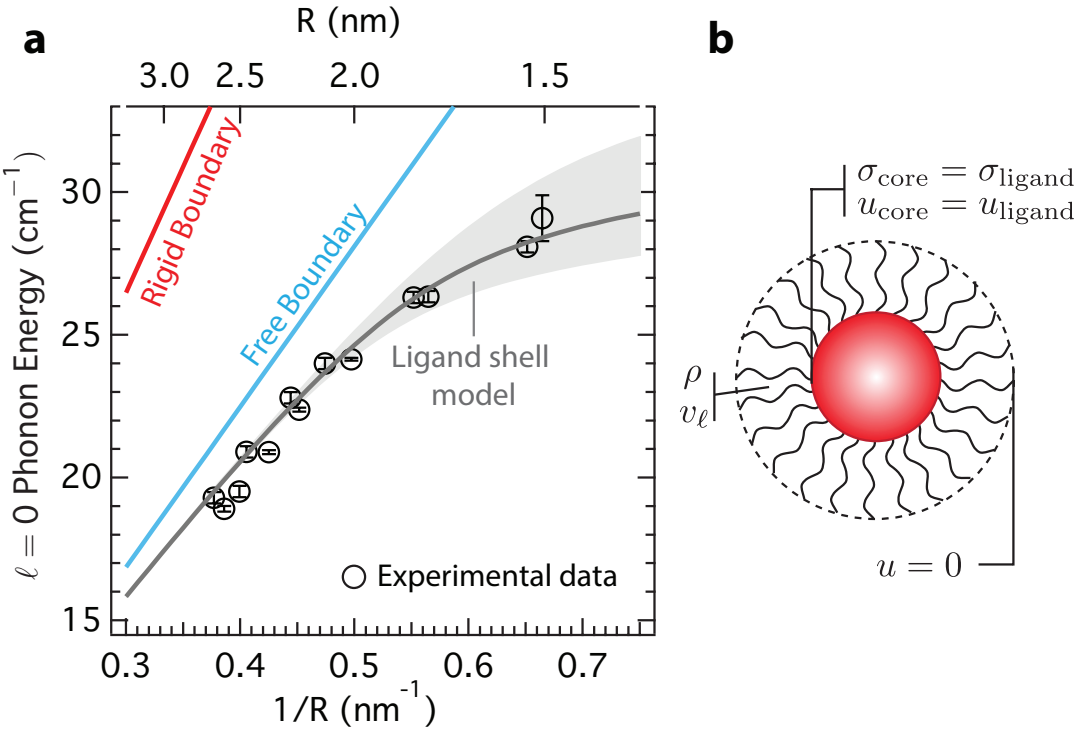

Figure 4-8: (a)Comparison of experimentally measured phonon energies (circles) and elastic sphere model predictions (lines) for radial breathing mode ($\ell = 0$) of QD nanocrystals. Grey line is fit to data using the core-ligand model described in the text, and the shaded region represents the uncertainty in the fit based on the uncertainty in QD size (see Appendix A for sizing information). Error bars represent standard deviation among at least four measurements. 10 cm-1 = 0.3 THz. (b) Schematic of the core-ligand model used to fit the data in (a), in which the elastic sphere model is extended to include vibrational properties of a bound ligand shell. The symbols v_l and ρ are the longitudinal sound velocity and the density of the ligand shell, respectively, σ is the stress at the core-ligand interface, and u is the displacement.

To explain the observed differences between experimental data and the predictions based on continuum models of QDs as homogeneous elastic spheres, we developed an extension of the traditional elastic sphere model to explicitly incorporate the effect of a ligand shell. In the absence of ligands, atomistic molecular dynamics simulations of the quasi-breathing mode energy for metal clusters vibrating in vacuum quantitatively agree with both Lamb's model and pump-probe experiments, even for particles as small as 1 nm in diameter [103]. Therefore, the discrepancies between the elastic sphere model and our experimental results for *colloidal* nanocrystals likely

results from the presence of ligands rather than from a failure of the continuum elastic approximation. This hypothesis is consistent with the observation that the largest deviations from theory occur for the smallest nanoparticles, which have the greatest surface area to volume ratio and for which the ligand mass contributes most significantly to the total mass of the nanostructure [85,88]. To incorporate the elastic response of the ligands, we extend the previous homogeneous elastic sphere model to the case of a spherical acoustic resonator cavity perturbed by mechanical surface interactions caused by mass loading. In this core-ligand model (Figure 4-8b), the QD core vibrates against a deformable organic ligand with a matching boundary condition at the core-ligand interface and a rigid boundary condition at the outer surface of the ligand sphere where the ligand shells of adjacent QDs push against each other [104, 105]. We emphasize that the vibrational modes we experimentally observe and model here are localized on individual nanocrystals, and are different from the coherent superlattice modes that some have observed at significantly lower frequencies (5-50 GHz) using time-domain techniques [106, 107].

To validate the core-ligand model, we have applied it to a series of octadecylphosphonic acid (ODPA) terminated QDs with sizes spanning the available synthetic range. Figure 4-8a shows the experimentally measured phonon energies, as well as the fit to these data using the core-ligand model. In this model, the only free fitting parameter was the longitudinal sound velocity of the ligand shell. The fitted value of 2424 $\pm$ 70 m/s for the ODPA sound velocity closely resembles that of high-density polyethylene (2430 m/s), a similarly saturated hydrocarbon material [108]. To further probe this effect, a size series of CdSe QDs with oleic acid ligands were also synthesized and fitted using the core-ligand model (Figure 4-9). The oleic acid ligand data yield a ligand sound velocity of 2439 $\pm$ 250 m/s, effectively identical to the octadecylphosphonic acid data, suggesting that 18-carbon ligands similarly affect the breathing modes of QDs. The core-ligand elastic continuum model successfully captures both the measured redshift in phonon energies at all sizes compared to the core-only model, and also explains the observed phonon energy rollover for small QD sizes (large $1/R$). This is the first observation of such a ligand effect on the vibrational

frequencies of QDs.

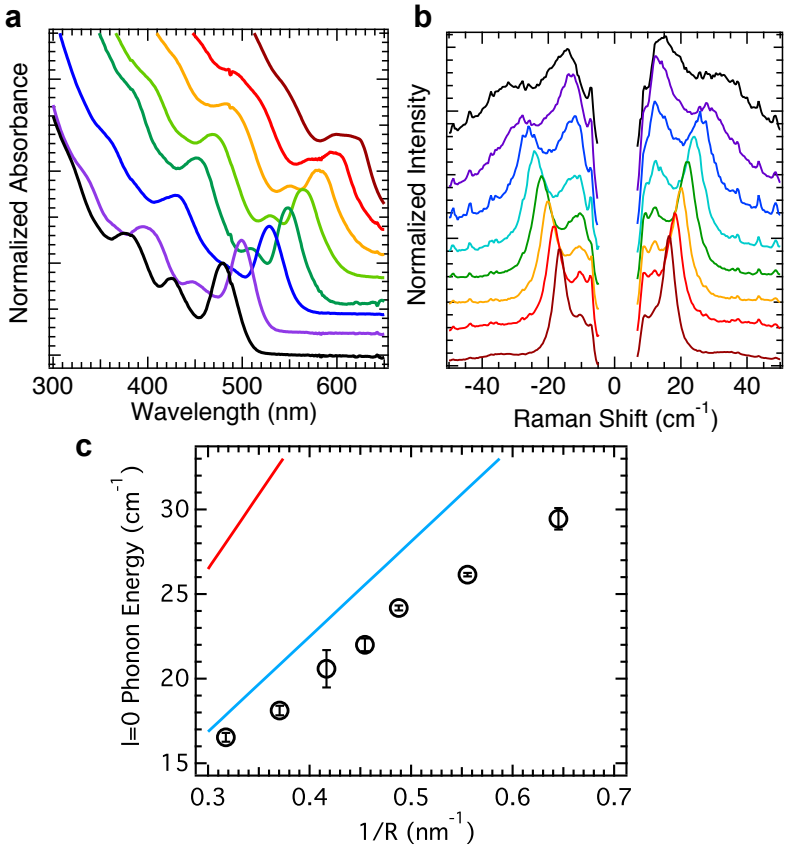

Figure 4-9: (a) Absorption spectra for oleic acid capped QDs grown by seeded growth method (see Appendix A for experimental details). (b) Raman spectra for the particles of (a). (c) ℓ=0 phonon mode energy as a function of $1/R$ for oleic acid capped QDs. Red and blue lines correspond to rigid and free boundary condition predictions, respectively.

Finally, to test the effect of crystal structure, a size series of zincblende nanocrystals were synthesized according to the method of Chen, *et al.* with oleic acid ligands and compared to the wurtzite QDs with the same ligands. Each synthesis (zincblende and wurtzite) was repeated twice, with the results are shown in Figure 4-10, which are compared with the theoretical prediction based on the free boundary condition as a function of $1/R$. For a given size, the zincblende nanocrystal phonon energy is usually slightly larger than for wurtzite nanocrystals, consistent with the theoretical prediction, but the difference is small compared to the x-axis error. These

data demonstrate that zincblende and wurtzite QDs have similar size-dependent phonon energies when synthesized with the same surface ligand.

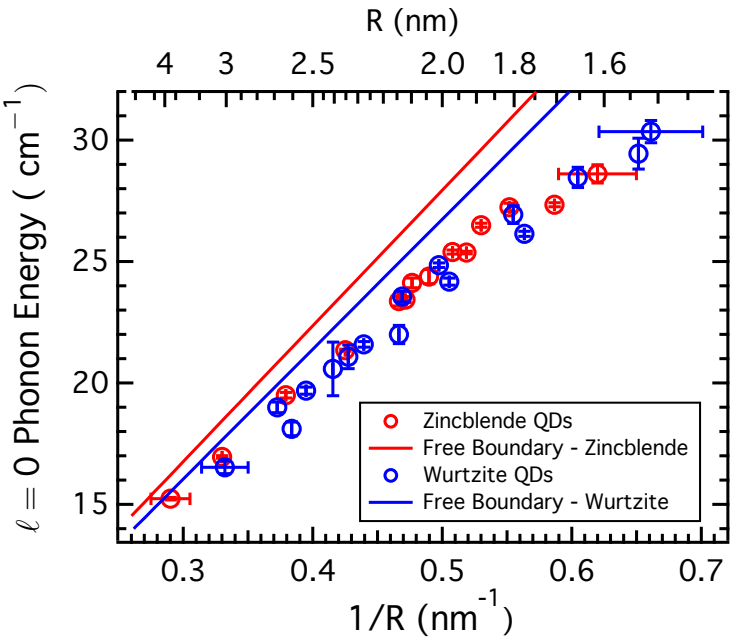

Figure 4-10: Plot of $\ell = 0$ phonon energy as a function of $1/R$ for zincblende (red) and wurtzite (blue) QDs, both with oleic acid ligands. The theoretical predictions based on the free boundary condition are plotted as solid lines. Error bars: y-error bars represent the standard deviation between four measurements, while x-error bars represent uncertainty in sizing based on the sizing curve in Appendix A. The x-error bars are only shown for the smallest and largest QDs of each type for clarity.

4.5 Effect of Ligand Properties on the ℓ=0 Phonon Energies of CdSe QD Cores

To further understand the effect of surface ligands on core vibrations, we performed a series of solution phase ligand exchanges on a series of QD cores with both linear, saturated alkanethiol ligands and *para*-substituted aromatic thiol ligands (also called benzylmercaptans).

4.5.1 Alkanethiol Substitution Results

To initially probe the effect that surface-bound ligands have on the vibrational frequencies of the QD core, we performed ligand exchange experiments with a set of straight-chain alkanethiols of variable length. For all QD sizes investigated, the energy of the radial breathing mode red-shifted monotonically with increasing ligand length between hexanethiol (C_6) and octadecanethiol (C_{18}). This result supports the proposed ligand mass effect in which larger ligand masses result in a greater perturbation of the acoustic resonant frequency of the QD.In Figure 4-11, the measured phonon energy for thin films of ligand exchanged QDs is plotted as a function of inverse QD size, and compared to the CdSe elastic sphere free boundary condition model. As observed for the case of QDs with native ligands (Figure 4-8), the free boundary condition model overestimates the phonon frequency for all sizes, with the greatest deviation ($\sim 30\%$) smaller than the predicted energy occurring for the smallest QDs. The core-ligand model developed above can quantitatively capture the observed shifts in acoustic mode energy with ligand length. The gray lines of Figure 4-11a delineate the core-ligand model fits to the hexanethiol and octadecanethiol data series, where the ligand shell thickness is derived from the X-ray scattering study by Weidman, *et al.*, [109] and the only free fitting parameter is the ligand longitudinal sound velocity. The fitted sound velocity for all ligands are tabulated in Table 4.1. These fitted ligand sound velocities compare favorably to earlier mechanical measurements of linear alkanethiols self-assembled on gold surfaces by DelRio *et al.* (Figure 4-11b) [110]. The close match between the sound velocities extracted from this work and previously measured elastic properties of surface-bound molecules in self-assembled monolayers (SAMs) implies a similarity in the elastic behavior of organic molecules bound in either flat (SAM) or curved (QD) geometries. The difference in the longitudinal velocities (v_l) for various lengths of alkanethiol ligands with equal assumed shell densities (ρ) suggests that the elastic stiffness also plays a role in the redshift in phonon frequency with increasing carbon chain length, as v_l is related to the elastic modulus along the radial direction, c_{11}, through $v_l = \sqrt{c_{11}/\rho}$.

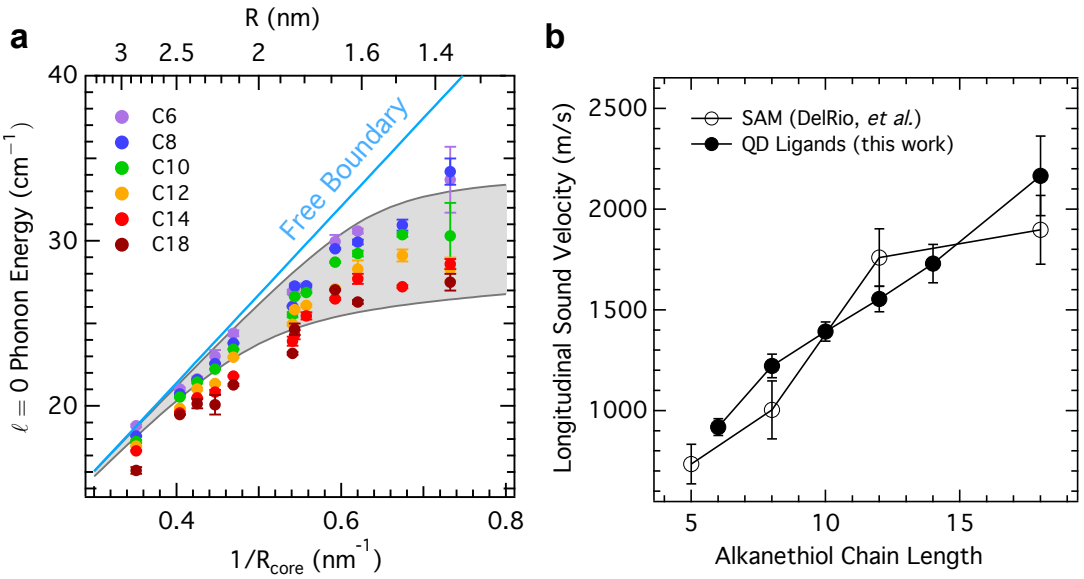

Figure 4-11: (a) Ligand length dependence of the $\ell = 0$ QD phonon energy. The blue line represents the prediction based on the free-boundary condition. Colored circles indicate phonon energies for alkanethiol ligands with carbon number indicated in the legend, with y-axis error bars corresponding to the standard deviation of at least four measurements. The gray lines represent fits based on the model from Figure 4-8b to the hexanethiol (upper line) and octadecanethiol (lower line) data, with shaded gray region suggesting range of tunability for QD phonon energies. (b) Fitted ligand sound velocity as a function of alkanethiol chain length (number of carbons) from the QD data in a (filled circles) compared to self-assembled monolayer data by DelRio, *et al.* (empty circles) [110]. Error bars reflect the one standard deviation confidence interval for measurements and fits.

4.5.2 Benzylmercaptan Substitution Results

To determine whether the observed change in acoustic phonon energy with ligand length is entirely a mass effect, we performed a second series of ligand exchange experiments with *para*-substituted benzylmercaptans (inset in Figure 4-12). Changing the *para*-substituent allows subtle tuning of the mass of these molecules while greatly affecting neither the physical molecular size, due to the conserved aromatic structure, nor the strength of the ligand-surface bond, due to the methylene unit that separates the substituted benzene from the thiol binding group (Figure 4-12). As observed for linear alkanethiols, more massive substituted benzylmercaptans also shift the QD resonant vibrational frequency to lower energies. Significantly, this

Table 4.1: Fitted sound velocities for native and exchanged ligands on CdSe QD cores.

Ligand	L_{ligand} (nm)	v_l (m/s)
ODPA	1.3	2424 ± 70
OA	1.3	2439 ± 253
$C_6H_{13}SH$	0.45	919 ± 42
$C_8H_{17}SH$	0.61	1222 ± 59
$C_{10}H_{21}SH$	0.76	1392 ± 48
$C_{12}H_{25}SH$	0.91	1554 ± 63
$C_{14}H_{29}SH$	1.07	1730 ± 95
$C_{18}H_{37}SH$	1.38	2165 ± 197

behavior is observed regardless of the electron donating or withdrawing character of the substituents (X = H, Me, F, OMe, Cl, tBu, CF_3, Br) indicating that the mechanical properties of the ligand—rather than the electronic or chemical functionality—determine its effect on the phonon frequency.

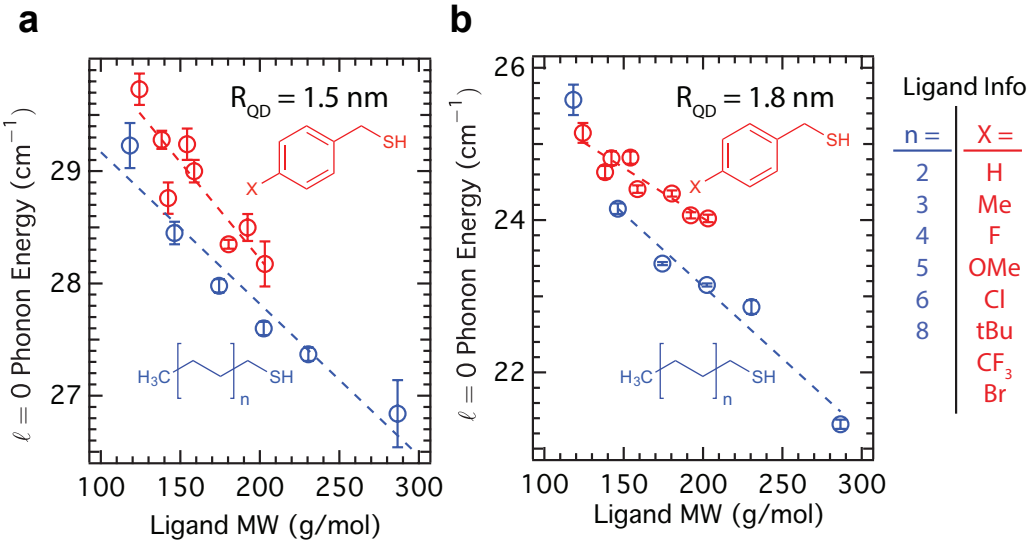

Figure 4-12: Relationship between measured phonon energy and the ligand molecular weight for a series of alkanethiols (blue circles) and benzylmercaptans (red circles) QDs of radius 1.5 nm (a) and 1.8 nm (b). Legend at right of (b) orders *para* substituents by increasing molecular weight. Dotted lines are linear fit to data and serve as a guide to the eye. 10 cm-1 = 0.3 THz.

While the mass effect is consistent across both ligand series, for the same ligand molecular weight, benzylmercaptan ligands result in systematically higher energy vibrations than alkanethiols (Figure 4-12). These data suggest that the ligand

molecular mass only partially determines the phonon energies of QD cores, with other factors possibly including ligand stiffness (e.g. aromatic rings with different elastic modulus, c_{11}, than aliphatic chains) or ligand packing density (which in turn affects the density, ρ, of the ligand shell).

4.5.3 Matrix Effect

In order to verify that the observed changes to the QD phonon frequency with ligand mass were not due to changes in the matrix/environment, we tested the effect of the surrounding matrix on QD phonon modes separately. QDs were embedded in one of several types of matrices (decane solution, poly(methyl methacrylate) film, and octadecane (wax) film) and compared to thin films of QDs without a surrounding matrix. There is a small decrease in the measured $\ell = 0$ phonon energy between thin films of QDs and matrix-embedded QDs, but this change is small (~ 0.5 cm^{-1}) compared to the observed ligand effect, which can change the measured phonon energy by 3-8 cm^{-1}. These results emphasize that the ligands, rather than the surrounding matrix, are most responsible for observed deviations from ideal behavior.

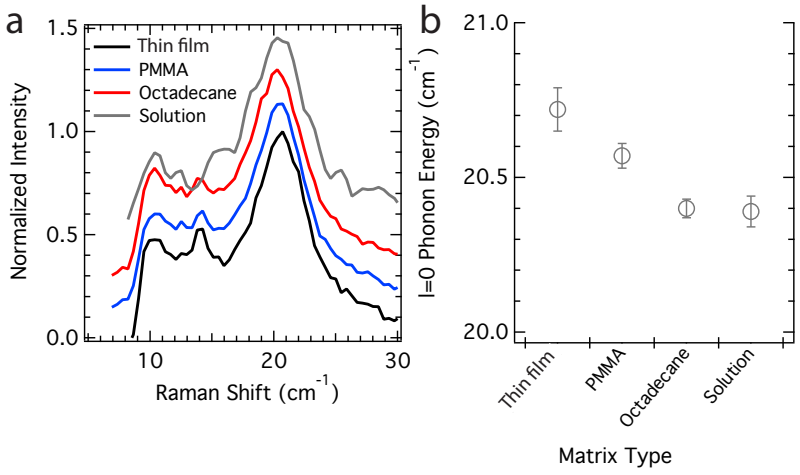

Figure 4-13: QDs after ligand exchange with alkanethiols (left) and benzylmercaptans (right) of different sizes show no change in the absorption onset, which indicates the QD size remains constant upon ligand exchange, and the ligand exchange does not affect the QD Raman spectrum through changing QD size.

4.6 Effect of Inorganic Shell Thickness on Heteronanocrystal Acoustic Phonon Energies

The highly fluorescent QD materials used for fluorescence downconversion nearly always include an epitaxially grown shell of a higher band-gap semiconductor around the central core [10, 11]. The inorganic shell can deter QD charging [111] and blinking [11], in addition to confining the wavefunction of the charges in the QD and passivating dangling bonds at the surface of the core. To understand how this shell impacts the acoustic phonon spectrum of core-shell heteronanocrystals, we synthesized a set of nanocrystals with a constant size CdSe core and variable thickness CdS shell according to the method of Coropceanu [112]. Aliquots were removed from the reaction mixture in order to achieve different shell thicknesses. All sample aliquots were dispersed into hexanes and precipitated twice with acetone to purify. Absorption spectra and TEM images for CdS overcoated CdSe QDs are shown in Figure 4-14.

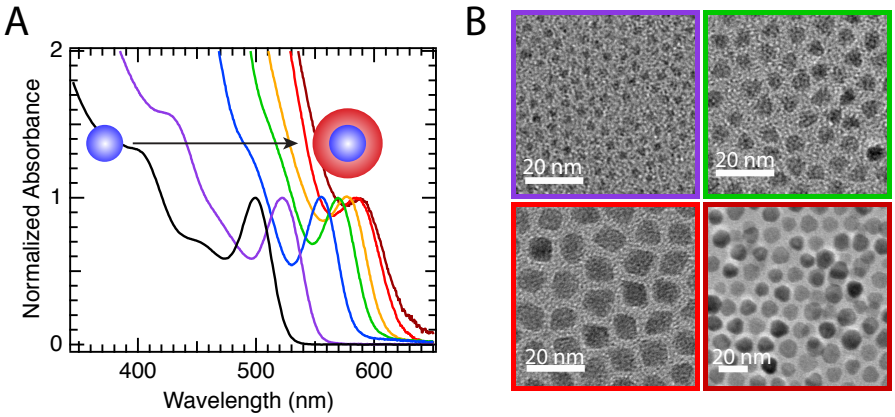

Figure 4-14: (a) Absorption spectra of CdS-overcoated CdSe QDs at various stages of shell growth. (b) TEM images of nanoparticles with colored outlines corresponding to the same color traces in (a).

The low-frequency Raman spectra of these particles reveal a monotonic redshift in acoustic phonon frequencies with increasing shell thickness (Figure 4-15), similar to the size dependence of the CdSe-only acoustic phonon modes (Figure 4-8). For core-shell materials, if there is a weak acoustic phase matching at the core-shell interface,

then the low-frequency Raman spectrum is a superposition core-only or shell-only vibrational spectra [113]. On the other hand, for a well-alloyed interface, there is continuity of both the displacement vectors and the stress for the perpendicular to the radial wave vector such that the whole nanocrystal vibrates as one body, as expected based on the similarity of elastic constants at the epitaxially bonded core-shell interface [114]. For the largest nanocrystals, a second peak at double the energy of the first is assigned to the overtone of the $\ell = 0$ mode, corresponding to an acoustic vibration with the same angular symmetry as the $\ell = 0$ peak but with a node in the radial wave vector—this phonon feature will be discussed more extensively in Chapter 5. These data demonstrate that for core-shell nanocrystals, the ℓ =0 phonon mode energy can be tuned by more than 20 cm^{-1} ($\sim$ 70% reduction in frequency compared to the core-only nanocrystal) by a change in shell thickness of $\sim$ 3 nm (Figure 4-15b).

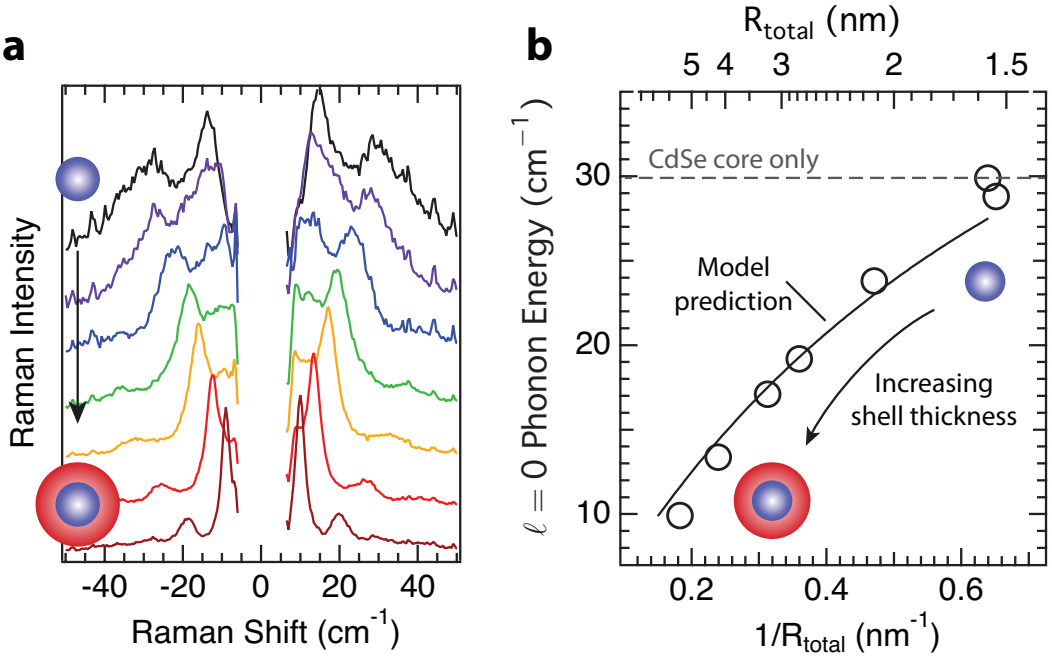

Figure 4-15: (a) Raman spectra of a series of CdSe/CdS core/shell QDs with identical core size but increasing CdS shell thickness from top to bottom. (b) Size-dependence of the $\ell = 0$ phonon energy corresponding to the spectra shown in (a). Open circles denote experimental data and solid line indicates the prediction of the core-shell-ligand model described in the text with zero fitting parameters.

The core-shell-ligand model, an extension of the core-ligand model depicted

schematically in Figure 4-8b, accurately predicts the measured size dependent phonon energies with zero fitting parameters after accounting for the inorganic shell between the core and ligand materials (Figure 4-15, black line). For the model, the ligand sound velocity was obtained from a size series of oleic acid capped core-only QDs (Figure 4-9), and the elastic properties of CdSe and CdS were obtained from bulk measurements. The excellent agreement between model predictions and experiment demonstrate the robustness of the model even for different materials systems, and suggest it can be used as a predictive tool to calculate acoustic phonon frequencies for QD nanomaterials. Based on both Figures 4-11 and 4-15, we demonstrate the feasibility of significant synthetic control over the nanoparticle vibrational spectrum by changing the mass and elastic moduli of individual layers of core-shell-ligand QDs without altering other aspects of the QD photoluminescence.

4.7 Discussion & Conclusions

We have demonstrated not only that the QD acoustic phonon energies vary with nanocrystal core size, but also with inorganic and organic surface chemical modification. The size dependence of the QD acoustic phonon energies deviates from the $1/R$ dependence predicted for an elastic sphere, especially for small QD radii where the mass of the bound ligand represents a significant fraction of the total mass of the system. Increasing the mass of the surface ligand reduces the acoustic phonon energy of the nanocrystal core, an effect that translates across several different types of ligand structure. This effect can be described entirely classically, to first order, with a continuum mechanics model relying only on bulk properties of elastic solids.

We note that the presented model is perfectly elastic, and would therefore predict a δ-function phonon linewidth in the absence of other factors, contrary to the observed finite linewidth (Figure 4-7). Potential contributors to the linewidth include QD polydispersity, multiphonon effects, and anharmonic coupling at the surface [115]. Among these, our results suggest that the polydispersity of the QDs only accounts for a small fraction of the observed linewidth, as QDs with varying polydispersity have

similar measured $\ell = 0$ linewidths (Figure 4-16). The $1/R$ scaling of the linewidth with QD size observed in Figure 4-7 suggests that environmental damping plays a role, as both the real and imaginary parts (corresponding to energy and linewidth, respectively) of the eigenvalue solution for a sphere in a matrix are known to vary inversely with the radius [94]. Environmental damping can also affect phonon energies via energy dissipation. In particular, the data in Figure 4-11 reveal that for large QDs ($R > 2.5$ nm) the measured phonon energy continues to exhibit a ligand-dependent deviation from the free-boundary prediction, whereas our fully elastic model predicts convergence with the free-boundary prediction at these large sizes. A model of an elastic sphere in a fluid could explain this constant offset from the free-boundary prediction [116], but only if the density of the liquid were larger than the density of the core, which is unphysical. Deeper understanding of the ligand effect for various molecular structures across all sizes of QDs may require molecular dynamics or quantum chemistry calculations (*e.g.* density functional theory), which we continue to study in future investigations.

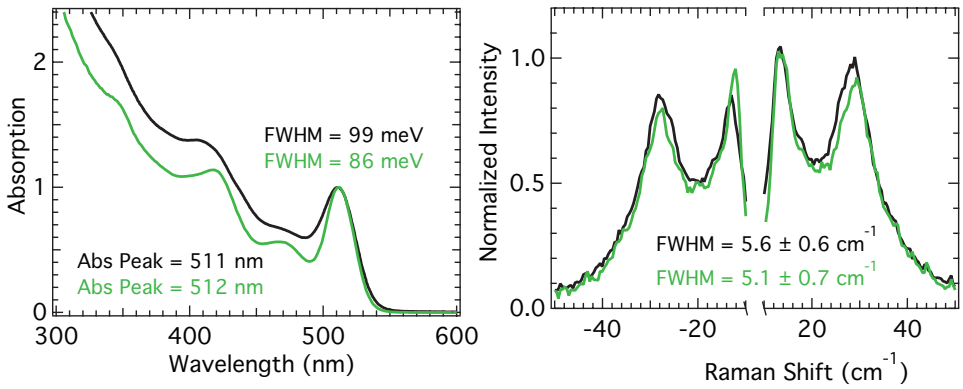

Figure 4-16: Absorption (left) and Raman (right) spectra for two batches of QDs with nearly identical average size (based on first absorption feature position) but varying polydispersity (based on first absorption feature width). The Raman spectra demonstrate that though there is a small effect of polydispersity on the Raman linewidths in these two samples, the difference is comparable to the error within the fitting procedure.

Our continuum core-ligand model both qualitatively and quantitatively captures the dependence of the acoustic mode frequency as a function of QD size and ligand

length. The good agreement between our extracted ligand sound velocities and those measured for alkanethiol SAMs by atomic force microscopy [110] suggests that it is possible to use acoustic phonon energies to infer elastic moduli for an average ligand shell surrounding QDs in thin films. To the best of our knowledge, the mechanical properties of the ligand medium in self-assembled QD systems are yet unknown, and only bulk properties of the colloidal assembly have been measured [107]. This knowledge could be useful for understanding heat transport at the individual QD length scale [30]. Additionally, this work provides some insight into methods to engineer thermal conductivity through vibrational density of state modulation in accordance with the model from Figure 1-13.

In addition to the ligand effect, growing an inorganic shell on QD nanocrystals also results in a redshift of the acoustic phonon energy. Through using a higher bandgap shell to create a type-I QD heterostructure, it should be possible to substantially adjust QD phonon energies without substantially changing emission color. Experiments to understand the effects of other shell materials on nanocrystal phonon energies are ongoing in our group. Combined, the nanocrystal size, ligand identity, and inorganic shell thickness provide a toolbox with which to engineer nanocrystal vibrational energies tailored for a specific application.

4.8 Chapter-Specific Acknowledgements

The theoretical modeling presented in this Chapter was entirely completed by Elizabeth Lee with help from Adam Willard. TEM and SAXS characterization were largely done by Nabeel Dahod, though several CdSe/CdS TEM images were taken by Mark Weidman.

Chapter 5

Temperature-Dependent Raman Spectroscopy of QDs

5.1 Motivation

The fundamental insights into the QD vibrational spectrum elucidated in Chapter 4 provide a launch point for further investigations into the physics underlying QD vibrations. Though that chapter demonstrated predictable methods to tune to QD Raman spectrum through the nanocrystal size, ligands, and shell, many open questions remain. Why do ligands with the same mass produce different QD vibrational energies? What influence does ligand binding group group (*e.g.* thiol, amine, phosphonic acid, carboxylic acid, etc.) have on the vibrational frequencies of the QD core? Why do large QDs, for whom ligand mass is negligible, continue to show red-shifted phonon energies compared to the predictions based on the core-ligand model? Does the model remain predictive for other core/shell/ligand compositions? Investigations of many of these questions are currently underway in our laboratory, but a different question serves as the focus for this chapter: How does cooling affect vibrational frequencies and amplitudes, and what does this say about the nature of the modes measured?

5.2 Background: Phonon Occupation and Lattice Expansion

5.2.1 Temperature Dependence of Phonon Occupation

Phonons are bosons, which, unlike fermions, may have more than one particle occupying the same quantum state. The occupation number $\langle n \rangle$ of a quantum state with energy E is given by the Bose-Einstein distribution function

$$\langle n \rangle = \frac{1}{e^{-E/kT} - 1}, \tag{5.1}$$

with k equal to the Boltzmann constant and T the temperature of the material. Figure 5-1a shows the average occupation $\langle n \rangle$ for phonons ranging in energy from 10-500 cm^{-1} for several different temperatures. It is immediately clear that the lowest energy phonons have non-negligible occupation even at very low temperatures (10 K); conversely, vibrations of even a few hundred cm^{-1} are effectively frozen out even at room temperature. The same information can be visualized differently, as in Figure 5-1b, where the occupation number is plotted as a function of temperature with several different phonon mode energies indicated. Near room temperature only phonons with energy less than ~ 200 cm^{-1}, where $E_{\text{phonon}} \approx kT$, have significant occupation.

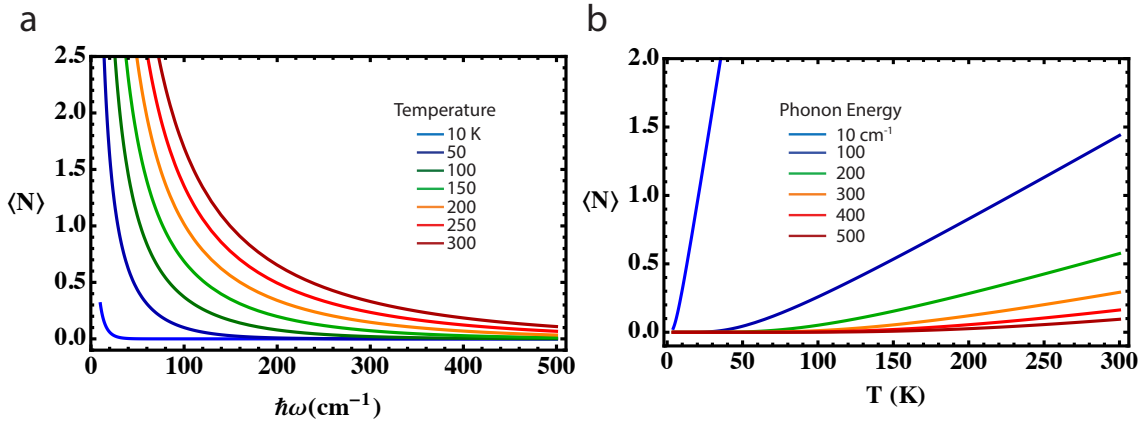

Figure 5-1: a) Average phonon occupation $\langle n \rangle$ vs. phonon energy for several different temperatures. b) Average phonon occupation vs. temperature for several different phonon energies. Both plots are derived from Equation 5.1.

Temperature Dependence of Raman Intensities

Both single phonon and multiphonon processes exhibit temperature-dependent probabilities in Raman spectroscopy [40]. Raman spectroscopy measures the creation or annihilation of a phonon; in quantum mechanics, this can be written mathematically through the creation and annihilation operators. The transition probability for the creation of a phonon (giving rise to the Stokes line in the Raman spectrum) is given by

$$\langle\psi(\langle n\rangle)|\mathbf{a}^{+}|\psi(\langle n\rangle+1)\rangle=(\langle n\rangle+1)^{\frac{1}{2}}, \tag{5.2}$$

where $\mathbf{a}^{+}$ is the creation operator. Similarly, for the annihilation of a phonon (the anti-Stokes line) the transition probability is

$$\langle\psi(\langle n\rangle)|\mathbf{a}^{-}|\psi(\langle n\rangle-1)\rangle=(\langle n\rangle)^{\frac{1}{2}}, \tag{5.3}$$

where $\mathbf{a}^{-}$ is the annihilation operator. Therefore, for a one-phonon process, the Stokes intensity is proportional to $\langle n\rangle+1$ and the anti-Stokes intensity is proportional to $\langle n\rangle$.

In temperature-dependent Raman measurements, it can be difficult to ensure that the irradiated sample volume and focal plane are consistent for all temperatures, making it difficult to compare absolute intensities across many different spectral measurements, so it is often easier to look at the ratio between the Stokes and anti-Stokes peak intensities. The anti-Stokes to Stokes intensity ratio is given by

$$\frac{I_{AS}}{I_S}=C*\exp\left(\frac{-E}{kT}\right), \tag{5.4}$$

where the constant C is related to the photon (not phonon) energies of the Stokes and anti-Stokes lines, and $E=\hbar\omega$ is the phonon energy. This relationship between Stokes and anti-Stokes intensity has been used as an internal temperature measurement for Raman microscopy experiments, but the sensitivity is not high enough to measure

temperature changes much below 1 K. Figure 5-2 shows the temperature difference δT that can be measured using phonons of various frequencies ν for different count rates. To achieve temperature sensitivity of below 1 K requires measuring 50,000 counts of Raman scattered light from phonons of energy ~ 100 cm^{-1}. Achieving this sort of count rate leads to other difficulties, such as defocusing during long integration times, and prevents dynamic temperature measurements.

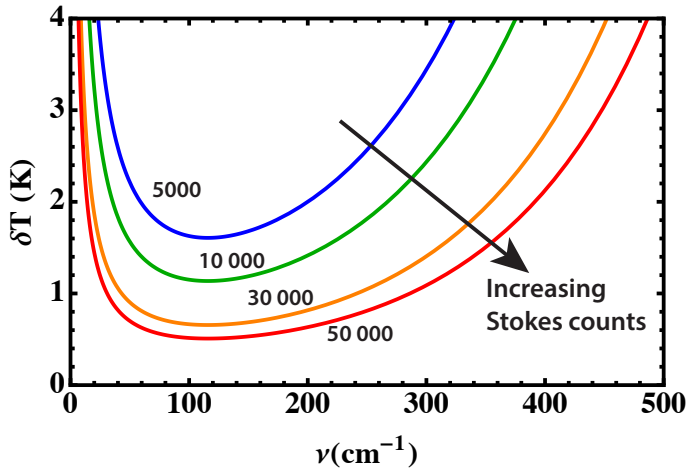

Figure 5-2: Measurable change in temperature δT possible to achieve using the Stokes to anti-Stokes ratio in Raman spectroscopy as a function of phonon energy ν.

Temperature Dependence of Multiphonon Processes

It is worth noting that for a two phonon process, the scattering probabilities for two single phonon process are simply multiplied, such that the two-phonon Stokes intensity goes as $\langle n \rangle^2 + 2\langle n \rangle + 1$, and the anti-Stokes intensity varies as $\langle n \rangle^2$. Thus, the relative intensity of a multiphonon peak is expected to increase more rapidly with temperature than a fundamental peak. This will be used to assign peaks in the QD Raman spectrum in Section 5.4.

5.2.2 Bond Anharmonicity and Lattice Expansion

On a macroscopic scale, thermal expansion results in warping and buckling in railroad track, cracks in buildings, and delamination of different materials their interface after

many cycles of cooling and heating. While there exist a variety of engineering tools to mitigate the impact of thermal expansion on structures, the source of this phenomenon fundamentally lies with the physical chemistry of the material, and the anharmonicity of chemical bonds.

The development of the normal vibrational modes for a solid material in Chapter 1, Section 1.3.1 assumed that the potential energy function describing the atoms within the crystal was the parabolic potential associated with the simple harmonic oscillator. If bonds were, in fact, perfectly described by the harmonic oscillator model, there would be no thermal expansion because the harmonic potential is symmetric about the mean bond distance so the interatomic spacing would be temperature-invariant. This can be seen schematically in Figure 5-3, where the blue curve represents the harmonic potential, and the blue circle indicates the equilibrium bond displacement. Higher temperatures mean greater kinetic energy for the atoms in the lattice, and, based on the phonon occupation data from Figure 5-1, greater occupation of higher energy vibrational modes. In the schematic illustration in Figure 5-3, higher temperature means occupation of the higher energy "rungs" on the harmonic oscillator potential energy ladder.

In order to accurately model observed phenomena such as thermal expansion and thermal conductivity, the inter-atomic potential must be *anharmonic*, meaning that additional terms are included in the description of the potential energy. Several alternative potentials have been proposed, including the Morse potential [117] and the Lennard-Jones potential [118], both of which incorporate the interplay between Pauli repulsion at very small interatomic distances and van der Waals attraction at larger displacements. The Morse potential is contrasted with the harmonic oscillator potential in Figure 5-3, and demonstrates two key characteristics: the equilibrium bond distance increases with energy, and the spacing between levels decreases with increasing energy.

Temperature dependent vibrational spectra of many materials can be understood in the context of the anharmonic potential shown in Figure 5-3. In general, the phonon frequencies of materials blue-shift upon cooling, which is consistent

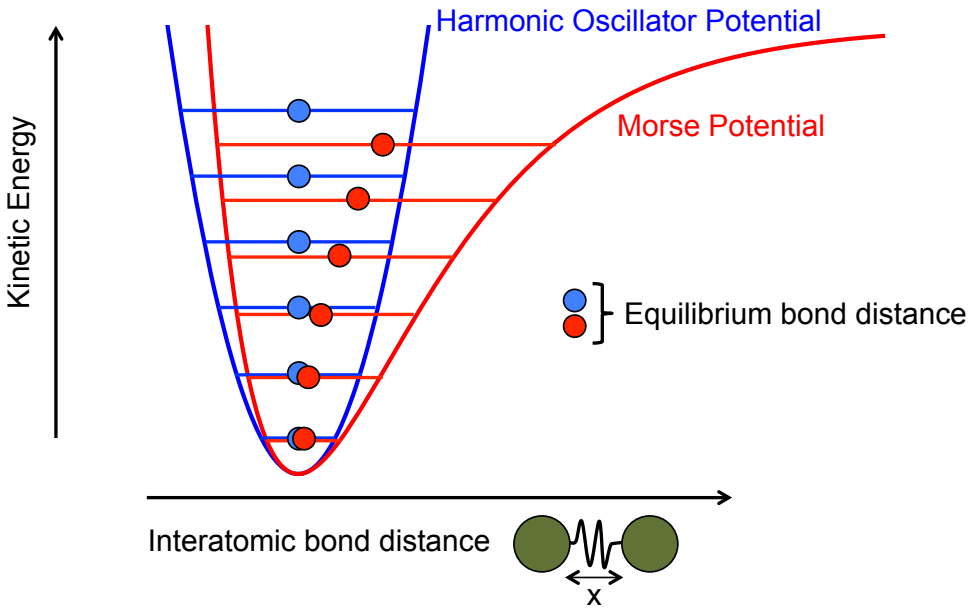

Figure 5-3: Schematic showing the harmonic oscillator potential in blue and the Morse potential in red (other potentials, such as the Lennard-Jones, look qualitatively similar to the Morse potential). The equilibrium bond distance remains constant across all energies in the harmonic oscillator model, but increases with energy in the Morse potential. Similarly, the level spacing is constant for the harmonic oscillator but decreases in the case of the Morse potential.

with the shortening of the equilibrium bond distance at low temperatures (low phonon occupation). The shorter equilibrium bond distance at low temperatures is qualitatively similar to an increased inter-atomic force constant k in the harmonic oscillator model, which increases phonon frequency ($\omega \propto \sqrt{k/\mu}$ for reduced mass μ). In addition to this volume changing effect, the phonon frequency also experiences a purely temperature effect due to higher order anharmonicity terms (Δ_3 and Δ_4 in the pseudo harmonic Hamiltonian) [119, 120]. These volume and temperature effects can be modeled for a phonon mode i with frequency ω as [119]

$$\left(\frac{\mathrm{d}\ \ln\ \omega_i}{\mathrm{d}T}\right)_P = \left(\frac{\mathrm{d}\ \ln\ V}{\mathrm{d}T}\right)_P \left(\frac{\mathrm{d}\ \ln\ \omega_i}{\mathrm{d}V}\right)_T + \left(\frac{\mathrm{d}\ \ln\ \omega_i}{\mathrm{d}T}\right)_V$$

$$= -\frac{\alpha}{\kappa}\left(\frac{\mathrm{d}\ \ln\ \omega_i}{\mathrm{d}P}\right)_T + \left(\frac{\mathrm{d}\ \ln\ \omega_i}{\mathrm{d}T}\right)_V, \tag{5.5}$$

for isothermal compressibility $\kappa = (\mathrm{d}\ \ln V/\mathrm{d}P)_T$ and thermal expansivity $\alpha = (\mathrm{d}\ \ln\ V/\mathrm{d}T)_P$, where subscripts refer to the variable kept constant. In Equation 5.5, the first term on the right hand side of the equation refers to the effect on ω_i of changing the crystal volume without changing the temperature, while the second term refers to the pure temperature contribution at a constant volume. In addition to the frequency shift, the linewidth increases with temperature for most phonon modes. This increase in linewidth (inverse phonon lifetime) is due to both decay into lower energy phonons and scattering with other phonons in the lattice.

In an equivalent formulation, the change in phonon frequency can be given in terms of an explicitly volume effect $\Delta^{(1)}$ and an explicitly anharmonic effect due to phonon coupling $\Delta^{(2)}$ [121, 122] through

$$\omega(T) = \omega_0 + \Delta^{(1)}(T) + \Delta^{(2)}(T). \tag{5.6}$$

The volume effect $\Delta^{(1)}(T)$ is given by [122]

$$\Delta^{(1)}(T) = \omega_0 \left[\exp\left(-3\gamma \int_0^T \alpha(T')dT' \right) - 1 \right], \tag{5.7}$$

where ω_0 is the frequency at zero K, γ is the mode Grüneisen parameter (a constant describing the change in the phonon frequency of a mode with a change in crystal volume), and α is again the thermal expansivity, which makes $\Delta^{(1)}(T) \propto T$ at higher temperatures. $\Delta^{(2)}(T)$ has a more complex functional form dependent on phonon coupling due to bond anharmonicity and phonon scattering, but can either be proportional to T or T^2 (or higher) depending on the number of interacting phonons.

5.2.3 Example: Temperature Dependence of CdSe LO Phonon

The frequency and linewidth effects are clearly observed in the temperature-dependent Raman spectra of the bulk CdSe LO phonon (Figure 5-4). The spectra reveal, as expected, a redshift and broadening with increasing temperature for the LO phonon (Figure 5-4b). For a line fitted to the Stokes LO phonon energy between 100–300K

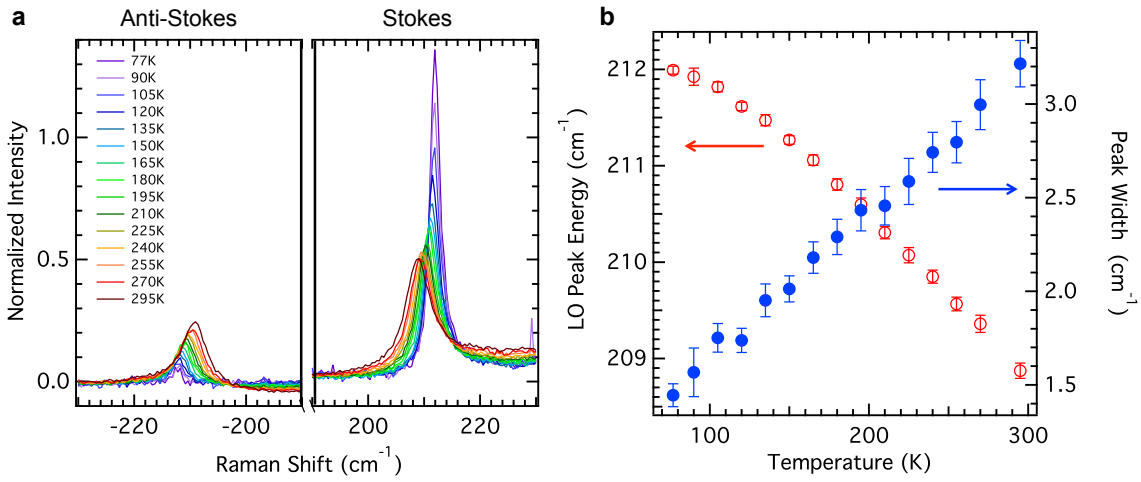

Figure 5-4: a) anti-Stokes and Stokes Raman spectra of the CdSe LO phonon as a function of temperature. The peak broadens and redshifts with increasing temperature. The magnitude of the Stokes peak appears to decrease due to its broadening. b) Plot of CdSe LO phonon frequency (red) and linewidth (blue) as a function of temperature. Error bars represent the error in the fitting parameters using a Gaussian fit to the peaks in (a).

for bulk CdSe in Figure 5-4, the slope $(\mathrm{d}\omega/\mathrm{d}T)_P$ is $-1.55(\pm 0.03) * 10^{-2}$ K^{-1}, nearly identical to the LO phonons from ZnS ($-1.55 * 10^{-2}$ [123]). While the isothermal compressibility κ and thermal expansivity α are known for bulk CdSe ($\alpha = 6.89 * 10^{-6}$ K^{-1} [124], $\kappa = 1.82 * 10^{-6}$ bar^{-1} [125]), it is impossible to separate the pure volume contribution from the thermal anharmonic contribution to the phonon frequency shift from Equation 5.5 without pressure dependent data. Pressure dependent data is also implicitly required for evaluation of the frequency shift in Equation 5.6, which relies on the Grüneisen prameter, equivalent to $(1/\kappa)(\mathrm{d}\ \ln\ \omega_i/\mathrm{d}P)_T$. While the Grüneisen parameter is unknown for the LO mode of bulk CdSe, a fit to the temperature-dependent phonon frequency data for the CdSe LO phonon using Equations 5.6 and 5.7 with fitting parameters ω_0 and γ yielded a reasonable match to the data (Figure 5-5). The fitted value of γ is larger than the value 1.1 found for the LO phonon of zincblende CdSe QDs [126], but is similar to the LO mode Grüneisen parameter for ZnS [123].

The temperature dependent linewidth of the CdSe LO phonon can be achieved

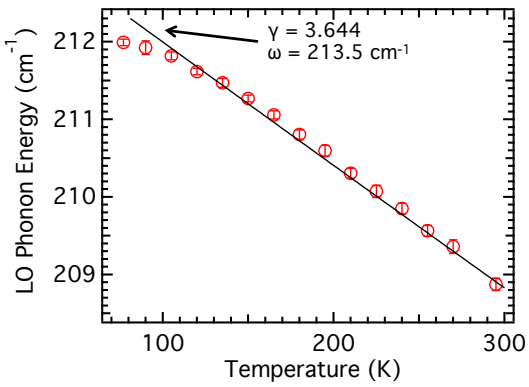

Figure 5-5: LO phonon energy as a function of temperature (red circles), and fit to the data using Equations 5.6 and 5.7. Fitted values of ω_0 and γ are indicated.

using several different models. Li, *et al.* assume that the principal contributors to the phonon linewidth in GaN is through LO phonon decay into either two or three acoustic phonons [122], Ohsaka assumes that the LO phonon of anatase TiO_2 either decays into two phonons or scatters with other phonons in the sample [120], and Bellowsa, *et al.* use a model where the phonons in a naphthalene crystal can decay into either two equal energy phonons or two phonons whose energy sums to the initial phonon [127]. The temperature dependent linewidth data from Figure 5-4 cannot be fit well considering only the decay of the LO phonon into two equal energy acoustic phonons, but the data is over-fit using other models. The linewidth is found to be linearly dependent on temperature in the range between 77–300K, which has been predicted for phonons with energy greater than kT (the LO mode of CdSe has energy very close to kT) when anharmonic terms up to third order are considered in the Hamiltonian [128].

It is important to note here that the LO phonon is essentially a "molecular" vibrational mode, where the atoms within a unit cell are vibrating relative to each other, rather than the much longer wavelength (and lower energy) acoustic phonons discussed throughout Chapter 4. This Chapter will examine shifts in phonon frequency and linewidth for acoustic phonons in CdSe QDs.

5.3 Methods

A custom ST-500 microscopy cryostat from Janis Research was used in conjunction with the microscope setup depicted in Section 2-7 for experiments in this Chapter. A correction collar was used with the microscope objective in order to correct for the 2mm of extra glass between the sample and the objective. The sample chamber was evacuated to $\sim 10^{-6}$ Torr before cooling to either liquid nitrogen or liquid helium temperatures. For liquid helium experiments, the helium was actively pulled through the cold finger with a vacuum pump. For all experiments, the sample was measured under vacuum. An initial measurement was performed at room temperature, then the sample was cooled to the minimum temperature (4K or 77K depending on the cryogen) and spectra were collected as the sample holder was heated. At each temperature, the sample (mounted on a sapphire substrate) was allowed to equilibrate for at least five minutes before the measurement. Typically, three spectra at each temperature were collected and averaged, each with an integration time of 60 seconds.

5.4 Assignment of Overtone Features in the Raman Spectrum of Large QDs

A careful observer would notice that for the largest QDs in Figure 4-15, a second (overtone) feature appears in the Raman spectra of large CdSe/CdS nanocrystals, which appears at almost exactly twice the energy of the fundamental (Figure 5-6). In fact, for the largest CdSe/CdS QDs, at least three overtone features are apparent at room temperature (Figure 5-6b).

These overtone features could result from one of two possible mechanisms: the creation (or annihilation) of two phonons, or a different phonon with the same symmetry as the fundamental but with a radial node (similar to the electronic 2S orbital). These two possibilities can be distinguished by their different expected temperature dependence. The two phonon process, as per Section 5.2.1, is expected to have an intensity proportional to $\langle n \rangle^2$, and therefore the ratio between the overtone

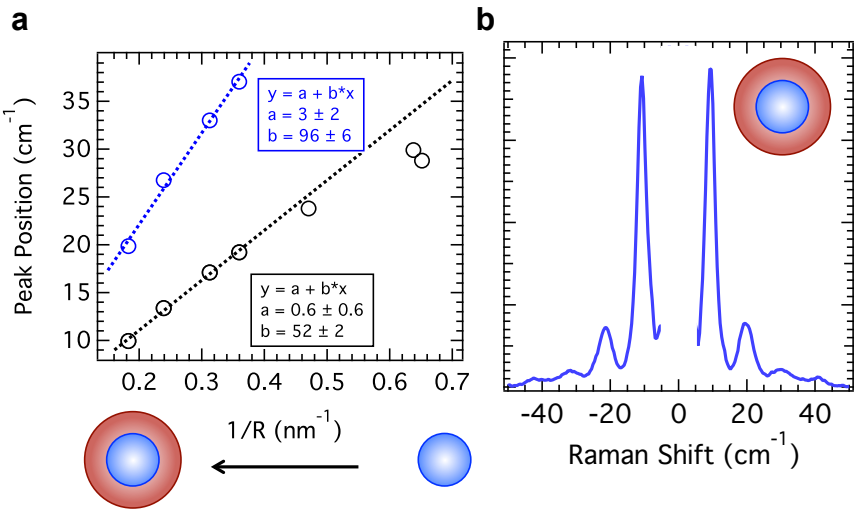

Figure 5-6: a) Plot of the phonon energy as a function of $1/R$ for the fundamental and overtone features for the CdSe/CdS overcoated QDs from Figure 4-15, revealing that the overtone energy is nearly twice the fundamental. b) Raman spectrum of the largest core-shell QD from Figure 4-15 with at least three overtone features visible.

and the fundamental intensities (I_o/I_f) should, to first order in the Taylor expansion, be given by

$$\frac{I_o}{I_f} \propto \frac{kT}{\hbar\omega_f} \tag{5.8}$$

where k is Boltzmann's constant, $\hbar$ the reduced Plank constant, and ω_f the frequency of the fundamental. In contrast, if the overtone is a different mode altogether, then the ratio between the overtone and fundamental intensities should be constant with temperature. Figure 5-7 shows schematic illustrations of both potential processes with their expected temperature dependence.

To determine the origin of the overtone peaks, Raman spectra were collected for the large CdSe/CdS core-shell QD from Figure 5-6b for temperatures between 5K–300K. The resulting raw and normalized spectra are plotted in Figure 5-8, with the fundamental and overtone intensities plotted in panel c. The normalized spectra show effectively no change in the intensity ratio between the fundamental and overtone peak, and the plot of intensity as a function of temperature looks similar to Figure 5-7b. These results suggest that the "overtone" peak corresponds to the $n = 2$ spherical harmonic for the vibrations of an elastic sphere.

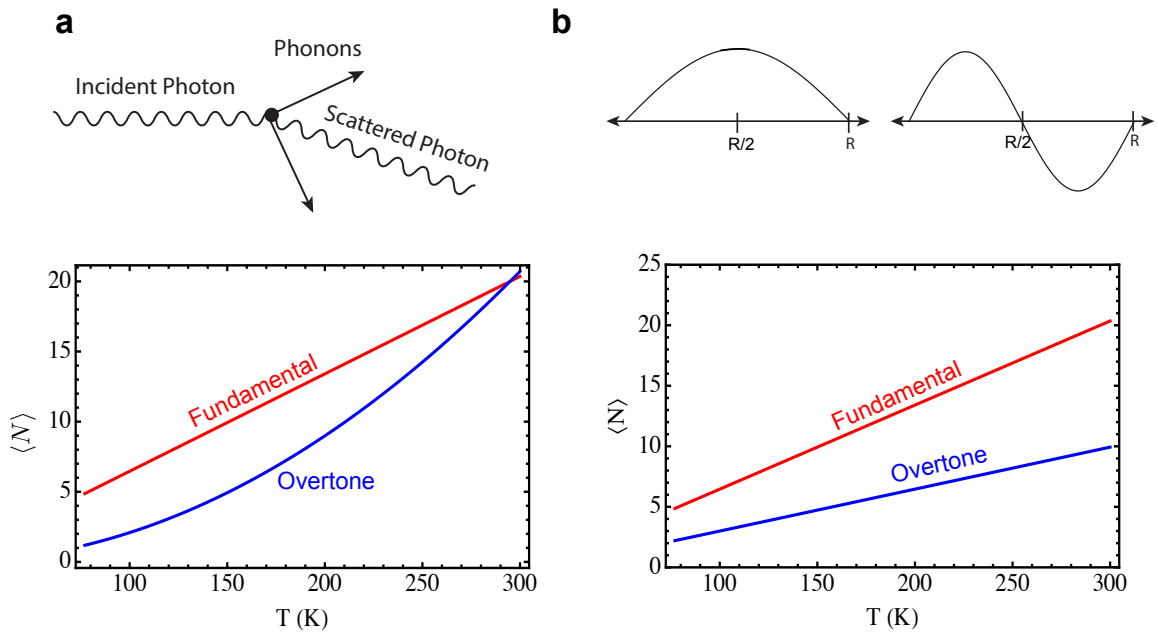

Figure 5-7: a) Schematic of multiphonon Raman process, with expected temperature dependence of the fundamental and overtone peaks. b) Schematic of acoustic phonon modes with varying radial nodes, with expected temperature dependence of fundamental and overtone intensities. For both (a) and (b), the energy of the fundamental is 10 cm^{-1}, consistent with the peak in Figure 5-6b.

Further evidence that the overtone peak is a separate vibration and not a two-phonon peak comes from the changes in peak position as a function of temperature. The frequency of both the fundamental and overtone peaks vary with temperature, as shown in Figure 5-9, but they change by nearly the exact same amount (~ 0.7 cm^{-1}). For a two-phonon process, the overtone peak energy would be expected to change by twice that of the fundamental since two fundamental phonons contribute. These data, in conjunction with the lack of temperature variation in the overtone to fundamental ratio, indicate that the higher order peaks in the low-frequency Raman spectra of large QDs originate from distinct phonons with different numbers of radial nodes rather than multiphonon processes. Interestingly, the linewidth of both the fundamental and overtone phonons (Figure 5-9c) are largely invariant with temperature, unlike the LO phonon of CdSe shown in Figure 5-4. This suggests that origin of the Raman linewidth is different for optical and acoustic modes, an observation worthy of further

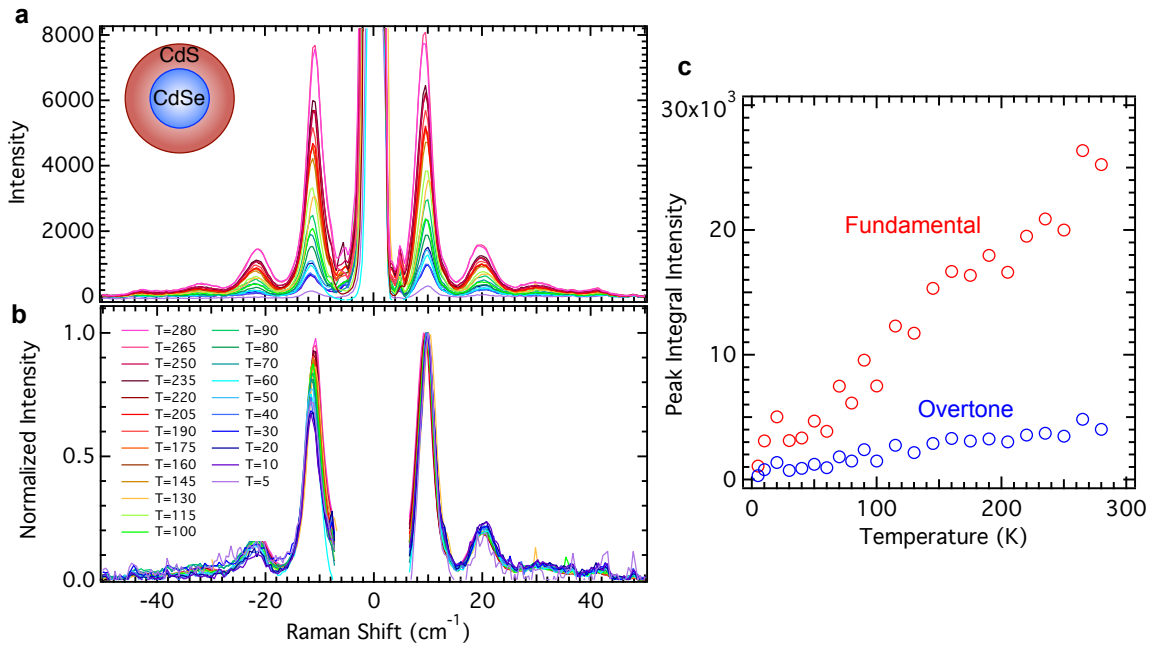

Figure 5-8: a) Raw and b) normalized (to maximum intensity of fundamental peak) Raman spectra for $\sim$ 10 nm core-shell CdSe/CdS QDs at temperatures ranging from 5K to 300K. c) Integrated intensities for the peaks corresponding to the fundamental ($\sim$ 10 cm^{-1}) and overtone ($\sim$ 20 cm^{-1}).

investigation.

Finally, the anti-Stokes to Stokes intensity ratios from Figure 5-8 reveal expected temperature dependences, and are plotted in Figure 5-9. The black lines are not fits to the data, but rather the prediction based on Equation 5.4 using $C = 1$ and the indicated energies. These data suggest that the anti-Stokes to Stokes ratio could be used for *in situ* temperature measurements at low temperatures with proper calibration, but the small change in ratio over much of the range between 100–300 K indicates that these phonons do not yield enough temperature contrast to be used at higher temperature.

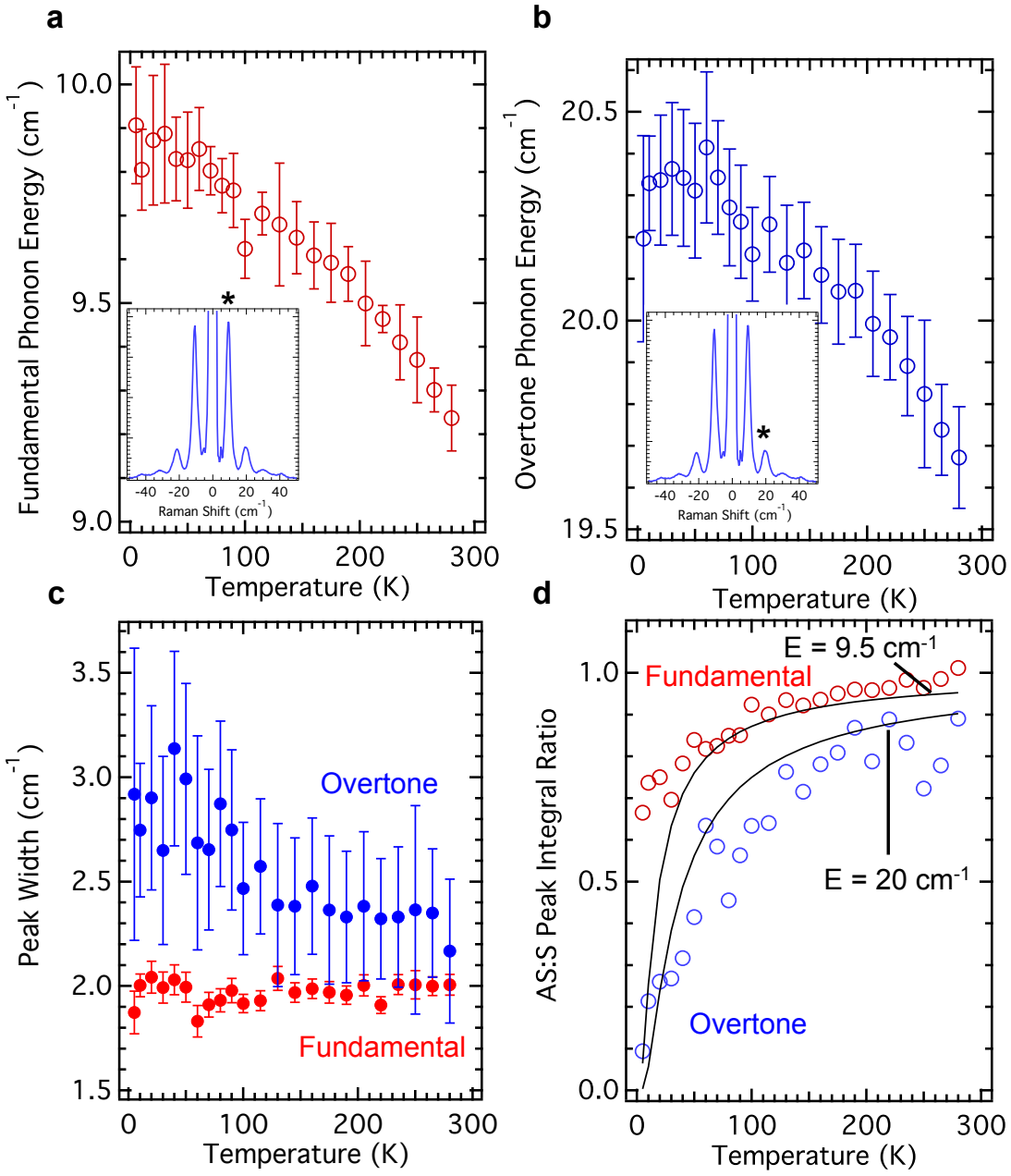

Figure 5-9: Temperature dependence of the phonon energy for the a) fundamental, and b) overtone peaks in the Raman spectra from Figure 5-8. Insets are the room temperature spectrum of the QD sample, with the peak of interest labeled with an asterisk. c) Phonon linewidth for both the overtone and fundamental phonons. d) Anti-Stokes to Stokes intensity ratio for the fundamental and overtone peaks plotted as a function of temperature and compared to the prediction based on Equation 5.4.

5.5 Temperature Dependent Phonon Energies and Linewidths

The measured acoustic phonon energies for the core-shell QDs of Figure 5-9 redshift with increasing temperature, similar to observations for bulk CdSe, but their linewidths remain invariant across the measured temperature range, contrary to observations of bulk LO phonons (see Figure 5-4b). This section will focus on temperature-dependent Raman spectra of core-only QDs, and the potential insights they provide into the source of the observed broadening and shifting of phonon energies.

Figure 5-10a shows the temperature-dependent Raman spectra for an example QD batch of $R \sim 2.2$ nm, with clear shifting in the phonon peak position as a function of temperature. Figure 5-10 (b-d) shows the fitted $\ell = 0$ phonon energy as a function of temperature for three different sizes of QD. As discussed in Section 5.2.2, the shift in frequency can be understood in terms of two effects: a lattice expansion, and an phonon interaction effect due to anharmonicity. Again, as for the CdSe LO phonon data, due to the lack of pressure-dependent data or acoustic mode Grüneisen parameter, it is impossible to differentiate entirely between the two effects. For all three QDs in Figure 5-10, the acoustic phonon energy varies linearly with temperature, with slope $(\mathrm{d}\omega/\mathrm{d}T)_P$ equal to $-4(\pm 0.5) * 10^{-3}$ cm^{-1}/K, about 1/3 that of the LO phonon. Additionally, as in Chapter 4, the QD surface ligands are a confounding effect because they, too, experience changing sound velocities, densities, and anharmonic vibrational coupling as a function of temperature.

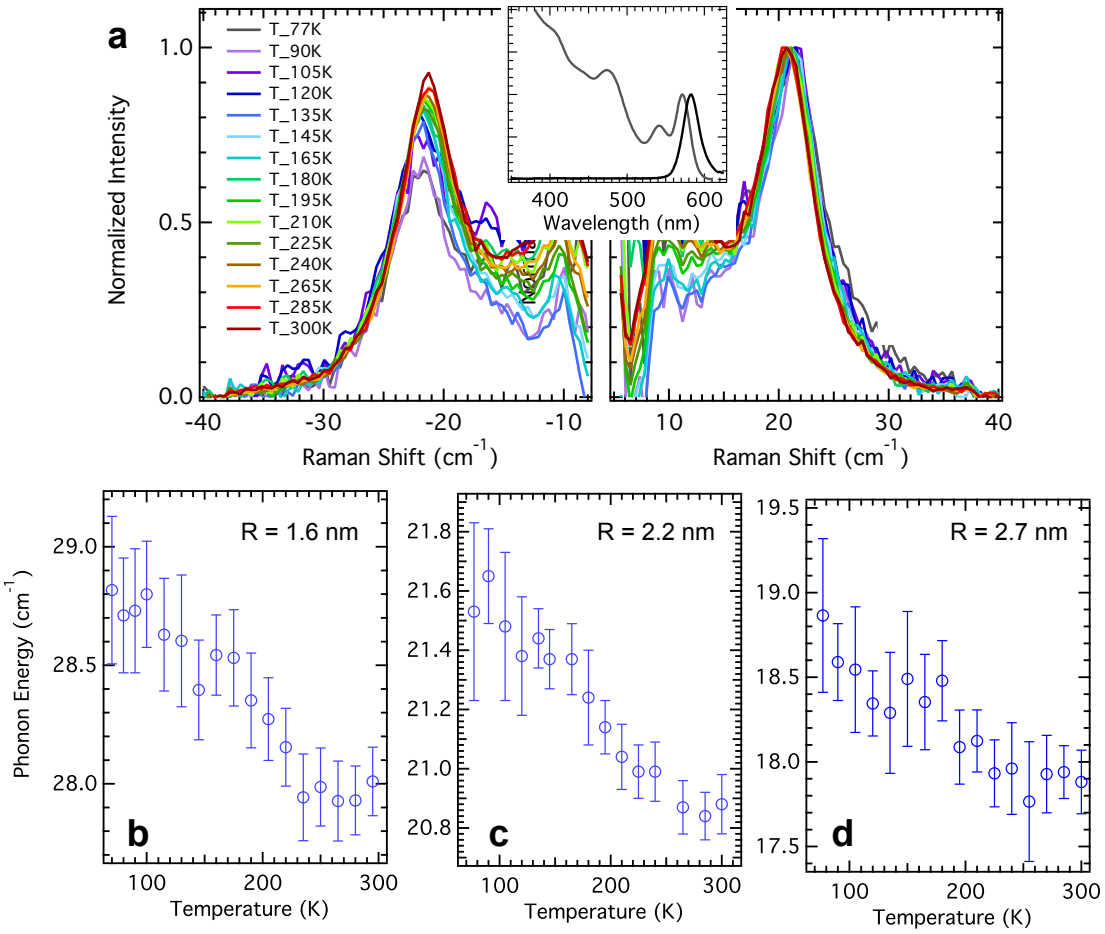

Figure 5-10: a) Normalized temperature dependent Raman spectra of $R = 2.2$ nm QDs, with inset absorption and emission spectra, for temperatures ranging from 77–300 K. The anti-Stokes (left) side reveals temperature-dependent changes in the phonon occupation through changes in intensity, and the small shift in phonon energy with temperature is also apparent on the Stokes (right) side. b-d) Plot of the $\ell = 0$ phonon energy as a function of temperature for three different sizes of QDs with radii indicated. Error bars represent 95% confidence interval for the center of the Gaussian fit through the procedure described by Figure 4-6. Only one spectrum was obtained at each temperature, so the source of these error bars are distinct from those in Chapter 4.

Though the acoustic phonon energies in CdSe QDs shift with temperature, their linewidths remain constant across the same temperature range (Figure 5-11). As expected, the magnitude of the linewidth is proportional to $1/R$, as in Figure 4-7. The same model for phonon energies and linewidths based on anharmonic interactions that successfully predicted the $\propto T$ dependence for the LO phonon linewidth dependence with temperature also predicts that the phonon frequency should be temperature independent for phonon frequencies $\omega << kT$, consistent with minimal decay of low energy acoustic phonons into other types of acoustic phonons. This suggests that when QD acoustic phonons are analyzed using Equation 5.6, the volume component $\Delta^{(1)}$ and not the temperature component $\Delta^{(2)}$ may be entirely responsible for the temperature dependent frequency shift, since $\Delta^{(2)}$ and changes in linewidth are both related to multiphonon interactions through anharmonic contributions to the vibrational potential. An additional effect that may play a role in the lack of observed linewidth is the inhomogeneous broadening due to polydispersity, which results in a linewidth not determined entirely by the phonon lifetime.

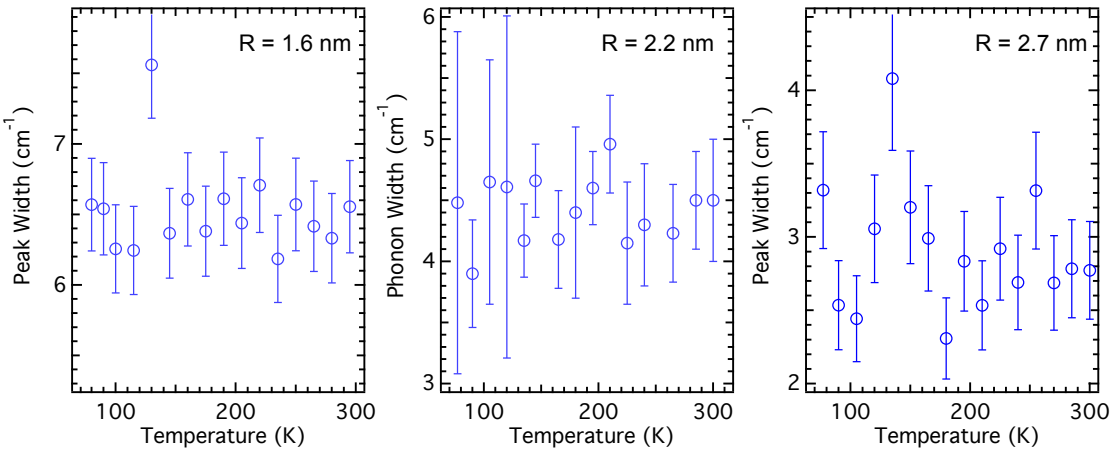

Figure 5-11: $\ell = 0$ phonon line widths as a function of temperature for same QDs as in Figure 5-10.

5.6 Summary and Conclusions

The temperature dependence of QD acoustic phonon intensities, energies, and linewidths have been documented for CdSe QDs and CdSe/CdS core-shell QDs. For the latter materials system, temperature-dependent Raman spectroscopy was able to identify and classify the overtone feature as a second harmonic feature rather than a two-phonon feature due to the negligible change in relative intensity of the overtone compared to the fundamental over the temperature range spanning 5–300K. All QDs, both core-only and core-shell, demonstrate a temperature-dependent shift in acoustic phonon frequency, but no change in linewidth. These data tentatively suggest that the volume expansion effect is more important than phonon-phonon interactions in determining the temperature-dependent frequency change, though more work needs to be done to clarify. There are remarkably few published results describing the effect of temperature on acoustic phonon frequencies and linewidths for any materials system (including bulk crystals), and this work represents an important initial study explicitly measuring the temperature dependence of acoustic phonons in QDs.

Appendix A

Colloidal Synthesis of Semiconductor Nanocrystals

The synthesis of colloidal CdSe QDs has been investigated for more than 20 years, progressing from the use of organometallic precursors such as Me_2Cd [129] to a variety of more benign and air-stable starting materials such as the CdO or $Cd(Oleate)_2$ used here. Innovation in the synthesis of QD materials was not a goal of this thesis, and literature methods were adapted by the author to synthesize all nanocrystals used in Chapters 4–5.

A.1 Wurtzite CdSe QDs

In this work, the wurzite QD synthesis was based on the work of Peng, *et al.*, which uses CdO and trioctylphosphine selenide (TOP-Se) as the Cd and Se precursors, respectively [98]. For this preparation, 120 mg of CdO, 0.54 g of Octadecylphosphonic acid, and between 5.6–6.0 g of Trioctylphosphine Oxide (TOPO, smaller cores were synthesized with less TOPO, larger cores with more TOPO, see [130]) were added to a 50 mL 3-neck round bottom flask and degassed under a vacuum of at least 200 mTorr for 1.5 hours. Under nitrogen, this mixture was heated to 310° C until the reaction mixture became a colorless clear solution. At this point, the temperature was increased to 360° C and 0.9 mL of a previously prepared solution of 1.6 M TOP-Se in TOP was swiftly injected with a syringe to the rapidly stirring mixture. The QDs

were allowed to grow in size for a variable period of time (typically 10 - 50 seconds) before removing the heating mantle and rapidly cooling the reaction mixture with flowing air from a heat gun. For size series experiments, aliquots of the growth reaction were removed using a glass syringe at various time points post-injection. Nanoparticles were purified by first adding the growth solution to 20 mL hexanes, then precipitating with acetone, followed by resuspension in hexanes and a second acetone precipitation. Purified nanocrystals were dispersed in anhydrous hexanes and stored under nitrogen.

The crystal structure of these particles were confirmed to be wurtzite through XRD measurements (Figure A-1). Many sizes of QD were synthesized over the course of this thesis, and in order to control for day-to-day variations in Transmission Electron Microscopy (TEM) contrast and therefore TEM sizing, a sizing curve relating the first absorption feature energy to the QD size was constructed from TEM measurements of 40 sizes of particles (Figure A-2). TEM was performed on a JEOL 2011 instrument operating at 200 kV. Samples were prepared by drop casting QD suspensions in hexanes onto copper TEM grids coated with an amorphous carbon support film. Nanocrystal sizes were extracted via image-analysis techniques previously reported [131]. Solution-phase small-angle X-ray scattering (SAXS) was measured on a Rigaku Smartlab with a Cu Kα source operating at 45 kV and 200 mA in transmission geometry with convergent beam optics and a 2 mm length limiting slit inserted. Samples were prepared by filling glass capillaries with suspensions of QDs in toluene at concentrations greater than 50 mg/mL. The experimental SAXS data were fit using Rigaku NANO-Solver software to model the form factor of spherical CdSe nanocrystals in a matrix of toluene. The background scattering from a pure toluene capillary was subtracted from the experimental data. The software also accounted for instrumental smearing. Example TEM images and SAXS patterns are shown in Figure A-3.

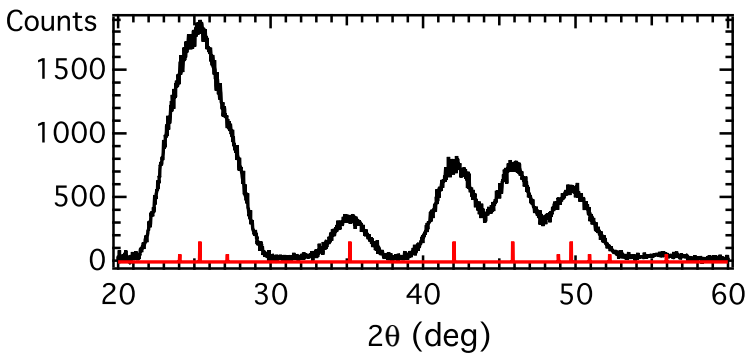

Figure A-1: XRD spectrum Cu Kα radiation of nanocrystals synthesized through CdO/TOP-Se hot injection method. Black line is QD spectrum, red vertical lines are bulk CdSe wurtzite expected peak positions.

A.2 Seeded Growth of QDs with Oleic Acid Ligands

CdSe QD cores with oleic acid ligands were synthesized using a seeded growth method adapted from Chen, *et al* [99]. Briefly, 10 mL of a 1:1 mixture of oleylamine:octadecene were degassed for 1 hour at 100 , then the temperature was lowered to 60 and 100 nmol of small (∼3 nm diameter) CdSe cores that had been synthesized via the standard method were injected. The reaction flask was again evacuated to remove hexanes from the solution. Under nitrogen, the temperature was increased to 240 , and a solution of 0.05M TPB-Se and 0.05M Cd-oleate were injected with a syringe pump at a rate of 2.1 mL/hr. Aliquots were removed at different times to achieve different nanocrystal sizes. The resulting seeded growth nanocrystals were precipitated with acetone and then with a mixture of 2:1 butanol:methanol.

A.3 Zincblende CdSe with Oleic Acid Ligands

Zincblende QDs were synthesized using SeO_2 and Cd(myristate) as precursors according to the method by Chen, *et al.* [100]. Briefly, 0.1 mmol of both Cd(myristate) and SeO_2 were added to a 50 mL 3-neck round bottom flask with 6.3 mL octadecene. This solution was degassed at room temperature and a vacuum of 200 mTorr for one hour. After degassing and under nitrogen, the reaction was heated to 240° C at a

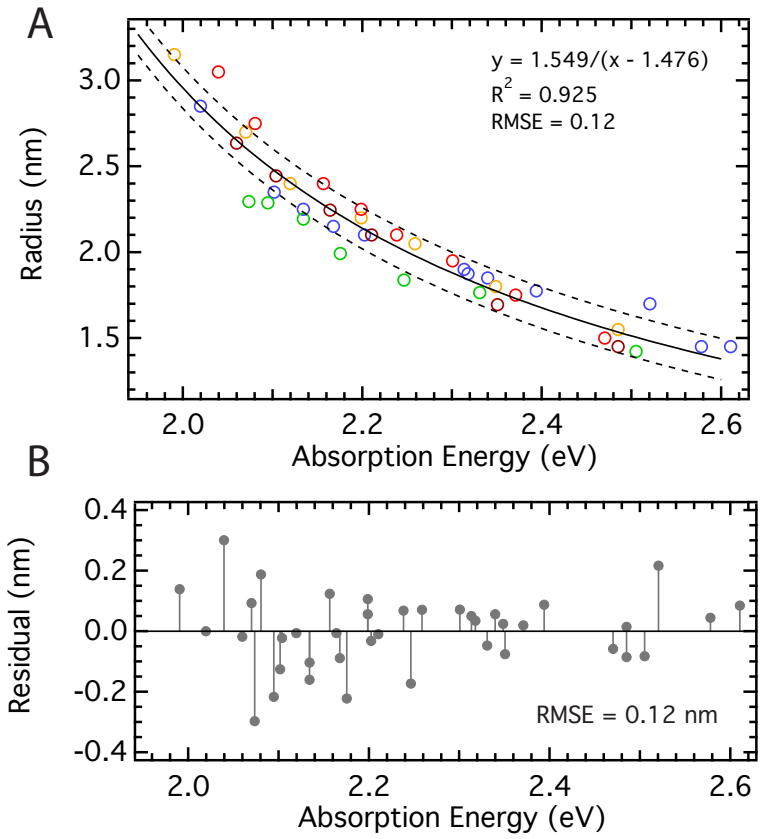

Figure A-2: (A) Plot of QD radii measured by TEM against the first absorption peak energy with a fit line corresponding to the equation R = 1.549/(AbsPeak - 1.476) as a solid black line. Dotted lines represent the best fit ± RMS error. Different colors represent different syntheses where aliquots were taken over time during the QD synthesis. (B) Residuals of the fit, with root-mean-square error 0.12 nm. This sizing curve and error were used throughout the manuscript for QD sizes.

rate of about 20° C per minute. The solution started to turn yellow at about 230∘ C. After the reaction vessel reached 240° C, 0.1 mL of oleic acid was added dropwise to serve as the surface ligand. Aliquots were taken during synthesis to achieve different nanocrystal sizes. QDs stopped growing when their first absorption feature reached about 560 nm, so a batch of zincblende QDs with first absorption feature near 520 nm was used with the seeded growth method above to achieve large sizes of zincblende QDs. The crystal phase of these QDs were verified using XRD (Figure A-4).

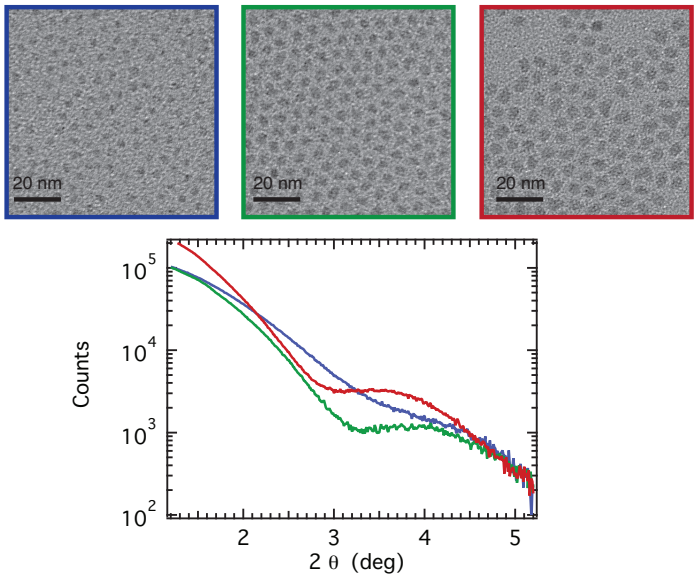

Figure A-3: Top: TEM images of three different sizes of QDs, ranging from small (3.1 nm) to large (4.5 nm). Bottom: SAXS patterns for the three different sizes of QDs with the same line colors as box colors for TEM images.

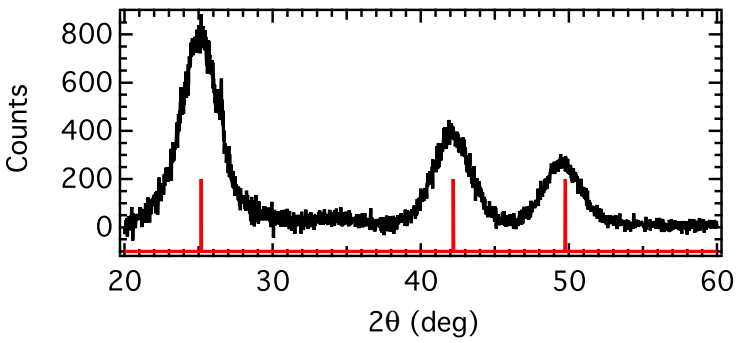

Figure A-4: XRD spectrum using Cu Kα radiation of nanocrystals synthesized using SeO_2 as the selenium precursor for zincblende QDs. Black line is QD spectrum, red vertical lines are expected peak positions for zincblende CdSe.

Appendix B

Additional Experiments: Nanoplatelets

In addition to the extensive work presented in Chapters 4 and 5 studying the low-frequency acoustic phonons of QDs, the Raman spectroscopy setup developed for this thesis has been used to understand several other materials systems. The most interesting or exciting results of those experiments are included in this Appendix.

B.1 CdSe Nanoplatelets

Advances in colloidal synthesis have yielded an array of different available shapes of semiconducting nanoparticles. An interesting emerging class of materials is the CdSe nanoplatelet. These materials are made analogously to CdSe nanoparticles, but with different precursors, coordinating solvent environments, and at different temperatures. They can form extensive stacks [132], and energy transfer between nanoplatelets can occur within picoseconds [133], much faster than the energy transfer rates between nanoparticles measured in Chapter 3. These nanoplatelets can be synthesized with monolayer precision in their thickness, and with varying aspect ratios and extents. There is negligible "confinement" of acoustic phonon modes in their in-plane directions, but significant confinement in their out-of-plane thickness direction. We sought to measure acoustic phonons propagating in a layer of finite thickness, which are known as Lamb waves and are schematically illustrated in Figure B-1. These Lamb waves have frequencies given by the following characteristic equations, where the boundary condition is zero stress (free boundary) at the top and bottom

of the plate [134]:

$$\frac{\tan\beta d/2}{\tan\alpha d/2} = -\frac{4\alpha\beta k^2}{(k^2-\beta^2)^2} \tag{B.1}$$

$$\frac{\tan\beta d/2}{\tan\alpha d/2} = -\frac{(k^2-\beta^2)^2}{4\alpha\beta k^2} \tag{B.2}$$

for $\alpha = (\omega^2/v_l^2) - k^2$ and $\beta = (\omega^2/v_t^2) - k^2$. The sound velocities v_l and v_t are the longitudinal and transverse sound velocities of the material that were also used to understand acoustic vibrations of spheres, d is the thickness of the plate, k is the wavevector, and ω is the frequency. The first of these equations refers to waves that are symmetrical about the midplane of the plate (Figure B-1b), and the second refers to those that are antisymmetric about the midplane (Figure B-1a).

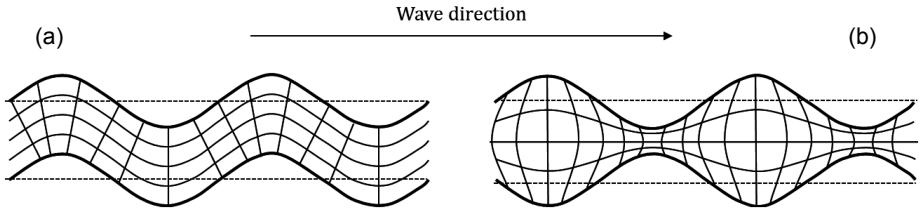

Figure B-1: Schematic of Lamb waves within an elastic plate. a) antisymmetric wave, and b) symmetric wave. Image reproduced from [135].

CdSe nanoplatelets of two different thicknesses, 5 monolayers and 6 monolayers (MLs), were measured using the Raman microscope described in Chapter 2-7. Their absorption spectra and resulting Raman spectra are shown in Figure B-2. The Raman spectra reveal a phonon feature with energy 29.3 cm^{-1} for the 5 ML nanoplatelets, and 25.7 cm^{-1} for the 6 ML platelets. 4 ML platelets were successfully synthesized by the author, but the corresponding Raman spectra did not reveal clear phonon features to test the thickness-dependent phonon frequency (Figure B-3). Future work on this project will involve improving the synthesis for more thicknesses of nanoplatelets, and the extension of mathematical models to understand acoustic modes in nanoscale elastic plates.

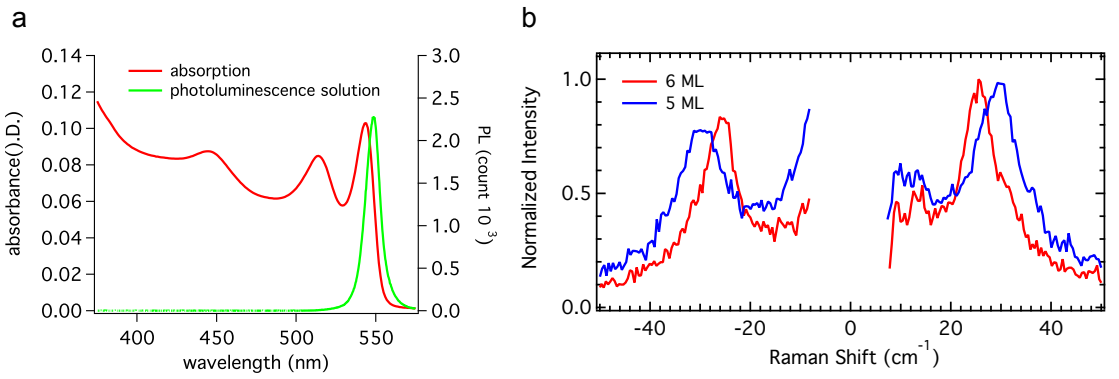

Figure B-2: a) Absorption and photoluminescence spectra of 5 monolayer CdSe nanoplatelets. b) Raman spectra of 5 ML and 6 ML nanoplatelets. Nanoplatelets and absorption spectra provided by Dr. Yunan Gao.

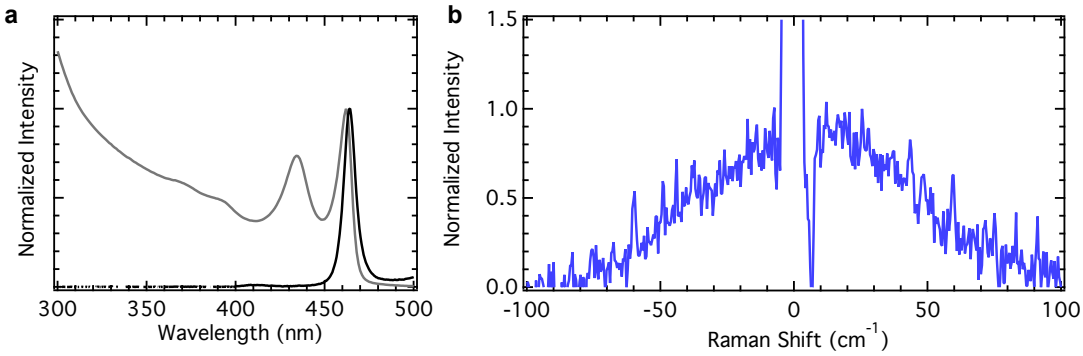

Figure B-3: a) Absorption and emission spectra of 4ML nanoplatelets synthesized through the method reported by [136], with thickness of 4 ML CdSe. b) Raman spectra for the nanoplatelets in (a).

B.2 Low Temperature Raman Measurements for Bulk Perovskite Materials

Lead halide perovskites have emerged in the last 5 years as one of the most rapidly growing new materials systems under study, largely driven by their incredible performance as solar cell active layer materials, achieving certified efficiencies of more than 20%, up from an initial efficiency of around 4% in 2009 [137]. The composition of these materials generally follows the formula ABX_3, where A is a cation, often Cs^+ or methyl ammonium (CH_3NH_3), B is a heavy metal, usually Pb, and X is a

halide such as Cl, Br, or I. The perovskite structure is shown in Figure B-4, with some example atoms/molecules that can occupy each of the lattice sites. Perovskites are exceptionally simple to make, usually involving simply mixing the precursors according to their stoichiometry. They can be made in bulk through spin coating or drop casting the precursor mixtures, and can be made as nanoplatelets or other nanostructures by adding a known quantity of ligand to the formation solution [138].

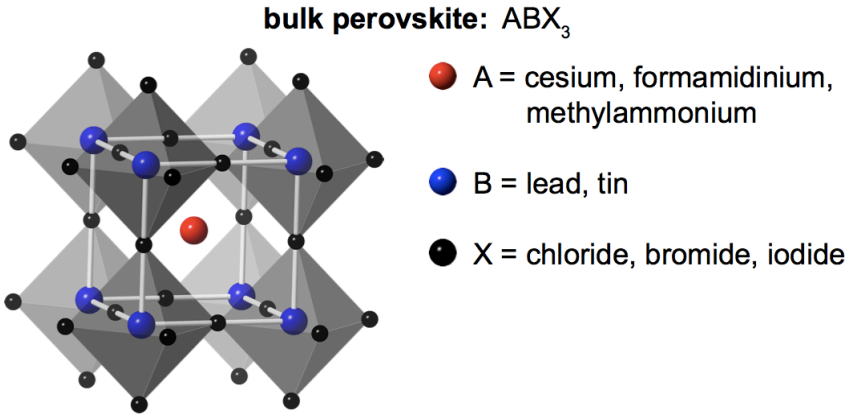

Figure B-4: Schematic structure of perovskite materials, with example atoms/molecules that can occupy each of the different lattice sites.

In Figure B-5, the Raman spectrum for bulk $CH_3NH_3PbBr_3$ perovskite materials displays significant peak sharpening at low temperatures (77 K) compared to room temperature, and, notably, the low-frequency region shows no phonon features up to about 30 cm^{-1}. These data suggested that Raman spectra of perovskite nanoplatelets may reveal size-dependent phonon features, much like the CdSe nanoplatelets.

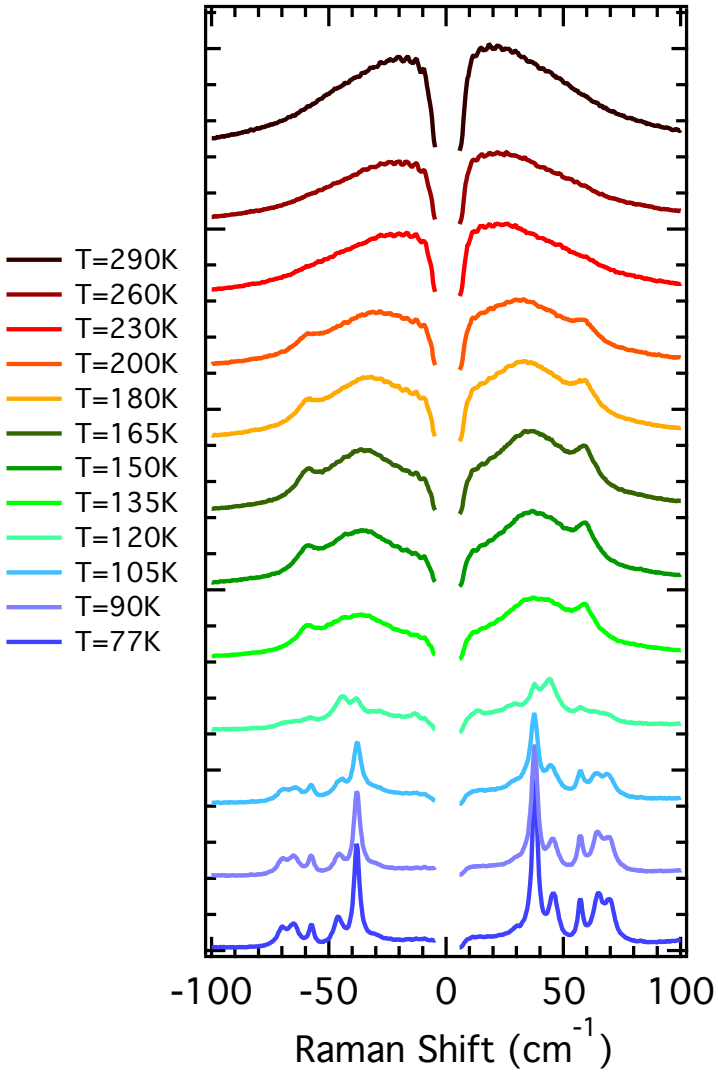

Figure B-5: Normalized temperature dependent Raman spectra of bulk $CH_3NH_3PbBr_3$ perovskite material. Spectra at each temperature are offset for clarity.

In order to study perovskite nanoplatelets, nearly monodisperse perovskite nanoplatelets with a thickness of one unit cell were synthesized by a hot injection method in a non-polar solvent octadecene solvent according to the method of Vybornyi, *et al.* [139]. These perovskite materials had a very sharp absorption feature (Figure B-6a), suggesting excellent monodispersity in thickness. However, the temperature-dependent Raman spectra never revealed any sharp peaks corresponding to nanoplatelet thickness (Figure B-6b), and the measurement was limited by very low Raman scattering intensity. Raman measurements on nanoplatelet materials prepared through other means yielded similar disappointing Raman spectra as well as significant fluorescence from these materials. While Raman spectra can be used to understand phase transitions and bulk properties of these materials, as well as potentially the effects of changes in material composition, perovskite nanoplatelets either suffer from stability issues or simply low Raman cross section that makes them particularly difficult to work with. Future work must focus on improving the synthesis and stability of these nanoplatelet materials before Raman spectroscopy will provide meaningful insight into their structure.

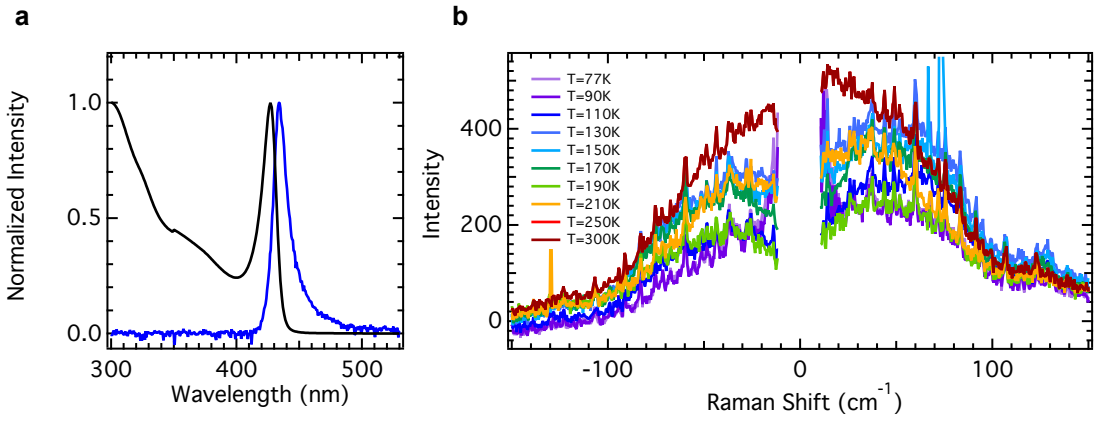

Figure B-6: Absorption (a) and Raman spectra (b) for perovskite nanoplatelets synthesized through a hot injection method in a non-polar solvent.

Bibliography

[1] Talapin, Dmitri V., Lee, Jong-Soo, Kovalenko, Maksym V., and Shevchenko, Elena V. Prospects of Colloidal Nanocrystals for Electronic and Optoelectronic Applications. *Chemical Reviews*, 110(1):389–458 (2010).

[2] Shirasaki, Yasuhiro, Supran, Geoffrey J., Bawendi, Moungi G., and Bulovic, Vladimir. Emergence of colloidal quantum-dot light-emitting technologies. *Nat Photon*, 7(1):13–23 (2013).

[3] Anikeeva, Polina O., Halpert, Jonathan E., Bawendi, Moungi G., and Bulović, Vladimir. Electroluminescence from a Mixed Red-Green-Blue Colloidal Quantum Dot Monolayer. *Nano Letters*, 7(8):2196–2200 (2007). PMID: 17616230.

[4] Ruland, Andrés, Schulz-Drost, Christian, Sgobba, Vito, and Guldi, Dirk M. Enhancing Photocurrent Efficiencies by Resonance Energy Transfer in CdTe Quantum Dot Multilayers: Towards Rainbow Solar Cells. *Advanced Materials*, 23(39):4573–4577 (2011).

[5] Nurmikko, Arto. What future for quantum dot-based light emitters? *Nat Nano*, 10(12):1001–1004 (2015).

[6] Urban, Jeffrey J. Prospects for thermoelectricity in quantum dot hybrid arrays. *Nat Nano*, 10(12):997–1001 (2015).

[7] Liu, Wenhao, Greytak, Andrew B, Lee, Jungmin, Wong, Cliff R, Park, Jongnam, Marshall, Lisa F, Jiang, Wen, Curtin, Peter N, Ting, Alice Y, Nocera, Daniel G, Fukumura, Dai, Jain, Rakesh K, and Bawendi, Moungi G. Compact biocompatible quantum dots via RAFT-mediated synthesis of imidazole-based random copolymer ligand. *Journal of the American Chemical Society*, 132(2):472–483 (2010).

[8] Tang, Jiang, Kemp, Kyle W., Hoogland, Sjoerd, Jeong, Kwang S., Liu, Huan, Levina, Larissa, Furukawa, Melissa, Wang, Xihua, Debnath, Ratan, Cha, Dongkyu, Chou, Kang Wei, Fischer, Armin, Amassian, Aram, Asbury, John B., and Sargent, Edward H. Colloidal-quantum-dot photovoltaics using atomic-ligand passivation. *Nature Materials*, 10(10):765–771 (2011).

[9] Chuang, Chia-Hao M., Brown, Patrick R., Bulović, Vladimir, and Bawendi, Moungi G. Improved performance and stability in quantum dot solar cells through band alignment engineering. *Nature Materials*, 13(8):796–801 (2014).

[10] Dabbousi, B. O., Rodriguez-Viejo, J., Mikulec, F. V., Heine, J. R., Mattoussi, H., Ober, R., Jensen, K. F., and Bawendi, M. G. (CdSe)ZnS Core-Shell Quantum Dots: Synthesis and Characterization of a Size Series of Highly Luminescent Nanocrystallites. *The Journal of Physical Chemistry B*, 101(46):9463–9475 (1997).

[11] Chen, Ou, Zhao, Jing, Chauhan, Vikash P., Cui, Jian, Wong, Cliff, Harris, Daniel K., Wei, He, Han, Hee-Sun, Fukumura, Dai, Jain, Rakesh K., and Bawendi, Moungi G. Compact high-quality CdSe-CdS core-shell nanocrystals with narrow emission linewidths and suppressed blinking. *Nat Mater*, 12(5):445–451 (2013).

[12] Kim, Sungjee, Fisher, Brent, Eisler, Hans-Jürgen, and Bawendi, Moungi. Type-II Quantum Dots: CdTe/CdSe(Core/Shell) and CdSe/ZnTe(Core/Shell) Heterostructures. *Journal of the American Chemical Society*, 125(38):11466–11467 (2003).

[13] Norris, D.J. *Measurement and assignment of the size-dependent optical spectrum in cadmium selenide (CdSe) quantum dots.* Ph.D. thesis, Massachusetts Institute of Technology (1995).

[14] Guyot-Sionnest, Philippe, Shim, Moonsub, Matranga, Chris, and Hines, Margaret. Intraband relaxation in CdSe quantum dots. *Phys. Rev. B*, 60:R2181–R2184 (1999).

[15] Schaller, Richard D., Pietryga, Jeffrey M., Goupalov, Serguei V., Petruska, Melissa A., Ivanov, Sergei A., and Klimov, Victor I. Breaking the Phonon Bottleneck in Semiconductor Nanocrystals via Multiphonon Emission Induced by Intrinsic Nonadiabatic Interactions. *Phys. Rev. Lett.*, 95:196401 (2005).

[16] Leatherdale, C. A., Woo, W. K., Mikulec, F. V., and Bawendi, M. G. On the Absorption Cross Section of CdSe Nanocrystal Quantum Dots. *The Journal of Physical Chemistry B*, 106(31):7619–7622 (2002).

[17] Ekimov, A. I., Kudryavtsev, I. A., Efros, Al. L., Yazeva, T. V., Hache, F., Schanne-Klein, M. C., Rodina, A. V., Ricard, D., and Flytzanis, C. Absorption and intensity-dependent photoluminescence measurements on CdSe quantum dots: assignment of the first electronic transitions. *J. Opt. Soc. Am. B*, 10(1):100–107 (1993).

[18] Parsons, R. B., Wardzynski, W., and Yoffe, A. D. The Optical Properties of Single Crystals of Cadmium Selenide. *Proceedings of the Royal Society of London A: Mathematical, Physical and Engineering Sciences*, 262(1308):120–131 (1961).

[19] Ashcroft, N. W. and Mermin, N. D. *Solid State Physics*. Harcourt College Publishers (1976).

[20] Alivisatos, A. P. Semiconductor Clusters, Nanocrystals, and Quantum Dots. *Science*, 271(5251):933–937 (1996).

[21] Cui, Jian, Beyler, Andrew P., Coropceanu, Igor, Cleary, Liam, Avila, Thomas R., Chen, Yue, Cordero, JoséM., Heathcote, S. Leigh, Harris, Daniel K., Chen, Ou, Cao, Jianshu, and Bawendi, Moungi G. Evolution of the Single-Nanocrystal Photoluminescence Linewidth with Size and Shell: Implications for Exciton–Phonon Coupling and the Optimization of Spectral Linewidths. *Nano Letters*, 16(1):289–296 (2016).

[22] Cui, Jian, Beyler, Andrew P., Marshall, Lisa F., Chen, Ou, Harris, Daniel K., Wanger, Darcy D., Brokmann, Xavier, and Bawendi, Moungi G. Direct probe of spectral inhomogeneity reveals synthetic tunability of single-nanocrystal spectral linewidths. *Nature Chemistry*, 5(7):602–606 (2013).

[23] Dal Corso, Andrea, Baroni, Stefano, Resta, Raffaele, and de Gironcoli, Stefano. *Ab initio* calculation of phonon dispersions in II-VI semiconductors. *Phys. Rev. B*, 47:3588–3592 (1993).

[24] Grimvall, Goran. *Thermophysical Properties of Materials*. Elselvier (1999).

[25] Regner, Keith T., Sellan, Daniel P., Su, Zonghui, Amon, Cristina H., McGaughey, Alan J. H., and Malen, Jonathan A. Broadband phonon mean free path contributions to thermal conductivity measured using frequency domain thermoreflectance. *Nature Communications*, 4:1640 (2013).

[26] Swartz, E. T. and Pohl, R. O. Thermal boundary resistance. *Rev. Mod. Phys.*, 61:605–668 (1989).

[27] Cahill, David G., Ford, Wayne K., Goodson, Kenneth E., Mahan, Gerald D., Majumdar, Arun, Maris, Humphrey J., Merlin, Roberto, and Phillpot, Simon R. Nanoscale thermal transport. *Journal of Applied Physics*, 93(2):793–818 (2003).

[28] Yang, Ronggui, Chen, Gang, and Dresselhaus, Mildred S. Thermal conductivity of simple and tubular nanowire composites in the longitudinal direction. *Phys. Rev. B*, 72:125418 (2005).

[29] Ong, Wee-Liat, Rupich, Sara M., Talapin, Dmitri V., McGaughey, Alan J. H., and Malen, Jonathan A. Surface chemistry mediates thermal transport in three-dimensional nanocrystal arrays. *Nature Materials*, 12(5):410–415 (2013).

[30] Ong, Wee-Liat, Majumdar, Shubhaditya, Malen, Jonathan A., and McGaughey, Alan J. H. Coupling of Organic and Inorganic Vibrational States and Their Thermal Transport in Nanocrystal Arrays. *The Journal of Physical Chemistry C*, 118(14):7288–7295 (2014).

[31] Losego, Mark D. and Cahill, David G. Thermal transport: Breaking through barriers. *Nat Mater*, 12(5):382–384 (2013).

[32] Schaller, Richard D., Pietryga, Jeffrey M., Goupalov, Serguei V., Petruska, Melissa A., Ivanov, Sergei A., and Klimov, Victor I. Breaking the Phonon Bottleneck in Semiconductor Nanocrystals via Multiphonon Emission Induced by Intrinsic Nonadiabatic Interactions. *Phys. Rev. Lett.*, 95:196401 (2005).

[33] Kambhampati, Patanjali. Hot Exciton Relaxation Dynamics in Semiconductor Quantum Dots: Radiationless Transitions on the Nanoscale. *The Journal of Physical Chemistry C*, 115(45):22089–22109 (2011).

[34] Gao, Yunan, Sandeep, C. S. Suchand, Schins, Juleon M., Houtepen, Arjan J., and Siebbeles, Laurens D. A. Disorder strongly enhances Auger recombination in conductive quantum-dot solids. *Nat Commun*, 4 (2013).

[35] Nirmal, M., Dabbousi, B. O., Bawendi, M. G., Macklin, J. J., Trautman, J. K., Harris, T. D., and Brus, L. E. Fluorescence intermittency in single cadmium selenide nanocrystals. *Nature*, 383(6603):802–804 (1996).

[36] Lakowicz, Joseph. *Principles of Fluorescence Spectroscopy*. Springer (2006).

[37] Gouadec, Gwénaël and Colomban, Philippe. Raman Spectroscopy of nanomaterials: How spectra relate to disorder, particle size and mechanical properties. *Progress in Crystal Growth and Characterization of Materials*, 53(1):1–56 (2007).

[38] Yu, Peter and Cardona, Manuel. *Fundamentals of Semiconductors*. Springer (2010).

[39] Carter, R., Crawford, B., Edgell, W., and Swanson, D. *Infrared and Raman Spectroscopy, Pt A.*, pp. 36–44. Marcel Dekker, Inc., 1 edition (1976).

[40] Sherwood, P. M. A. *Vibrational Spectroscopy of Solids*. Cambridge University Press (1972).

[41] Weber, Willes and Merlin, Roberto, editors. *Raman Scattering in Materials Science*. Springer (2000).

[42] Mork, A. Jolene, Weidman, Mark C., Prins, Ferry, and Tisdale, William A. Magnitude of the Förster Radius in Colloidal Quantum Dot Solids. *The Journal of Physical Chemistry C*, 118(25):13920–13928 (2014).

[43] Dexter, D. L. A Theory of Sensitized Luminescence in Solids. *The Journal of Chemical Physics*, 21(5):836–850 (1953).

[44] Medintz, Igor and Hilderbrandt, Niko. *FRET - Förster Resonance Energy Transfer: From Theory to Applications*. WILEY-VCH Verlag (2014).

[45] Tokmakoff, Andrei. Förster Energy Transfer. http://ocw.mit.edu/courses/chemistry/5-74-introductory-quantum-mechanics-ii-spring-2004/lecture-notes/14.pdf (2004).

[46] Medintz, Igor L., Clapp, Aaron R., Mattoussi, Hedi, Goldman, Ellen R., Fisher, Brent, and Mauro, J. Matthew. Self-assembled nanoscale biosensors based on quantum dot FRET donors. *Nat Mater*, 2(9):630–638 (2003).

[47] Medintz, Igor L., Clapp, Aaron R., Brunel, Florence M., Tiefenbrunn, Theresa, Tetsuo Uyeda, H., Chang, Eddie L., Deschamps, Jeffrey R., Dawson, Philip E., and Mattoussi, Hedi. Proteolytic activity monitored by fluorescence resonance energy transfer through quantum-dot-peptide conjugates. *Nat Mater*, 5(7):581–589 (2006).

[48] Curutchet, Carles, Franceschetti, Alberto, Zunger, Alex, and Scholes, Gregory D. Examining Förster Energy Transfer for Semiconductor Nanocrystalline Quantum Dot Donors and Acceptors. *The Journal of Physical Chemistry C*, 112(35):13336–13341 (2008).

[49] Wolcott, Abraham, Doyeux, Vincent, Nelson, Cory A., Gearba, Raluca, Lei, Kin Wai, Yager, Kevin G., Dolocan, Andrei D., Williams, Kenrick, Nguyen, Daniel, and Zhu, X. Y. Anomalously Large Polarization Effect Responsible for Excitonic Red Shifts in PbSe Quantum Dot Solids. *The Journal of Physical Chemistry Letters*, 2(7):795–800 (2011).

[50] Geiregat, Pieter, Justo, Yolanda, Abe, Sofie, Flamee, Stijn, and Hens, Zeger. Giant and Broad-Band Absorption Enhancement in Colloidal Quantum Dot Monolayers through Dipolar Coupling. *ACS Nano*, 7(2):987–993 (2013).

[51] Allan, G. and Delerue, C. Energy transfer between semiconductor nanocrystals: Validity of Förster's theory. *Phys. Rev. B*, 75:195311 (2007).

[52] Baer, Roi and Rabani, Eran. Theory of resonance energy transfer involving nanocrystals: The role of high multipoles. *The Journal of Chemical Physics*, 128(18):184710 (2008).

[53] Lee, Elizabeth M. Y., Tisdale, William A., and Willard, Adam P. Can Disorder Enhance Incoherent Exciton Diffusion? *The Journal of Physical Chemistry B*, 119(30):9501–9509 (2015).

[54] Kagan, C. R., Murray, C. B., Nirmal, M., and Bawendi, M. G. Electronic Energy Transfer in CdSe Quantum Dot Solids. *Phys. Rev. Lett.*, 76:1517–1520 (1996).

[55] Crooker, S. A., Hollingsworth, J. A., Tretiak, S., and Klimov, V. I. Spectrally Resolved Dynamics of Energy Transfer in Quantum-Dot Assemblies: Towards Engineered Energy Flows in Artificial Materials. *Phys. Rev. Lett.*, 89:186802 (2002).

[56] Lunz, Manuela, Bradley, A. Louise, Chen, Wei-Yu, and GunÊijko, Yurii K. Two-Dimensional Förster Resonant Energy Transfer in a Mixed Quantum Dot Monolayer: Experiment and Theory. *The Journal of Physical Chemistry C*, 113(8):3084–3088 (2009).

[57] Achermann, Marc, Petruska, Melissa A., Crooker, Scott A., and Klimov, Victor I. Picosecond Energy Transfer in Quantum Dot LangmuirâĹŠBlodgett Nanoassemblies. *The Journal of Physical Chemistry B*, 107(50):13782–13787 (2003).

[58] Kim, DaeGwi, Okahara, Shinya, Nakayama, Masaaki, and Shim, YongGu. Experimental verification of Förster energy transfer between semiconductor quantum dots. *Phys. Rev. B*, 78:153301 (2008).

[59] Lingley, Zachary, Lu, Siyuan, and Madhukar, Anupam. A High Quantum Efficiency Preserving Approach to Ligand Exchange on Lead Sulfide Quantum Dots and Interdot Resonant Energy Transfer. *Nano Letters*, 11(7):2887–2891 (2011).

[60] Lunz, Manuela, Bradley, A. Louise, Chen, Wei-Yu, Gerard, Valerie A., Byrne, Stephen J., Gun'ko, Yurii K., Lesnyak, Vladimir, and Gaponik, Nikolai. Influence of quantum dot concentration on Förster resonant energy transfer in monodispersed nanocrystal quantum dot monolayers. *Phys. Rev. B*, 81:205316 (2010).

[61] Dang, Cuong, Lee, Joonhee, Breen, Craig, Steckel, Jonathan S., Coe-Sullivan, Seth, and Nurmikko, Arto. Red, green and blue lasing enabled by single-exciton gain in colloidal quantum dot films. *Nature Nanotechnology*, 7(5):335–339 (2012).

[62] Yu, W. William, Qu, Lianhua, Guo, Wenzhuo, and Peng, Xiaogang. Experimental Determination of the Extinction Coefficient of CdTe, CdSe, and CdS Nanocrystals. *Chemistry of Materials*, 15(14):2854–2860 (2003).

[63] Segets, Doris, Lucas, J. Matthew, Klupp Taylor, Robin N., Scheele, Marcus, Zheng, Haimei, Alivisatos, A. Paul, and Peukert, Wolfgang. Determination of the Quantum Dot Band Gap Dependence on Particle Size from Optical Absorbance and Transmission Electron Microscopy Measurements. *ACS Nano*, 6(10):9021–9032 (2012).

[64] Yoneda, Y. Anomalous Surface Reflection of X Rays. *Phys. Rev.*, 131:2010–2013 (1963).

[65] De Geyter, Bram and Hens, Zeger. The absorption coefficient of PbSe/CdSe core/shell colloidal quantum dots. *Applied Physics Letters*, 97(16):161908 (2010).

[66] Danisch, Maximilien, Jin, Yuliang, and Makse, Hernan A. Model of random packings of different size balls. *Phys. Rev. E*, 81:051303 (2010).

[67] Miyazaki, Jun and Kinoshita, Shuichi. Site-selective spectroscopic study on the dynamics of exciton hopping in an array of inhomogeneously broadened quantum dots. *Phys. Rev. B*, 86:035303 (2012).

[68] Chung, Inhee, Shimizu, Ken T, and Bawendi, Moungi G. Room temperature measurements of the 3D orientation of single CdSe quantum dots using polarization microscopy. *Proceedings of the National Academy of Sciences of the United States of America*, 100(2):405–408 (2003).

[69] Murray, C. B., Kagan, C. R., and Bawendi, M. G. Self-Organization of CdSe Nanocrystallites into Three-Dimensional Quantum Dot Superlattices. *Science*, 270(5240):1335–1338 (1995).

[70] Schrier, Joshua and Wang, Lin-Wang. Shape Dependence of Resonant Energy Transfer between Semiconductor Nanocrystals. *The Journal of Physical Chemistry C*, 112(30):11158–11161 (2008).

[71] Halivni, Shira, Sitt, Amit, Hadar, Ido, and Banin, Uri. Effect of Nanoparticle Dimensionality on Fluorescence Resonance Energy Transfer in Nanoparticle–Dye Conjugated Systems. *ACS Nano*, 6(3):2758–2765 (2012).

[72] Jasieniak, Jacek, Smith, Lisa, Embden, Joel van, Mulvaney, Paul, and Califano, Marco. Re-examination of the Size-Dependent Absorption Properties of CdSe Quantum Dots. *The Journal of Physical Chemistry C*, 113(45):19468–19474 (2009).

[73] Kovalenko, Maksym V. Opportunities and challenges for quantum dot photovoltaics. *Nat Nano*, 10(12):994–997 (2015).

[74] Choi, Ji-Hyuk, Fafarman, Aaron T., Oh, Soong Ju, Ko, Dong-Kyun, Kim, David K., Diroll, Benjamin T., Muramoto, Shin, Gillen, J. Greg, Murray, Christopher B., and Kagan, Cherie R. Bandlike Transport in Strongly Coupled and Doped Quantum Dot Solids: A Route to High-Performance Thin-Film Electronics. *Nano Letters*, 12(5):2631–2638 (2012).

[75] Kagan, Cherie R. and Murray, Christopher B. Charge transport in strongly coupled quantum dot solids. *Nature Nanotechnology*, 10(12):1013–1026 (2015).

[76] Wang, Congjun, Shim, Moonsub, and Guyot-Sionnest, Philippe. Electrochromic Nanocrystal Quantum Dots. *Science*, 291(5512):2390–2392 (2001).

[77] Zhao, Yiming, Riemersma, Charl, Pietra, Francesca, Koole, Rolf, de Mello Donegá, Celso, and Meijerink, Andries. High-Temperature Luminescence Quenching of Colloidal Quantum Dots. *ACS Nano*, 6(10):9058–9067 (2012).

[78] Besombes, L., Kheng, K., Marsal, L., and Mariette, H. Acoustic phonon broadening mechanism in single quantum dot emission. *Phys. Rev. B*, 63:155307 (2001).

[79] Favero, I., Cassabois, G., Ferreira, R., Darson, D., Voisin, C., Tignon, J., Delalande, C., Bastard, G., Roussignol, Ph., and Gérard, J. M. Acoustic phonon sidebands in the emission line of single InAs/GaAs quantum dots. *Phys. Rev. B*, 68:233301 (2003).

[80] Alivisatos, A. P. Perspectives on the Physical Chemistry of Semiconductor Nanocrystals. *The Journal of Physical Chemistry*, 100(31):13226–13239 (1996).

[81] Liu, Jin, Kilina, Svetlana V., Tretiak, Sergei, and Prezhdo, Oleg V. Ligands Slow Down Pure-Dephasing in Semiconductor Quantum Dots. *ACS Nano*, 9(9):9106–9116 (2015).

[82] Oron, Dan, Aharoni, Assaf, de Mello Donega, Celso, van Rijssel, Jos, Meijerink, Andries, and Banin, Uri. Universal Role of Discrete Acoustic Phonons in the Low-Temperature Optical Emission of Colloidal Quantum Dots. *Phys. Rev. Lett.*, 102:177402 (2009).

[83] Rainò, Gabriele, Moreels, Iwan, Hassinen, Antti, Stöferle, Thilo, Hens, Zeger, and Mahrt, Rainer F. Exciton Dynamics within the Band-Edge Manifold States: The Onset of an Acoustic Phonon Bottleneck. *Nano Letters*, 12(10):5224–5229 (2012).

[84] Lamb, Horace. On the Vibrations of an Elastic Sphere. *Proceedings of the London Mathematical Society*, s1-13(1):189–212 (1881).

[85] Cerullo, G., De Silvestri, S., and Banin, U. Size-dependent dynamics of coherent acoustic phonons in nanocrystal quantum dots. *Phys. Rev. B*, 60:1928–1932 (1999).

[86] Fujii, Minoru, Kanzawa, Yoshihiko, Hayashi, Shinji, and Yamamoto, Keiichi. Raman scattering from acoustic phonons confined in Si nanocrystals. *Phys. Rev. B*, 54:R8373–R8376 (1996).

[87] Zhao, Jialong and Masumoto, Yasuaki. Size dependence of confined acoustic phonons in CuCl nanocrystals. *Phys. Rev. B*, 60:4481–4484 (1999).

[88] Chassaing, P.-M., Demangeot, F., Combe, N., Saint-Macary, L., Kahn, M. L., and Chaudret, B. Raman scattering by acoustic phonons in wurtzite ZnO prismatic nanoparticles. *Phys. Rev. B*, 79:155314 (2009).

[89] Chilla, Gerwin, Kipp, Tobias, Menke, Torben, Heitmann, Detlef, Nikolic, Marija, Frömsdorf, Andreas, Kornowski, Andreas, Förster, Stephan, and Weller, Horst. Direct Observation of Confined Acoustic Phonons in the Photoluminescence Spectra of a Single CdSe-CdS-ZnS Core-Shell-Shell Nanocrystal. *Phys. Rev. Lett.*, 100:057403 (2008).

[90] Ikezawa, Michio, Okuno, Tsuyoshi, Masumoto, Yasuaki, and Lipovskii, Andrey A. Complementary detection of confined acoustic phonons in quantum dots by coherent phonon measurement and Raman scattering. *Phys. Rev. B*, 64:201315 (2001).

[91] Ivanda, M., Babocsi, K., Dem, C., Schmitt, M., Montagna, M., and Kiefer, W. Low-wave-number Raman scattering from CdS_xSe_{1-x} quantum dots embedded in a glass matrix. *Phys. Rev. B*, 67:235329 (2003).

[92] Saviot, L., Champagnon, B., Duval, E., Kudriavtsev, I. A., and Ekimov, A. I. Size dependence of acoustic and optical vibrational modes of CdSe nanocrystals in glasses. *Journal of Non-Crystalline Solids*, 197(2–3):238–246 (1996).

[93] Verma, Prabhat, Cordts, W., Irmer, G., and Monecke, J. Acoustic vibrations of semiconductor nanocrystals in doped glasses. *Phys. Rev. B*, 60:5778–5785 (1999).

[94] Son, Dong Hee, Wittenberg, Joshua S., Banin, Uri, and Alivisatos, A. Paul. Second Harmonic Generation and Confined Acoustic Phonons in Highly Excited Semiconductor Nanocrystals. *The Journal of Physical Chemistry B*, 110(40):19884–19890 (2006).

[95] Arora, Akhilesh K., Rajalakshmi, M., Ravindran, T. R., and Sivasubramanian, V. Raman spectroscopy of optical phonon confinement in nanostructured materials. *Journal of Raman Spectroscopy*, 38(6):604–617 (2007).

[96] Rajalakshmi, M., Arora, Akhilesh K., Bendre, B. S., and Mahamuni, Shailaja. Optical phonon confinement in zinc oxide nanoparticles. *Journal of Applied Physics*, 87(5):2445–2448 (2000).

[97] Duval, Eugène. Far-infrared and Raman vibrational transitions of a solid sphere: Selection rules. *Phys. Rev. B*, 46:5795–5797 (1992).

[98] Peng, Z. Adam and Peng, Xiaogang. Formation of High-Quality CdTe, CdSe, and CdS Nanocrystals Using CdO as Precursor. *Journal of the American Chemical Society*, 123(1):183–184 (2001).

[99] Chen, Ou, Yang, Yongan, Wang, Tie, Wu, Huimeng, Niu, Chenggang, Yang, Jianhui, and Cao, Y. Charles. Surface-Functionalization-Dependent Optical Properties of II–VI Semiconductor Nanocrystals. *Journal of the American Chemical Society*, 133(43):17504–17512 (2011).

[100] Chen, Ou, Chen, Xian, Yang, Yongan, Lynch, Jared, Wu, Huimeng, Zhuang, Jiaqi, and Cao, Y.âĂĚCharles. Synthesis of Metal–Selenide Nanocrystals Using Selenium Dioxide as the Selenium Precursor. *Angewandte Chemie International Edition*, 47(45):8638–8641 (2008).

[101] Owen, Jonathan S., Park, Jungwon, Trudeau, Paul-Emile, and Alivisatos, A. Paul. Reaction Chemistry and Ligand Exchange at CadmiumâĹŠSelenide Nanocrystal Surfaces. *Journal of the American Chemical Society*, 130(37):12279–12281 (2008).

[102] Montagna, Maurizio and Dusi, Roberto. Raman scattering from small spherical particles. *Phys. Rev. B*, 52:10080–10089 (1995).

[103] Sauceda, Huziel E., Mongin, Denis, Maioli, Paolo, Crut, Aurélien, Pellarin, Michel, Fatti, Natalia Del, Vallée, Fabrice, and Garzón, Ignacio L. Vibrational Properties of Metal Nanoparticles: Atomistic Simulation and Comparison with Time-Resolved Investigation. *The Journal of Physical Chemistry C*, 116(47):25147–25156 (2012).

[104] Goodfellow, Brian W., Yu, Yixuan, Bosoy, Christian A., Smilgies, Detlef-M., and Korgel, Brian A. The Role of Ligand Packing Frustration in Body-Centered Cubic (bcc) Superlattices of Colloidal Nanocrystals. *The Journal of Physical Chemistry Letters*, 6(13):2406–2412 (2015).

[105] Boles, Michael A. and Talapin, Dmitri V. Many-Body Effects in Nanocrystal Superlattices: Departure from Sphere Packing Explains Stability of Binary Phases. *Journal of the American Chemical Society*, 137(13):4494–4502 (2015).

[106] Lisiecki, Isabelle, Halté, Valérie, Petit, Christophe, Pileni, Marie-Paule, and Bigot, Jean-Yves. Vibration Dynamics of Supra-Crystals of Cobalt Nanocrystals Studied With Femtosecond Laser Pulses. *Advanced Materials*, 20(21):4176–4179 (2008).

[107] Poyser, Caroline L., Czerniuk, Thomas, Akimov, Andrey, Diroll, Benjamin T., Gaulding, E. Ashley, Salasyuk, Alexey S., Kent, Anthony J., Yakovlev, Dmitri R., Bayer, Manfred, and Murray, Christopher B. Coherent Acoustic Phonons in Colloidal Semiconductor Nanocrystal Superlattices. *ACS Nano*, 10(1):1163–1169 (2016).

[108] Selfridge, A. R. Approximate Material Properties in Isotropic Materials. *IEEE Transactions on Sonics and Ultrasonics*, 32(3):381–394 (1985).

[109] Weidman, Mark C., Yager, Kevin G., and Tisdale, William A. Interparticle Spacing and Structural Ordering in Superlattice PbS Nanocrystal Solids Undergoing Ligand Exchange. *Chemistry of Materials*, 27(2):474–482 (2015).

[110] DelRio, Frank W., Jaye, Cherno, Fischer, Daniel A., and Cook, Robert F. Elastic and adhesive properties of alkanethiol self-assembled monolayers on gold. *Applied Physics Letters*, 94(13):131909 (2009).

[111] Galland, Christophe, Ghosh, Yagnaseni, Steinbruck, Andrea, Sykora, Milan, Hollingsworth, Jennifer A., Klimov, Victor I., and Htoon, Han. Two types of luminescence blinking revealed by spectroelectrochemistry of single quantum dots. *Nature*, 479(7372):203–207 (2011).

[112] Coropceanu, Igor and Bawendi, Moungi G. Core/Shell Quantum Dot Based Luminescent Solar Concentrators with Reduced Reabsorption and Enhanced Efficiency. *Nano Letters*, 14(7):4097–4101 (2014).

[113] Portales, Hervé, Saviot, Lucien, Duval, Eugène, Gaudry, Mélanie, Cottancin, Emmanuel, Pellarin, Michel, Lermé, Jean, and Broyer, Michel. Resonant Raman scattering by quadrupolar vibrations of Ni-Ag core-shell nanoparticles. *Phys. Rev. B*, 65:165422 (2002).

[114] Chen, I-Chuen, Weng, Chih-Li, Lin, Cheng-Hsiao, and Tsai, Yan-Chr. Low-frequency Raman scattering from acoustic vibrations of spherical CdSe/CdS nanoparticles. *Journal of Applied Physics*, 108(8):083530 (2010).

[115] Bozyigit, Deniz, Yazdani, Nuri, Yarema, Maksym, Yarema, Olesya, Lin, Weyde Matteo Mario, Volk, Sebastian, Vuttivorakulchai, Kantawong, Luisier, Mathieu, Juranyi, Fanni, and Wood, Vanessa. Soft surfaces of nanomaterials enable strong phonon interactions. *Nature*, 531(7596):618–622 (2016).

[116] Saviot, Lucien, Netting, Caleb H., and Murray, Daniel B. Damping by Bulk and Shear Viscosity of Confined Acoustic Phonons for Nanostructures in Aqueous Solution. *The Journal of Physical Chemistry B*, 111(25):7457–7461 (2007).

[117] Morse, Philip M. Diatomic Molecules According to the Wave Mechanics. II. Vibrational Levels. *Phys. Rev.*, 34:57–64 (1929).

[118] Jones, J. E. On the Determination of Molecular Fields. II. From the Equation of State of a Gas. *Proceedings of the Royal Society of London A: Mathematical, Physical and Engineering Sciences*, 106(738):463–477 (1924).

[119] Peercy, P. S. and Morosin, B. Pressure and Temperature Dependences of the Raman-Active Phonons in SnO_2. *Phys. Rev. B*, 7:2779–2786 (1973).

[120] Ohsaka, Toshiaki. Temperature Dependence of the Raman Spectrum in Anatase TiO2. *Journal of the Physical Society of Japan*, 48(5):1661–1668 (1980).

[121] Spanier, Jonathan E., Robinson, Richard D., Zhang, Feng, Chan, Siu-Wai, and Herman, Irving P. Size-dependent properties of CeO_{2-y} nanoparticles as studied by Raman scattering. *Phys. Rev. B*, 64:245407 (2001).

[122] Li, W. S., Shen, Z. X., Feng, Z. C., and Chua, S. J. Temperature dependence of Raman scattering in hexagonal gallium nitride films. *Journal of Applied Physics*, 87(7):3332–3337 (2000).

[123] Mead, D. G. and Wilkinson, G. R. The temperature dependence of the Raman effect in some wurtzite type crystals. *Journal of Raman Spectroscopy*, 6(3):123–129 (1977).

[124] Iwanaga, H., Kunishige, A., and Takeuchi, S. Anisotropic thermal expansion in wurtzite-type crystals. *Journal of Materials Science*, 35(10):2451–2454 (2000).

[125] Montalvo, R. A. and Langer, D. W. Linear Compressibilities of IIâĂŘVI Compound Single Crystals. *Journal of Applied Physics*, 41(10):4101–4104 (1970).

[126] Alivisatos, A. P., Harris, T. D., Brus, L. E., and Jayaraman, A. Resonance Raman scattering and optical absorption studies of CdSe microclusters at high pressure. *The Journal of Chemical Physics*, 89(10):5979–5982 (1988).

[127] Bellowsa), James C. and Prasadb), Paras N. Dephasing times and linewidths of optical transitions in molecular crystals. Temperature dependence of line shapes, linewidths, and frequencies of Raman active phonons in naphthalene. *The Journal of Chemical Physics*, 70(4):1864–1871 (1979).

[128] Maradudin, A. A., Fein, A. E., and Vineyard, G. H. On the evaluation of phonon widths and shifts. *physica status solidi (b)*, 2(11):1479–1492 (1962).

[129] Murray, C. B., Norris, D. J., and Bawendi, M. G. Synthesis and characterization of nearly monodisperse CdE (E = sulfur, selenium, tellurium) semiconductor nanocrystallites. *Journal of the American Chemical Society*, 115(19):8706–8715 (1993).

[130] Abe, Sofie, Čapek, Richard Karel, De Geyter, Bram, and Hens, Zeger. Tuning the Postfocused Size of Colloidal Nanocrystals by the Reaction Rate: From Theory to Application. *ACS Nano*, 6(1):42–53 (2012).

[131] Weidman, Mark C., Beck, Megan E., Hoffman, Rachel S., Prins, Ferry, and Tisdale, William A. Monodisperse, Air-Stable PbS Nanocrystals via Precursor Stoichiometry Control. *ACS Nano*, 8(6):6363–6371 (2014).

[132] Jana, Santanu, Phan, Trang N. T., Bouet, Cécile, Tessier, Mickael D., Davidson, Patrick, Dubertret, Benoit, and Abécassis, Benjamin. Stacking and Colloidal Stability of CdSe Nanoplatelets. *Langmuir*, 31(38):10532–10539 (2015).

[133] Rowland, Clare E., Fedin, Igor, Zhang, Hui, Gray, Stephen K., Govorov, Alexander O., Talapin, Dmitri V., and Schaller, Richard D. Picosecond energy transfer and multiexciton transfer outpaces Auger recombination in binary CdSe nanoplatelet solids. *Nat Mater*, 14(5):484–489 (2015).

[134] Lamb, Horace. On Waves in an Elastic Plate. *Proceedings of the Royal Society of London A: Mathematical, Physical and Engineering Sciences* (1916).

[135] Marks, Ryan, Clarke, Alastair, Featherston, Carol, Paget, Christophe, and Pullin, Rhys. Lamb wave interaction with adhesively bonded stiffeners and disbonds using 3D vibrometry. *Applied Sciences*, 6(1):12 (2016).

[136] Chen, Dongdong, Gao, Yuan, Chen, Yiya, Ren, Yang, and Peng, Xiaogang. Structure Identification of Two-Dimensional Colloidal Semiconductor Nanocrystals with Atomic Flat Basal Planes. *Nano Letters*, 15(7):4477–4482 (2015).

[137] NREL. Efficiency Chart.

[138] Tyagi, Pooja, Arveson, Sarah M., and Tisdale, William A. Colloidal Organohalide Perovskite Nanoplatelets Exhibiting Quantum Confinement. *The Journal of Physical Chemistry Letters*, 6(10):1911–1916 (2015).

[139] Vybornyi, Oleh, Yakunin, Sergii, and Kovalenko, Maksym V. Polar-solvent-free colloidal synthesis of highly luminescent alkylammonium lead halide perovskite nanocrystals. *Nanoscale*, 8:6278–6283 (2016).